Doctoral Dissertation

Comprehensive study of ^{12}C by precise three-α cluster model wave functions

(精密3αクラスター模型波動関数による炭素12原子核の包括的研究)

Hajime Moriya

Theoretical Nuclear Physics Laboratory

Hokkaido University

森谷 元

北海道大学理学院宇宙理学専攻

原子核理論研究室

2023年3月

Contents

Abstract

The cluster structure is an essential ingredient to describe nuclear structure, in which nuclear systems are composed of some subunits of several nucleons. ^{4}He cluster, called α cluster is one of the most basic clusters which has extraordinarily large binding energy and the excited states are located in comparably high energy region. In particular, ^{12}C has been investigated as a three-α system for a long time because of its first $J^\pi = 0^+$ excited state, the Hoyle state, in which three α clusters are well developed. The Hoyle state plays a crucial role in the triple-α reaction process where an α particle sequentially captures two more α particles and finally ^{12}C is synthesized. There are mainly two remarkable points. One is that recently, the rotational excited states series of the Hoyle state, the Hoyle band, was proposed and the structure of the first $J^\pi = 2^+$ excited state has been paid attention. However, the structure of the 2^+_2 state, especially for its geometric three-α structure is still unclear. The other point is that the triple-α process usually occurs in astrophysical environments e.g., X-ray bursting of an accreting neutron star, where three α particles have background of neutron matter. Thus, it is necessary to consider the effect to the Hoyle state from the neutron matter.

To settle these points, we comprehensively investigate three-α cluster structure of ^{12}C, using precise three-α cluster wave function obtained by the stochastic variational method and the correlated Gaussian basis. In the three-α cluster model, α clusters are treated as structureless charged particles (macroscopic cluster model) and the orthogonality condition to the Pauli forbidden states between α particles is imposed which is called the orthogonality condition model (OCM). For the former, we introduced the confining potential to obtain the wave function in the square integrable form, allowing an analysis of the density distributions of three-α particles. It is concluded that the 2^+_2 state is not a simple rigid rotational excited state of the Hoyle state because the ^{8}Be+α component of 2^+_2 state is 2/3 of that of the Hoyle state. For the latter, to evaluate the effect from dilute cold neutron matter, a polaron picture of α particle is introduced, where the impurity α particles polarize the majority neutron matter via interaction between α and neutrons. It is concluded that the Hoyle state in the neutron matter stabilizes and shrinks, which may impact the reaction rate for the nucleosynthesis. It is interesting to extend discussion of α cluster structure to heavier nuclear systems such as ^{16}O, ^{20}Ne, and ^{24}Mg. However, the macroscopic OCM is difficult for these nuclei because the numerical calculations become instable. Finally, we propose a novel approach to overcome the numerical instability toward applications to the heavier nuclear systems.

Chapter 1

Introduction

1.1 Clustering in nuclei

A nucleus is a many-body quantum system consisting of finite number of neutrons and protons correlating via nuclear interaction. The nuclear interaction has a strong attraction with a range of few fm[1)], which overwhelms the Coulomb repulsion between protons. The range of the interaction is comparable to the size of the nuclear systems and, therefore, nuclei have the saturation property for its density and the energy per nucleons. The saturation density and energy per nucleon are known to be approximately $0.16 \sim 0.17$ fm^{-3} [1] and 8 MeV[2)], respectively. The independent nucleon model is the basic description, particularly in the ground state, in which a nucleon occupies a single particle orbit in the mean field formed by the strong interactions of nucleons. This structure is called shell structure as a analogous of the atomic shell model of electrons.

In addition to the shell structure, based on the analogy of atomic molecules, cluster structure is essential to describe nuclear system, in which a nuclear system are composed of some subunits of several nucleons, clusters. The cluster structure can be considered to appear in the condition where correlations of nucleons in the clusters are much stronger than correlations between clusters, and then they are localized. In particular, the ^{4}He cluster, the α cluster, is the most basic cluster, which is made by the highly symmetric four nucleons, two protons and two neutrons. The α cluster has extraordinary large binding energy, and the first excited state is located at comparably high energy, ~ 20 MeV above the ground state [2], wheres the first excited states of normal nuclei are located at few MeV. Hence, α clusters often appear in the nuclear structure. The excited states of the self-conjugate nuclei of mass number $A = 4n$ $n \in \mathbb{N}$ with proton number $Z = 2n$ and neutron number $N = 2n$ are particularly characterized by the α clusters.

It is noted that these cluster structure generally appear in the vicinity of the thresholds where the nuclei break up into constituent clusters. For example, ^{8}Be namely two-α system, has the unstable ground state near the two-α threshold. Following this fact, one can consider the "rule" for cluster structure of the light nuclei, especially the self-conjugate $4n$ nuclei, which is called the Ikeda diagram [3] shown in the Fig. 1.1. The Ikeda diagram presents the possible cluster structures with threshold energy as a function of n of the self-conjugate $4n$ nuclei. The diagonal elements except for ^{8}Be represent the ground state that has the shell structure.

[1)] fm= 10^{-15} m

[2)] MeV= 10^6 eV

The clusters start to appear near the corresponding threshold energies, and they are finally all the minimum unit, α clusters (small circle symbols in the diagram). The diagram implies the possibility of systematic appearance of cluster structures in the nuclei, which makes the nuclear structure rich in variety.

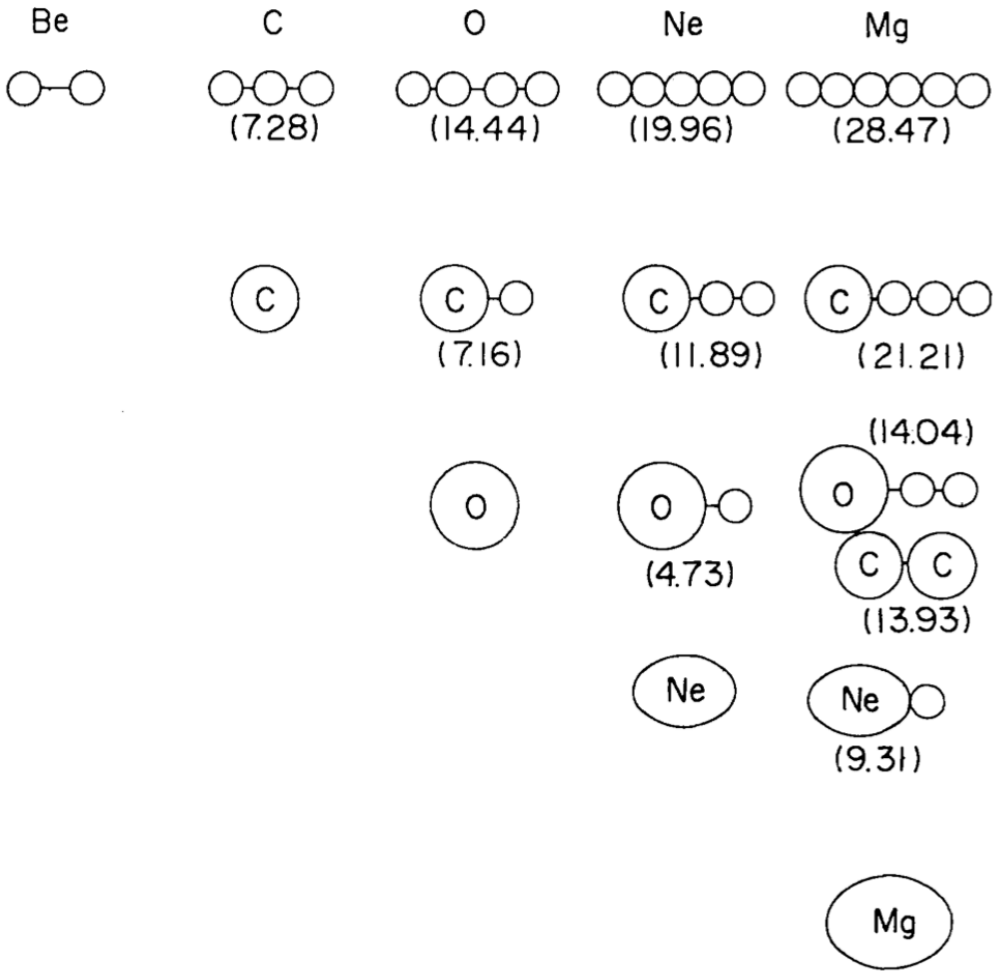

Figure 1.1: Ikeda diagram. The figure is taken from Ref. [3].

Not only the clustering in light nuclei, the clustering in medium-heavy mass nuclei is also paid attention recently. Typel [4] investigates the α cluster formation on the surface of the heavy nuclei by the generalized relativistic mean-field model with explicit cluster degree of freedom. According to the investigation, it is concluded that the α clustering happens in the low density neutron matter, approximately 1/10 of the nuclear saturation density. Motivated by this study, Tanaka *et al.* [5], conducted the experiment for α clustering phenomena in the surface region of Sn isotopes by the α knockout reaction and concluded the existence of α clusters in the nuclear surface. This α clustering in the neutron matter background is strongly related with the structure of neutron stars [6].

1.2 Hoyle state

1.2.1 α cluster structure in the Hoyle state

The first excited $J^\pi = 0^+$ state, Hoyle state [7] is one of the most important states in terms of cluster structure, which is located at 0.38 MeV above three-α threshold. Some studies on the Hoyle state by the shell model approach have been conducted, and found that describing the Hoyle state within the shell model is not easy [8]. We note that, very recently, the Hoyle state has been investigated by the Monte Carlo Shell Model approach by utilizing supercomputers in which the crossover picture of the shell structure and the cluster structure is presented [9], which is known as the duality [10, 11].

In 1950s, the linear chain like structure of the α clusters are suggested by Morinaga [12,13]. However, in 1970s and 80s, theoretical studies based on the cluster model gave negative results on the linear chain structure in the Hoyle state. On the contrary to the shell model calculation, the cluster model calculations such as the resonating group method (RGM) [14], generator coordinate method (GCM) [15], and orthogonality condition model (OCM) [16–18] successfully reproduce observed values [19–23] e.g., energy, α decay width, electromagnetic transition probabilities. In conclusion of these theoretical studies, well developed three α clusters are weakly coupled in the S orbit in the Hoyle state with significant amount of the $^8\mathrm{Be}(0^+) + \alpha$ configuration according to the analysis of α reduced width amplitude.

Inspired by the possibility for the Bose-Einstein condensation of α particles in a dilute symmetric nuclear matter [24, 25], Tohsaki *et al.* investigated the posibility of the same phenomena in a finite nuclear system, called α condensation in ^{12}C and ^{16}O [26]. In their investigation, the α condensation wave function for the $N\alpha$ cluster model within nucleons degree of freedom was newly suggested in which α particles are moving in the common mean-field,

$$|\Phi^{\mathrm{THSR}}_{N\alpha}\rangle = \left(C^+_\alpha\right)^N |\mathrm{vacuum}\rangle\,, \tag{1.1}$$

$$\langle \boldsymbol{r}_1 \cdots \boldsymbol{r}_N | \Phi^{\mathrm{THSR}}_{N\alpha}\rangle \propto \mathcal{A}\left[\exp\{-\nu(\boldsymbol{r}_1^2 + \cdots + \boldsymbol{r}_N^2)\}\phi(\alpha_1)\cdots\phi(\alpha_N)\right], \tag{1.2}$$

where C^+_α is the α particle creation operator, $\phi(\alpha_i)$ is the internal wave function of ith α cluster describing by the four nucleons occupying the $0s$ harmonic oscillator, $\boldsymbol{r}_i$ is the center-of-mass coordinate of the ith α particle, and $\mathcal{A}$ is the antisymmetrizer for all exchanges of nucleons. The relative motion of $N\alpha$ particles are described by the $0S$ harmonic oscillator with the size parameter ν. When ν is compact comparable to the size of α clusters, the $N\alpha$ cluster structure is melt and configure into the shell structure, which is consistent with the ground state property. On the other hand, when ν are large relative to the size of α clusters, α clusters occupy in the single orbit, indicating the α condensation. This kind of wave functions are named Tohsaki-Horiuchi-Schuck-Röpke (THSR) wave function after the initials of authors [26–28]. THSR wave function has been confirmed to have almost 100% overlap with the conventional wave functions which do not assume the α condensation [19–21]. Therefore, the α cluster structure in the Hoyle state is concluded to be the dilute α condensate state as a weakly interacting gas-like structure.

Besides the gas-like structure, geometric configuration of three-α system has been considered within the algebraic cluster model (ACM) [29–31]. In the ACM, three-α state is obtained from a group-theoretical construction of rotational and vibrational excitations of an equilateral triangle where the α particles are at the vertices. The Ref. [30] has investigated the

name	shape	group	Γ_{vib}	Patterns
linear =	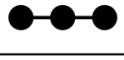	$\mathcal{D}_{\infty h}$	$A_{1g} + A_{1u} + E_{1u}$	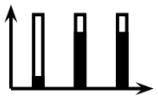
linear $\neq$		$\mathcal{C}_{\infty\nu}$	$2A_1 + E_1$	
equilateral		$\mathcal{D}_{3h}$	$A_1' + E'$	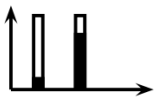
isosceles		$\mathcal{C}_{2\nu}$	$2A_1 + B_1$	
scalene		$\mathcal{C}_s$	$3A'$	

Figure 1.2: The table listing possible three-α geometric configurations based on the point group symmetry and its characteristic vibration modes, which is taken from the Ref. [32].

spectrum and the form factors of ^{12}C by the ACM and concluded that they are reasonably reproduced. Based the ACM, all possible configurations of three molecules can be listed [32] in Fig. 1.2. Using the idea of the ACM, Vitturi *et al.* [33] have investigated the performance of the simple geometric α-cluster model in which three α particles are set up in the equilateral triangle and transition densities are constructed according to the point-group symmetry. They found the nice agreement with the $^{12}\mathrm{C}(\alpha,\alpha')$ scattering data, especially for the cross section of the transition from the ground state to the Hoyle state.

It is interesting to mention about $J^\pi = 2_2^+$ state of ^{12}C which is the excited state of the Hoyle state. Owing to the recent great development of the experimental technics, 2_2^+ state has been attracted, which has been confirmed [34–37] at 2.59(6) MeV above the three-α threshold with the decay width of 1.01(15) MeV [38]. The 2_2^+ state is controversial as the candidate of the rotational excited state of the Hoyle state. The RGM and GCM calculations have found that $^8\mathrm{Be} + \alpha_{l=2}$ configuration is dominant in the structure of 2_2^+ state, thus it is rotational excited state of the Hoyle state [20, 21]. Freer *et al.* newly observed $J^+ = 4^+$ state locating at 13.3 MeV above the three-α threshold. They considered the rotational band consisting of the Hoyle state, the second 2^+ state, and newly observed 4^+ state, which is called the "Hoyle band" [39]. In the theoretical point of view, the Hoyle band still has not been well understood, even whether it exists or not. In the ACM context, the 2_2^+ state and the 4_2^+ state are obtained as the rotational band members under the A symmetry which is interpreted as the symmetry of the breathing vibration. Martìn-Lámbarri *et al.* see the agreement of the energy spectrum of ^{12}C between the ACM and experimental data, and finally concluded it is the evidence of the $\mathcal{D}_{3h}$ symmetry for three-α system and the Hoyle band [40]. On the

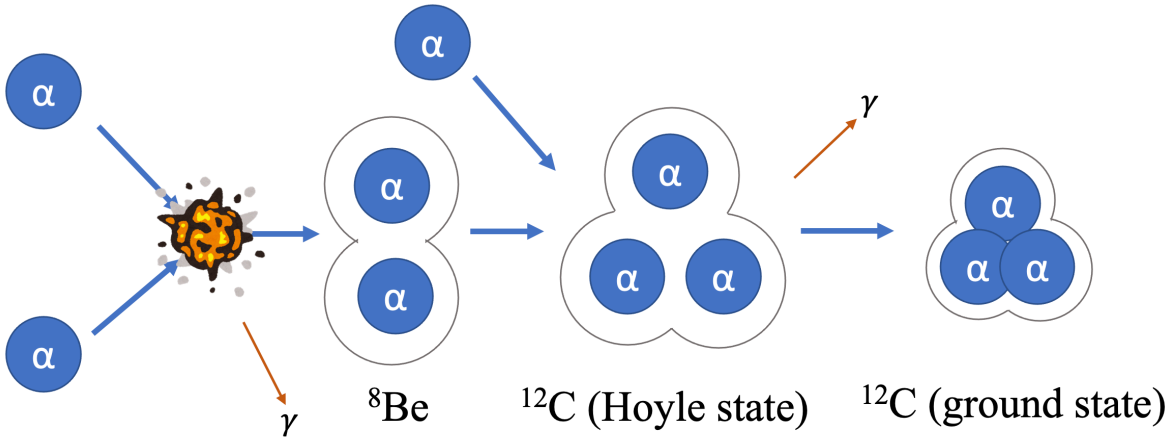

Figure 1.3: Schematic picture of the triple alpha process.

contrary, the theoretical study on 2_2^+ using the THSR wave function by Funaki [41] concluded that the Hoyle band is considered to be neither the simple rigid rotor nor the ^{8}Be+α rotation due to the specific condensation structure of the Hoyle state and strong coupling to the broad 0_3^+ state with ^{8}Be+α structure.

1.2.2 Hoyle state in the nucleosynthesis

The Hoyle state plays crucial role in the nucleosynthesis in the universe [7]. The abundance of the ^{12}C is explained via the triple alpha process whose schematic picture is described in the Fig 1.3. In the triple alpha process, especially the sequential process, an α particle sequentially captures two more α particles: two α particles form the resonant ground state of ^{8}Be which has a short life time, then one more α particle captured and the Hoyle state is formed. The Hoyle state very rarely decays to the ground state of ^{12}C with the γ-ray emission, which is rate-determining for the carbon synthesis. Hence, the abundance of the ^{12}C is mainly determined by the γ-decay rate of the Hoyle state. Through the triple alpha process, the nucleosynthesis can go heavier mass nuclei over the mass number $A = 5, 8$ where no stable nuclei exited. Therefore, the Hoyle state in the triple alpha process is important for the nucleosynthesis.

The triple alpha process usually occurs in normal stars where the temperature is about $10^8 \sim 10^9$ K and helium, created through the proton-proton chain reaction or the CNO cycle, are condensed enough to make a helium plasma. If the temperature in a star is rather higher than 10^9 K, contributions from the higher excited states than the Hoyle state such as $J^\pi = 2_2^+$ and 3_1^- are not negligible [42]. These contributions other than the Hoyle state have been recently deduced by the advance experiments [37], however it still has uncertainties.

The condensed helium plasma is also appeared in the outer layer of an X-ray bursting of the accreting neutron star [43] with lower temperature $\sim 10^8$ K in which helium is burned through the triple alpha process. In this helium plasma, the Coulomb repulsion is screened off at large distance due to a spherically symmetric polarization of surrounding degenerate electrons and nuclei [44], which can affect the triple reaction rate. Lai Hnin Phyu *et al.*, investigated the Coulomb screening effect to the structure and energy of the Hoyle state by using the three-α cluster model [45, 46]. The Coulomb screening was treated by correction to the Hamiltonian within the Debye-Hückel approximation. The correction of the Coulomb

screening effect results in changing of the Coulomb potential as follows:

$$V_{\text{Coul.}} \to V_{\text{Coul.}} \exp\left(-Cr\right), \tag{1.3}$$

where $V_{\text{Coul.}}$ is the Coulomb potential in vacuum, C is the inverse of the Coulomb screening length, and r is distance between α particles. In their conclusion, the Hoyle state become stable and compact because of the Coulomb screening effect. Moreover, the Q value of the triple alpha process shifts proportionally to the Coulomb screening length C, which is consistent with the conventional evaluation assuming point charged particles. It is interesting to consider the Hoyle state in different environment, e.g., dilute or condensed neutron matter medium in the same way.

1.3 Macroscopic cluster models

In this dissertation, three-α cluster model in the macroscopic framework is employed, in which the α clusters treated as structureless charged particles are degrees of freedom. The macroscopic cluster model have been employed for a long time because it has several advantages. First is that one can easily evaluate resonance states in proper way such as the complex scaling method (CSM) [47–49] and the analytic continuation of the coupling constant (ACCC) [50–52] because the dimension of freedom to be considered is small. Second is that one can extend to more complex multi-cluster systems such as ^{16}O+α+α or more-α systems if the Pauli principle between clusters are effectively taken into account. There mainly two types of macroscopic three-α model: one is the OCM and the other is the effective potential model. The difference between these two models is treatment of the Pauli principle of clusters. This section provides detail explanations of these models.

1.3.1 Orthogonality condition model

The OCM was originally introduced as the approximation for the treatment of the Pauli principle from the microscopic framework. Let the microscopic n-cluster wave function written as the antisymmetirzed multiplication of wave functions of internal-cluster and the their relative motion in the case where clusters are configured in the single spherical channel:

$$\Psi_{\text{micro}} = \mathcal{A}\left[\chi(\boldsymbol{x})\prod_{i=1}^{n}\phi_0(C_i)\right], \tag{1.4}$$

where $\boldsymbol{x} = (\boldsymbol{x}_1, \ldots, \boldsymbol{x}_{n-1})$ is the relative coordinate of the cluster center-of-mass, χ is the wave function of the relative motion, and $\phi_0(C_i)$ is internal wave function of the ith cluster. Note that the intrinsic relative coordinate for center-of-mass motion in n-cluster system is set of $(n-1)$ point vectors.[3)] The Ψ_{micro} can be rewritten as the linear combination of amplitude χ and, as a basis function, the test function $\Phi(\boldsymbol{t}, \boldsymbol{x})$ which pins clusters down to the specific coordinate $\boldsymbol{t} = (\boldsymbol{t}_1, \ldots, \boldsymbol{t}_{n-1})$,

$$\Psi_{\text{micro}} = \int d\boldsymbol{t}\chi(\boldsymbol{t})\Phi(\boldsymbol{t}, \boldsymbol{x}), \tag{1.5}$$

$$\Phi(\boldsymbol{t}, \boldsymbol{x}) = \mathcal{A}\left[\prod_{i=1}^{n-1}\delta(\boldsymbol{x}_i - \boldsymbol{t}_i)\prod_{j=1}^{n}\phi_0(C_j)\right]. \tag{1.6}$$

[3)] The relative coordinate is explained in 2.1 in detail.

Let us orthonormalization of the test functions by diagonalizing norm kernel $N(\boldsymbol{t},\boldsymbol{t}') \equiv \langle\Phi(\boldsymbol{t},\boldsymbol{x})|\Phi(\boldsymbol{t}',\boldsymbol{x})\rangle$,

$$\mathcal{N}\chi_k(\boldsymbol{t}) = \mu_k\chi_k(\boldsymbol{t}), \tag{1.7}$$

$$\mathcal{N}\chi_k(\boldsymbol{t}) \equiv \int d\boldsymbol{t}' N(\boldsymbol{t},\boldsymbol{t}')\chi_k(\boldsymbol{t}'), \tag{1.8}$$

where μ_k is eigenvalue which is always more or equal to 0 and χ_k is corresponding eigen function satisfying $\langle\chi_k|\chi_{k'}\rangle = \delta_{kk'}$. When $\mu_k = 0$, the wave function is obviously vanished, $\int d\boldsymbol{t}\chi_k\Phi(\boldsymbol{t},\boldsymbol{x}) = 0$. Such states are called the Pauli forbidden states. According to the orthonormality of the $\Psi_{\rm micro}$,

$$\langle\Psi_{\rm micro}|\Psi'_{\rm micro}\rangle = \iint d\boldsymbol{t}\ d\boldsymbol{t}'\chi^*(\boldsymbol{t})\mathcal{N}\chi'(\boldsymbol{t}') = 0 \quad \text{or} \quad 1, \tag{1.9}$$

the orthonormalized multi-cluster wave function in the OCM is approximately taken as $\Psi_{\rm OCM} = \mathcal{N}^{1/2}\chi$ [18]. It is noted that the $\Psi_{\rm OCM}$ does not contain the Pauli forbidden states.

The Pauli forbidden states ϕ_f are usually taken as the wave function of the harmonic oscillator with the common size parameter.[4)] If the internal wave function of clusters are described by the harmonic oscillator, relative wave function also can be described by the harmonic oscillator, which is the eigen function of $\mathcal{N}$ in eq. (1.8). Considering the shell structure of clusters in which nucleons move within the harmonic oscillator mean-field, total quanta is $N = 2n+l+\sum_i N(C_i)$, where $N(C_i)$ is the harmonic oscillator quanta of ith cluster. On the other hand, the lowest N_{min} is obtained from ground state shell configuration. Thus, the forbidden harmonic oscillator orbit is derived in the condition, $N > N_{min}$. For example, the inter-α case, total quanta is $N = 2n+l+N(\alpha)+N(\alpha)$, where $N(\alpha) = 0$ because the shell configuration of α is assumed to be $(0s)^4$. The lowest quanta of two-α system is $N_{min} = 4$ because the shell configuration of two-α system is $(0s)^4(0p)^4$. Then $0s$, $1s$, and $0d$ orbits which do not satisfy the condition $2n + l > 4$ are found to be forbidden.

In the macroscopic framework, OCM calculation is dedicated for obtaining wave function of the relative motion $\Psi_{\rm OCM}$ under the condition with Pauli forbidden states, ϕ_f orthogonal to the $\Psi_{\rm OCM}$, $\langle\phi_f|\Psi_{\rm OCM}\rangle$=0. This can be archived in straightforward way by introducing the exclusion operator defined as

$$\Lambda = 1 - \sum_{i\in f} |\phi_i\rangle \langle\phi_i| , \tag{1.10}$$

that projects the total wave function on the Pauli allowed space. However, the practical calculations become required large calculation cost in the case of more than three-cluster system because one must apply this projection operator for all inter-cluster pairs and number of terms is very large. For the feasible calculations, Kukulin and Pomenertsev suggested the pseudopotential [54] defined as

$$\Gamma = \gamma \sum_{i\in f} |\phi_i\rangle \langle\phi_i| . \tag{1.11}$$

By taking γ large number, projected Pauli forbidden states can be excluded numerically. γ is usually taken as $10^4 \sim 10^5$ MeV. However, it usually causes numerical instability. The OCM has been employed for the three-α system [53, 55–57] and the four-α system [58, 59], although OCM calculations for five- or more-α systems has not been reached yet due to the numerical instability due to the Γ.

[4)] Choices of the Pauli forbidden states are discussed in the Ref. [53].

1.3.2 Shallow potential model

On the contrary of the OCM, there is phenomenological cluster model, called shallow potential model, in which the Pauli principle is effectively described as the core repulsion [60]. To reproduce the α-α phase shifts for inter-α angular momentum $l = 0$ and 2, the potential between α particles are local but l-dependent. Numerical calculations with this model are more stable than the OCM. However, it is known that the internal behavior of the wave function is different from that of the OCM, which may affect the physical values [56].

1.4 Aim of this dissertation

We mentioned overviews of background of ^{12}C in this chapter. In this dissertation, the ^{12}C is comprehensively studied by precise three-α cluster model wave functions with three topics, three-α structure of ^{12}C, the Hoyle state in astrophysical environment, and the new method to overcome the numerical instability of the OCM calculations toward extended investigations from ^{12}C. In the next chapter 2, we explain how to obtain the precise few-body wave functions. At the end of this chapter, we describe motivations and aim of these three investigations for ^{12}C.

In chapter 3, we describe the analysis of three-α cluster structure in the spectrum of ^{12}C within the OCM. According to the ACM, geometrical configurations of three-α can be classified under the $\mathcal{D}_{3h}$ point group symmetry as we mentioned in 1.2. This motivate us to investigate density distributions of three-α system, such as one-body density and two-body density which visualizes the geometric structure directory. Together with other physical analysis, for example harmonic oscillator quanta of inter-α motions, momentum distribution, and partial wave component, we discuss the three-α structure. To extend the discussion to the resonant states, e.g., the Hoyle state and 2_2^+ state, one need to obtain those wave functions with a square integrable form. We evaluated these states by introducing a confining potential.

A study of controversial Hoyle band is also the motivation of this investigation, which has not reached consensus on its existence both theoretically and experimentally. Recently, Smith *et al.*, deduced the a limit for the direct decay branching ratio of the Hoyle state under the assumption that the intrinsic structure of 0_2^+ and 2_2^+ are the same, which is related to the direct triple alpha process. This assumption is reasonable within the ACM description. However, investigation by the THSR wave function, as mention in 1.2, concluded that 2_2^+ is not a simple rigid rotor of the Hoyle state with keeping its intrinsic structure. To settle this deviation, we analyze the wave functions of the Hoyle state and 2_2^+ state that is not assumed $\mathcal{D}_{3h}$ symmetry.

In chapter 4, we describe the study of three-α system in the cold dilute neutron matter. In 1.2.2, we mentioned the Coulomb screening effect on the Hoyle state in the astrophysical environment where the degenerate electron plasmas are surrounded. This environment might be realized in the X-ray bursting of a accreting neutron star. In the same way, the environment where α particles are immersed in the cold dilute neutron matter might be realized in the core collapse supernovae [61] and neutron star mergers, which has been recently observed through the gravitational wave [62]. This motivates us to study the Hoyle state in cold dilute neutron matter, which can impact on the astrophysical modeling [63]. The three-α system immersed in the dilute neutron matter is interesting for not only the astrophysics but also the clustering phenomena of medium-heavy mass nuclei. It is related to the experiments exploring α clusters

in the Sn isotope by the alpha knockout reaction [5].

In chapter 5, we propose a novel macroscopic cluster model approach. As mentioned in 1.3.1, the Pauli principle in the OCM calculation is carried out by the pseudopotential Eq.(1.11), which makes numerical calculations unstable. This numerical instability prevents us from reaching more complex or heavier multi-cluster system. In fact, only two OCM studies for the four-α system have been reported [58, 59] and one of them could not reach the converged result. To overcome this instability, we proposed the novel basis function for macroscopic cluster model, starting with the microscopic cluster wave function. We show the novel basis function is efficient and calculation cost for the three-α system drastically reduced. Possibilities for the more complex multi-cluster systems are indicated.

Finally, we summarize these works and conclude the dissertation as the comprehensive study of the ^{12}C by the precise three-α cluster model wave functions in chapter 6.

Chapter 2

Stochastic variational method

In this chapter, the methodology to obtain precise few-body wave functions. Basically, the motion of the isolated quantum few-body system is governed by the Hamiltonian, for example, the Hamiltonian for intrinsic motion of a N-body system is generally written as

$$H = \sum_{i=1}^{N} \frac{\boldsymbol{p}_i^2}{2m_i} - T_{cm} + \sum_{i>j=1}^{N} V_{ij}, \tag{2.1}$$

where $\boldsymbol{p}_i$, m_i T_{cm}, and V_{ij} are momentum operator of the ith particle[1)], mass parameter of the ith particle, the center-of-mass motion, and an interaction between the ith and jth particle. One can obtain the eigen states of the considering few-body system by diagonalizing its Hamiltonian within some specific space spanned by the basis functions.

According to the variational principle or the Ritz theorem, the "exact" solution of the Schrödinger equation can be obtained virtually by the variational method. Let $\Psi(\boldsymbol{X})$ the wave function of the N-body system where the $\boldsymbol{X}$ represents a set of all degrees of freedom to specify the motion of the system. $\Psi(\boldsymbol{X})$ is expressed as the linear superposition of the basis functions characterized by the set of variational parameters α_i, $\psi(\boldsymbol{X}, \alpha_i)$:

$$\Psi(\boldsymbol{X}) = \sum_{i=1}^{K} C_i \ \psi(\boldsymbol{X}; \alpha_i). \tag{2.2}$$

The set of the coefficient $\{C_i\}$ is determined by solving the generalized eigenvalue problem,

$$\sum_{i=1}^{K} (H_{ij} - EB_{ij}) C_j \qquad (i = 1, \ldots, K), \tag{2.3}$$

where the matrix elements H_{ij} and B_{ij} are defined as

$$H_{ij} = \langle \phi(\alpha_i; \boldsymbol{X}) | H | \phi(\alpha_j; \boldsymbol{X}) \rangle \tag{2.4}$$

$$B_{ij} = \langle \phi(\alpha_i; \boldsymbol{X}) | \phi(\alpha_j; \boldsymbol{X}) \rangle \,. \tag{2.5}$$

The set of the basis functions is not necessary to be orthogonal each other: the overlap matrix B_{ij} is not always the identity matrix.

[1)] Hereafter, spatial vectors are descried in a bold.

2.1 Coordinate

Let us define the coordinate for the N-body system. It is important to take care of the separation of center-of-mass motion from the intrinsic motion when one defines the coordinate. The relative coordinate and the center-of-mass coordinate are convenient for description of the intrinsic motion, which is written as $\tilde{\boldsymbol{x}} = (\boldsymbol{x}_1, \ldots, \boldsymbol{x}_N)$[2] $\boldsymbol{x}_N$ is taken as the center-of-mass coordinate here. In general, the relative coordinates are related to the single particle coordinate $\tilde{\boldsymbol{r}} = (\boldsymbol{r}_1, \ldots, \boldsymbol{r}_N)$ by the linear transformation,

$$\boldsymbol{x}_i = \sum_{j=1}^{N} U_{ij}\boldsymbol{r}_j, \quad \boldsymbol{r}_i = \sum_{j=1}^{N} \left(U^{-1}\right)_{ij} \quad (i = 1, \ldots, N), \tag{2.6}$$

where U_{ij} is a $N \times N$ matrix. There are several choices of the U_{ij}. Among them, the relative Jacobi coordinate is useful, in which U_{ij} is defined as

$$U = \begin{pmatrix} 1 & -1 & 0 & \cdots & 0 \\ \frac{m_1}{m_{12}} & \frac{m_2}{m_{12}} & -1 & \cdots & 0 \\ \vdots & & & & \vdots \\ \frac{m_1}{m_{12\cdots N-1}} & \frac{m_2}{m_{12\cdots N-1}} & \cdots & \cdots & -1 \\ \frac{m_1}{m_{12\cdots N}} & \frac{m_2}{m_{12\cdots N}} & \cdots & \cdots & \frac{m_N}{m_{12\cdots N}} \end{pmatrix}, \tag{2.7}$$

where $m_{12\cdots i} = m_1 + m_2 + \cdots + m_i$.

The single particle momentum $\boldsymbol{p}_i$ is also described as the linear transformation of U to the momentum of relative motion, $\boldsymbol{\pi}_j = -i\hbar\partial/\partial\boldsymbol{x}_j$, conjugate to the coordinate $\boldsymbol{x}_j$:

$$\boldsymbol{p}_i = \sum_{j=1}^{N} U_{ji}\boldsymbol{\pi}_j, \quad \boldsymbol{\pi}_i = \sum_{j=1}^{N} \left(U^{-1}\right)_{ji} \boldsymbol{p}_j \quad (i = 1, \ldots, N). \tag{2.8}$$

In this way, the center-of-mass motion is naturally expressed as $T_{cm} = \boldsymbol{\pi}_N^2/(2m_{12\cdots N})$. Then the kinetic energy of the intrinsic motion is described as

$$\sum_{i=1}^{N} \frac{\boldsymbol{p}_i^2}{2m_i} - T_{cm} = \frac{1}{2}\sum_{i=1}^{N-1}\sum_{j=1}^{N-1} \Lambda_{ij}\boldsymbol{\pi}_i \cdot \boldsymbol{\pi}_j, \tag{2.9}$$

where Λ_{ij} is the reduced mass matrix defined as

$$\Lambda_{ij} = \sum_{k=1}^{N} U_{ij}U_{jk}\frac{1}{m_k} \qquad (i, j = 1, \ldots, N-1). \tag{2.10}$$

It is convenient to express the single particle coordinate relative to the center-of-mass coordinate $\boldsymbol{r}_i - \boldsymbol{x}_N$, the inter-particle coordinate $\boldsymbol{r}_i - \boldsymbol{r}_j$, and the momentum difference $\boldsymbol{p}_i - \boldsymbol{p}_j$ in terms of $\boldsymbol{x}$ and $\boldsymbol{\pi}$.

$$\boldsymbol{r}_i - \boldsymbol{x}_N = \sum_{k=1}^{N-1} (U^{-1})_{ik}\boldsymbol{x}_k \equiv \widetilde{w^{(i)}}\boldsymbol{x}, \tag{2.11}$$

$$\boldsymbol{r}_i - \boldsymbol{r}_j = \sum_{k=1}^{N-1} \left((U^{-1})_{ik} - (U^{-1})_{jk}\right) \boldsymbol{x}_k \equiv \widetilde{w^{(ij)}}\boldsymbol{x}, \tag{2.12}$$

$$\frac{1}{2}(\boldsymbol{p}_i - \boldsymbol{p}_j) = \frac{1}{2}\sum_{k=1}^{N-1} (U_{ki} - U_{kj})\, \boldsymbol{\pi}_k \equiv \widetilde{\zeta^{(ij)}}\boldsymbol{p}, \tag{2.13}$$

[2] The tilde symbol stands for a transpose of a matrix if unless otherwise noted.

where $w^{(i)}$, $w^{(ij)}$, and $\zeta^{(ij)}$ are $(N-1)\times 1$ vectors. These short notations are useful when one considers the matrix elements of the Hamiltonian or physical operators, such as a two-body potential and correlation functions.

The relative Jacobi coordinate can be easily One of the most advantages of the relative Jacobi coordinate

2.2 Correlated Gaussian with the global vector

Choice of a basis function is important for the variational calculation. If the basis function is appropriately chosen, the practical calculation is efficient and precise in a numerical way. There three conditions to impose the basis function for the few-body systems: the first is that spatial behavior and correlations between particles are well described, the second is that the angular part of the basis function is good to the arbitrary total angular momentum, and the third is that the matrix elements can be analytically evaluated.

As the best choice of the basis function, I introduce the correlated Gaussian basis function (CG) with the global vector [64] defined as

$$\psi(\boldsymbol{x};A,u)=\exp\left(-\frac{1}{2}\tilde{\boldsymbol{x}}A\boldsymbol{x}\right)\mathcal{Y}_{LM}(\boldsymbol{v})\qquad \boldsymbol{v}=\tilde{u}\boldsymbol{x}, \tag{2.14}$$

where A is a positive definite symmetric $(N-1)\times(N-1)$ matrix, $\mathcal{Y}_{LM}$ is the solid spherical harmonics of the total angular momentum L and its z-projection M, $\mathcal{Y}_{LM}(\boldsymbol{v})=|\boldsymbol{v}|^L Y_{LM}(\hat{\boldsymbol{v}})$. $\tilde{\boldsymbol{x}}A\boldsymbol{x}$ is the quadratic form, which is a short writing of $\sum_{i=1}^{N-1}\sum_{j=1}^{N-1}A_{ij}\boldsymbol{x}_i\cdot\boldsymbol{x}_j$. u is the $(N-1)$ vector, so called the global vector, and practically taken as the variational parameters with its length unity at random.

The CG is good spacial description for N-body systems, which is extended from the normal Gaussian. Notably, the CG explicitly describes the correlations between particles via the off-diagonal part of the A. This can be easily shown by the expansion of the CG,

$$\exp\left(-A_{ij}\boldsymbol{x}_i\boldsymbol{x}_j\right)=\sum_{n=0}^{\infty}\frac{(-A_{ij})^n}{n!}(\boldsymbol{x}_i\cdot\boldsymbol{x}_j)^n \tag{2.15}$$

$$(\boldsymbol{x}_i\cdot\boldsymbol{x}_j)^n=\sum_{2k+n=n}\frac{4\pi(2k+l)!}{2^k k!(2k+2l+1)!!}\boldsymbol{x}_i^{2k}\boldsymbol{x}_j^{2k}(-1)^l\sqrt{2l+1}\left[\mathcal{Y}_l(\boldsymbol{x}_i)\times\mathcal{Y}_l(\boldsymbol{x}_j)\right]_{00}, \tag{2.16}$$

in which ith and jth particle are correlated with all possible angular momenta. The angular motion of the few-body system is properly described by the solid spherical harmonics with the global vectors. This can be shown by the expansion of the solid spherical harmonics with global vector in terms of the tensor coupling of the spherical harmonics of the single coordinate, for example of three-body system:

$$\mathcal{Y}_{LM}(u_1\boldsymbol{x}_1+u_2\boldsymbol{x}_2)=\sum_{l=0}^{L}\sqrt{\frac{4\pi(2L+1)!}{(2L+1)!(2L-2l+1)}}u_1^{2k+l}u_2^{2k+l}\left[\mathcal{Y}_l(\boldsymbol{x}_1)\times\mathcal{Y}_{L-l}(\boldsymbol{x}_2)\right]_{LM}. \tag{2.17}$$

The solid spherical harmonics of the arbitral N-body system also can be expanded in the same way. Therefore, the CG with the global vector expression is suitable for description of the spatial motion of the N-body system having the arbitral angular momentum.[3)]

[3)] The expression with the single global vector can describe only natural party state, e.g., 0^+, 1^-, and 2^+. To extend to the unnatural party states, e.g, 0^-, 1^+, and 2^-, double or triple global vectors expression is implemented [65, 66].

The matrix elements of the CG with the global vector can be analytically evaluated. By using the generating function of the CG, evaluation of the matrix elements becomes simpler and systematic. The generating function of the CG, g, is realized with an auxiliary vector $\boldsymbol{s} = (\boldsymbol{s}_1, \ldots, \boldsymbol{s}_N)$ in the form as

$$g(\boldsymbol{x}; A; \boldsymbol{s}) = \exp\left(-\frac{1}{2}\tilde{x}A\boldsymbol{x}\tilde{\boldsymbol{s}}\boldsymbol{x}\right). \tag{2.18}$$

The CG and the generating function are related with the integral as following:

$$\exp\left(-\frac{1}{2}\tilde{\boldsymbol{x}}A\boldsymbol{x}\right)\mathcal{Y}_{LM}(\boldsymbol{v}) = \frac{2^k k!(2k+2l+1)!!}{4\pi(2k+l)!}\int d\boldsymbol{e}Y_{LM}(\boldsymbol{e})\left(\frac{d^L}{d\lambda^L}g(\boldsymbol{x}; A; \lambda\boldsymbol{e}u)\right)_{\lambda=0,|\boldsymbol{e}|=1} \tag{2.19}$$

Following this equation, one can evaluate matrix elements of the operator $\mathcal{O}$ from the element $\langle g(\boldsymbol{x}; A_i; \lambda_i\boldsymbol{e}_i u_i)|\mathcal{O}|g(\boldsymbol{x}; A_j; \lambda_j\boldsymbol{e}_j u_j)\rangle$. Evaluations of matrix elements for concrete operators are described in the Appendix.

The CG is easily symmetrized or antisymmetrized for the changing of identical particles to satisfy the bosonic and fermionic properties. In the relative Jacobi coordinate, the (anti)symmetrization can be easily achieved by the linear transformation of permutation operation,

$$P = \begin{pmatrix} 1 & 2 & \cdots & N \\ p_1 & p_2 & \cdots & p_N \end{pmatrix} \tag{2.20}$$

which transforms the ith single-particle coordinate to the p_ith single particle coordinate, $\boldsymbol{r}_i \to \boldsymbol{r}_{p_i}$ as $P\boldsymbol{x} = T_P\boldsymbol{x}$, where the transformation matrix of the permutation P is defined as:

$$(T_P)_{ij} = \sum_{k=1}^{N} U_{ik}\left(U^{-1}\right)_{p_k j} \quad (i, j = 1, \ldots, N-1). \tag{2.21}$$

Using this linear transformation, one can define the symmetrizer $\mathcal{S}$ and the antisymmetrizer $\mathcal{A}$ as:

$$\mathcal{S} = \frac{1}{N!}\sum_P P, \tag{2.22}$$

$$\mathcal{A} = \frac{1}{N!}\sum_P \mathrm{sgn}(P)P, \tag{2.23}$$

where sgn stands for the parity of the permutation.

2.3 Stochastic Variational Method

To obtain the precise wave function, one needs to optimize the variational parameters in the basis functions. The A has the $N(N-1)/2$ variational parameters and u has $N-2$ variational parameters. In particular, optimization of the A is essential for the numerical calculation. Here, I introduce two ideas for a parameter optimization. One is called the geometric progression method in which the variational parameters in the A are taken as the series of the geometric progression, e.g., $A_{ij} = (r_0 r^{k-1})^{-2}$, where initial value r_0 (length unit) and the ratio r. Note that the geometric progression series are in the length unit. When the length of the geometric progression series is taken to be $k = 1, \ldots, m$ for every matrix element

in the A, the dimension of basis function becomes $m^{N(N-1)}$. The initial value and the ration are usually empirically determined to obtain the minimum energy. The geometric progression method is advantageous for spanning space entirely.

The other is called the stochastic variational method [67] in which the variational parameters are optimized by the competitive selection. If $A_1, \dots A_{k-1}$ have been already optimized, competitive selection for optimization of A_k is performed by following steps:

1. Generating n different candidates for the kth variational parameter $(A_k^1, \dots, A_k^n)$ randomly.
2. Solving k-dimensional generalized eigenvalue problem including candidates $(A_k^1, \dots, A_k^n)$ and corresponding eigen-energies $(E^1, \dots, E^n)$ are determined.
3. The A_k that reproduce the lowest energy among $(E^1, \dots, E^n)$ is selected as the kth variational parameter.
4. Moving to the $k+1$th variational parameter.

There are several methods to generate candidates of A_k, I introduce two good methods. One is the method that the candidates of the A_k is generated from the inter-particle parameter a_{ij},

$$\sum_{j>i=1}^{N} a_{ij}(\boldsymbol{r}_i - \boldsymbol{r}_j)^2 = \tilde{\boldsymbol{x}} \left(\sum_{j>i=1}^{N} a_{ij} w^{(ij)} \widetilde{w^{(ij)}} \right) \boldsymbol{x} = \tilde{\boldsymbol{x}} A_k \boldsymbol{x}. \tag{2.24}$$

In this method, once a_{ij} is randomly generated, then A_k is determined. The other method is by using rotational operator $\mathcal{R}$. The candidate of A_k is generated via following steps: generating a diagonal matrix A_k^{diag} randomly and operating rotational transformation in $(N-1)$ dimensional space, $A_k = \mathcal{R} A_k^{\mathrm{diag}}$. The former method is easy to apply for arbitral-body systems. The latter method can cover wide model space in equally likely way, especially for the three-body system.

Chapter 3

Geometric configuration in the spectrum of ^{12}C

We investigate geometric configurations of α clusters in the spectrum of ^{12}C within three-α OCM. In particular 2_2^+ is analyzed in detail, which has been discussed as a rotational band member of the Hoyle state. The ground and excited 0^+ and 2^+ states are described by a three-α cluster model. The three-body Schrödinger equation with orthogonality conditions is accurately solved by the stochastic variational method with correlated Gaussian basis functions. To analyze the geometric configuration in a convenient form, we introduce a confining potential. The two-body density distributions together with the spectroscopic information clarify the structure of these states. We find that main configurations of both the second 0^+ and 2^+ states are acute-angled triangle shapes originating from the ^{8}Be(0^+)+α configuration. However, the $^8\mathrm{Be}+\alpha$ components in the second 2^+ state become approximately 2/3 because the ^{8}Be subsystem is hard to excite, indicating that the state is not an ideal rigid rotational band member of the Hoyle state.

3.1 Background of the structure of ^{12}C

The background of the structure of ^{12}C, especially for the Hoyle band, is described again in this section. A lot of theoretical studies for the structure of ^{12}C have been conducted, using the various model. According to the OCM calculation by Yamada and Schuck [57] the ground state and 2_1^+ states are understood shell-like structure having $SU(3)$ symmetry. In the $SU(3)$ symmetry shell structure, the partial wave component of the ground state is equally distributed to l =0,2, and 4 inter-α partial waves. Following this three-equal distributions, the momentum distribution has three peaks with same amplitudes. Related with this, the density distributions have the nodal behavior in the internal region.

On the other hand, the Hoyle state could not explained by the shell model [8]. For more than half a century, the Hoyle state has been studied by cluster models, which could reproduce experimental energy [22]. As the state has a significant amount of the ^{8}Be(0^+)+α configurations [19, 20, 22, 23], the Hoyle state decays dominantly via sequential decay process $^8\mathrm{Be}(0^+)\alpha \to 3\alpha$ [68]. In addition to the ^{8}Be+α structure, Ref. [26] claimed that the Hoyle state has the α-condensate like character, where three α bosons occupy in the same S orbit. The structure of the Hoyle state has also been discussed in terms of geometric configurations of three-α particles based on the algebraic cluster model (ACM) [30, 32, 33]. Fully microscopic

calculations predicted a significant amount of α cluster configurations in the Hoyle state [69, 70]. Very recently, prominent three-α cluster structure configurations were confirmed in the Monte Carlo Shell Model approach [9].

The search for other excited cluster states with some analogy to the Hoyle states has attracted interest. The structure of second $J^\pi = 2^+$ state is controversial as it can be a candidate of a rotational excited state of the Hoyle state forming the "Hoyle band" [39]. Experimentally, the 2_2^+ state was confirmed [34–37] at 2.59(6)MeV above the three-α threshold with the decay width of 1.01(15)MeV [38]. The idea of the Hoyle band has attracted attention. Ref. [71] deduced a limit for the direct decay branching ratio of the Hoyle state under the assumption that the intrinsic structure of 0_2^+ and 2_2^+ are the same. Theoretically, the 2_2^+ state has only been recognized as having dominant $^8\mathrm{Be}(0^+) + \alpha$ configurations, in which its intrinsic structure is a weakly-coupled ^{8}Be plus an α particle with the angular momentum of 2 [**?**, 19, 70]. In analogy to the Hoyle state, the α-mean field character in the 2_2^+ state can be considered, in which one α particle is excited to the D orbit [57, 72] but Ref. [41] argued that the 2_2^+ state is not a simple rigid rotational excited state based on the analysis of the energy levels obtained by the microscopic three-α cluster model. In the context of the ACM, the 2_2^+ state is interpreted as the rigid rotational excited state of the Hoyle state in which three α particles geometrically form an equilateral triangle and vibrate with the $\mathcal{D}_{3h}$ symmetry [31]. To confirm whether this state belongs to the Hoyle state, a certain degree of similarity in the intrinsic structure should be observed. This motivates us to conduct a detailed study to clarify the extent of similarity between the structure of the second 0^+ and 2^+ states.

To settle this argument, in this chapter, we study geometric configurations of three-α particles in the second 2^+ state and compare its structure with the second 0^+ Hoyle state using accurate three-α wave functions. $^8\mathrm{Be} + \alpha$ components are analysed to clarify the origin of these configurations.

In this chapter, the four physical states, $J^\pi = 0_1^+$, 0_2^+, 2_1^+ and 2_2^+ of ^{12}C are studied within the three-α cluster model. In the next section, we explain our approach. Fully converged solutions are obtained by correlated Gaussian expansion with the stochastic variational method which is explained in the Chapter 2. Geometric configurations of the α particles are visualized by calculating two-body density distributions as well as other physical quantities. To evaluate these physical quantities of the state with rather wide decay width such as the second 2^+ state, we introduce a confining potential. The details are given in Sec. 3.2.2. In Sec. 4.3, we show the numerical results and analysis. Finally, we conclude the structure of the 2_2^+ state in Sec. 3.4.

3.2 Method

3.2.1 Three-α cluster model

The wave functions of ^{12}C are obtained by the SVM with fully symmetrized CG to take into account bosonic property of the α particles. The three-α Hamiltonian reads

$$H = \sum_{i=1}^{3} T_i - T_{\mathrm{cm}} + \sum_{i>j=1}^{3} (V_{2\alpha}^{ij} + V_{\mathrm{Coul.}}^{ij}) + V_{3\alpha}, \tag{3.1}$$

where T_i is the kinetic energy of the ith α particle. The kinetic energy of the center-of-mass motion T_{cm} is subtracted. The mass parameter in the kinetic energy terms and the elementary

charge in the Coulomb potential ($V_{\rm Coul.}$) are taken as $\hbar^2/m_\alpha = 10.654$ MeVfm^2 and $e^2 = 1.440$ MeVfm, respectively. Two-α interaction $V_{2\alpha}$ is taken as the same used in Ref. [73], which is derived by a folding procedure using an effective nucleon-nucleon interaction. We employ the three-alpha interaction $V_{3\alpha}$ depending on the total angular momentum J^π reproducing the binding energies as was used in Ref. [55]. Here we adopt the OCM which is explained in 1.3.1. To impose the orthogonality condition to the Pauli forbidden states (f.s.), we introduce in the Hamiltonian the pseudopotential eq. (5.1) for all inter-α pairs:

$$V_{\rm P} = \sum_{i>j=1}^{3} \Gamma_{ij}. \tag{3.2}$$

We adopt the harmonic oscillator wave functions for the forbidden states with the size parameter $\nu = 0.2575$ fm^{-2} [73] reproducing the size of the α particle. In this chapter, we take $\gamma = 10^5$ MeV. The forbidden state components of the resulting wave functions are found to be in the order of 10^{-5}. For the detail numerical settings, reader is referred to the Refs. [45,110].

3.2.2 Confining potential

We treat resonant 0_2^+ and 2_2^+ states as a bound state. This is the so-called bound-state approximation and works well for a state with a narrow decay width such as the 0_2^+ state (Expt.: $\Gamma = 8.5 \times 10^{-3}$ MeV [74]), while for 2_2^+ it is hard to obtain the physical state with a simple basis expansion [75] as it has somewhat large decay width (Expt.: $\Gamma = 1.01(15)$ MeV [36]). To estimate the resonant energy, the analytical continuation in the coupling constant [76] is useful but does not provide us with the wave function. Nevertheless, a square-integrable wave function of resonant states is useful to analyze its structure. A confining potential (CP) method [77, 78] is suitable for this purpose, as we can treat a resonance state as a bound state inside of the CP. To get a physical resonant state in the bound-state approximation, we introduce a confining potential in the following parabolic form [77] as

$$V_{\rm CP} = \sum_{i=1}^{3} \lambda\Theta(|\boldsymbol{r}_i - \boldsymbol{x}_3| - R_0)(|\boldsymbol{r}_i - \boldsymbol{x}_3| - R_0)^2, \tag{3.3}$$

where $\Theta(r)$ is the Heaviside step function,

$$\Theta(x) = \begin{cases} 1 & (x > 0) \\ 0 & (x < 0) \end{cases}, \tag{3.4}$$

which is shown in Fig. The strength λ and range R_0 parameters of the confining potential are real numbers and have to be taken appropriately.

Here we investigate the stability of the energies as well as root-mean-square (rms) radii $R_{\rm rms} = \sqrt{\langle\Psi_{JM}|(\boldsymbol{r}_1 - \boldsymbol{x}_3)^2|\Psi_{JM}\rangle}$ of the 0_1^+, 0_2^+, 2_1^+ states against changes of λ and R_0. Figure 3.2 shows the energies and rms radii of the 0_1^+, 0_2^+, 2_1^+ and 2_2^+ states with different R_0. The strength of the confining potential is set to be $\lambda = 100$ MeV/fm. Since the R_0 value is taken large enough, the energies and the rms radii of the bound states, 0_1^+ and 2_1^+, do not depend too much on these parameters. Even for the resonant 0_2^+ and 2_2^+ states, we find that the fluctuations of the energies are small about 0.1 MeV and 0.6 MeV, respectively, in the range of $R_0 = 8$–10 fm. This is reasonable considering the facts that the 0_2^+ state has quite small decay width and the 2_2^+ state has larger decay width. The magnitude of the radius

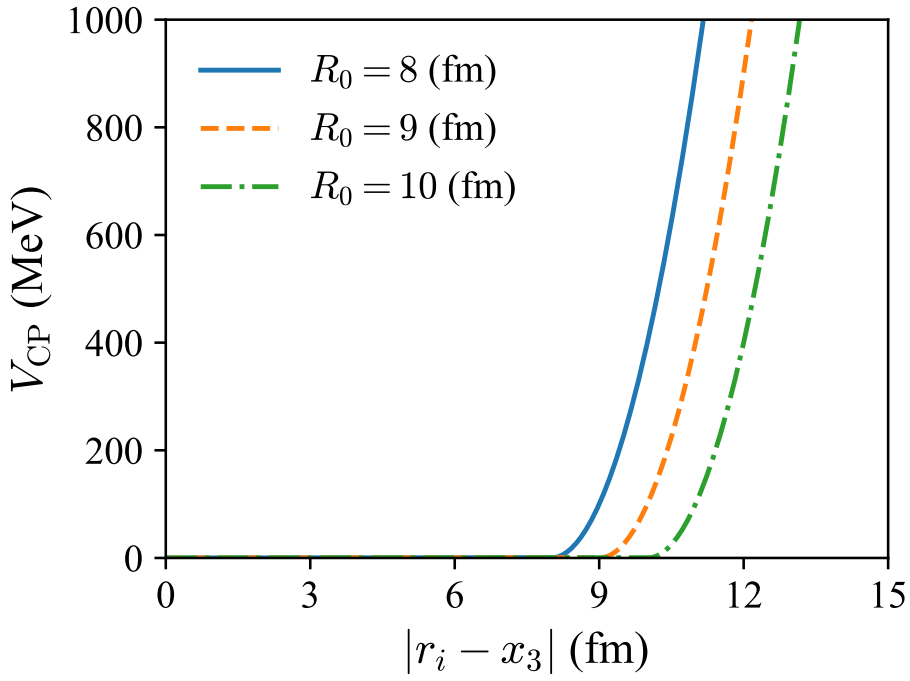

Figure 3.1: The plots of the confining potential with parabolic form in eq. (3.3).

Table 3.1: Calculated energies measured from the three-α threshold and rms radii of the 0^+_1, 0^+_2, 2^+_1, and 2^+_2 states.

J^π	E (MeV)	$R_{\rm rms}$ (fm)
0^+_1	-7.25	1.71
0^+_2	0.84	3.44
2^+_1	-2.92	1.93
2^+_2	2.32	3.50

fluctuation against to the changes of R_0 is about ≈ 0.3 fm for the 0^+_2 state and ≈ 0.5 fm for the 2^+_2 state. We also made the same analysis by strengthening the strength λ by 10 times and a similar plot was obtained. Hereafter, we use the results with $R_0 = 9$ fm, $\lambda = 100$ MeV/fm^2.

Table 3.1 lists the calculated energies and rms radii. These energy values can be compared with the real parts of the complex energies obtained by the complex scaling method (CSM) [55]. The energies are 0.75 and 2.24 MeV for 0^+_2 and 2^+_2 states, respectively, which are in good agreement with our results. Finally, we obtain the rms radii of the 0^+_2 and 2^+_2 states using these obtained wave functions. They are found to be similar and significantly large compared to the 0^+_1 and 2^+_1 states.

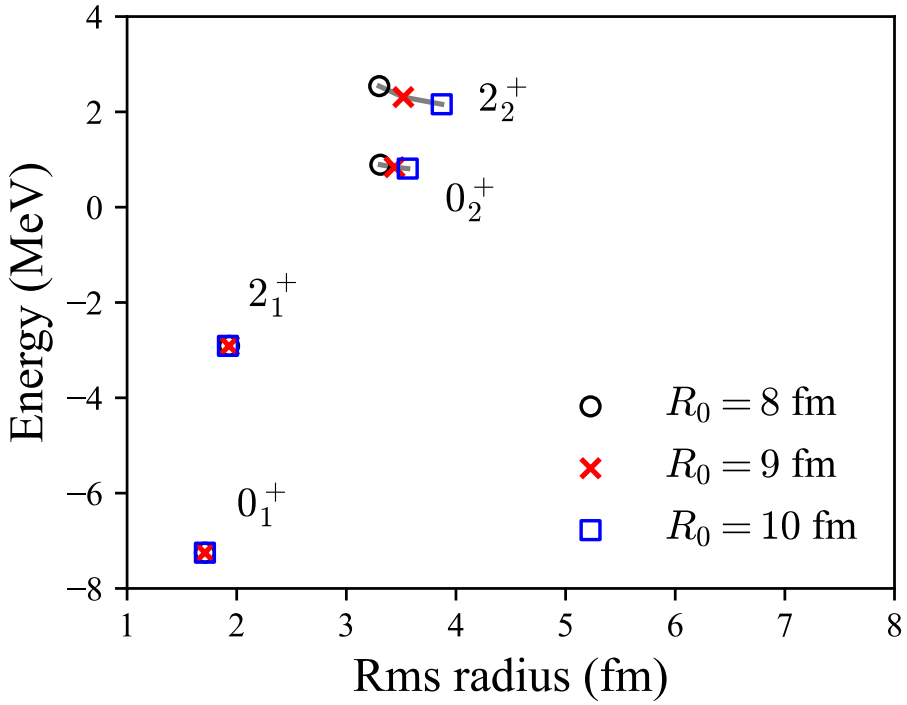

Figure 3.2: R_0 dependence in the CP. Energies and rms radii of the 0_1^+, 0_2^+, 2_1^+, and 2_2^+ states with $R_0 = 8, 9$ and 10 fm are plotted. The strength of the confining potential λ is set to be 100 MeV/fm^2. See text for details.

3.3 Results

3.3.1 One-body density and momentum distribution

Shell structure and the condensate structure of three-α can be seen by the one-body density and momentum distributions which are defined as

$$\rho(r) = \langle \Psi | \delta(|\boldsymbol{r}_1 - \boldsymbol{x}_3| - r) | \Psi \rangle \,, \tag{3.5}$$

$$\rho(k) = \langle \Psi | \delta(|\boldsymbol{k}_1 - \boldsymbol{k}_c m| - k) | \Psi \rangle \,, \tag{3.6}$$

where $\boldsymbol{k}_1$ is the conjugate momentum of $\boldsymbol{r}_1$ and $\boldsymbol{k}_c m$ is the momentum of the center-of-mass motion. Figure 3.3 shows the one-body density distribution and momentum distribution of the 0_1^+, 0_2^+, 2_1^+, and 2_2^+ states. For the momentum distributions of 0_1^+, as expected, there are three or two peaks with almost equal amplitude, which represent that three α particles are occupying three orbits not to violate Pauli principle in 0_1^+. This is nothing but the property of the shell structure. The momentum distribution of 2_1^+ has two peaks: one is located at the momentum near the middle peak of 0_1^+ with larger amplitude and the other is located at the largest momentum of peaks of 0_1^+ with almost same amplitude. This indicates that the 0_1^+ is rotationally excited to the 2_1^+ state by the center-of-mass. On the contrary, for both 0_2^+ and 2_2^+, the momentum distributions are concentrated at $k \sim 0.2$ fm^{-1}, which is the characteristic behavior of condensation state. Following the three or two peaks structure of the momentum distributions of 0_1^+ and 2_1^+, the one-body density distributions of those states also have three or two peak structure to be orthogonal to the Pauli forbidden states. In the same way, the

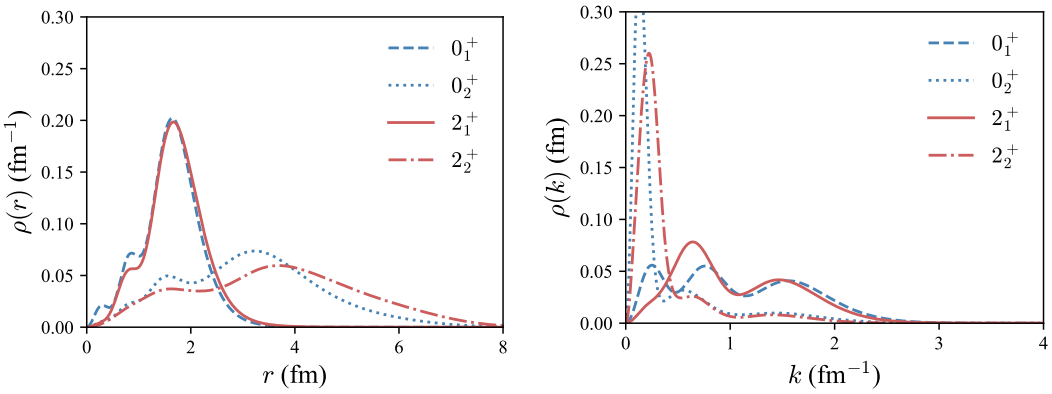

Figure 3.3: The one-body density distribution (left) and momentum distributions (right) of the 0_1^+, 0_2^+, 2_1^+, and 2_2^+ states.

one-body density distributions of 0_2^+ and 2_2^+ state widely spread with dilute density, which is consistent with the previous OCM study [57].

3.3.2 Three-α configurations: Two-body density

To discuss the geometric configurations of the three-α systems, it is intuitive to see the two-body density distributions with respect to the two relative coordinates, x_1 and x_2, defined by

$$\rho(r, R) = \langle \Psi | \delta(|\boldsymbol{x}_1| - r)\delta(|\boldsymbol{x}_2| - R) | \Psi \rangle \,, \tag{3.7}$$

Note that the distribution is normalized as $\int_0^\infty dr \int_0^\infty dR\, \rho(r, R) = 1$. Figure 3.4 plots the two-body density distributions of the $J^\pi = 0_1^+$, 0_2^+, 2_1^+, and 2_2^+ states. For a guide to the eyes, the specific r/R ratios are indicated by the dashed lines and their corresponding geometric shapes are depicted by inset figures. We remark that the two-body density distributions were already discussed for the $J^\pi = 0^+$ states in detail by using the shallow potential models [68, 79]. Here we present the results with the OCM. The preliminary results for the 0^+ states were already discussed in Ref. [56] but we repeat it to remind the characteristics of the two-body density distributions and to compare it with the 2^+ state.

The two-body density distributions of the 0_1^+ and 2_1^+ states have similar peak structures; the most dominant peak is located on the equilateral triangle configuration at $r \sim 3$ fm and some other peaks come from the nodal behavior of wave function due to the orthogonality to the forbidden states. We see different fine structures when a shallow potential model is employed. See Ref. [56] for detailed comparison.

In contrast to the compact ground state, the two-body density distribution of the 0_2^+ state is widely spreading. The most dominant peak of the 0_2^+ state distribution is located at the acute-angled triangle configuration, which comes from the $^8\mathrm{Be}(0^+) + \alpha$ structure [56]. For the 2_2^+ state, likely to the 0_2^+, the two-body density distribution spreads and the most dominant peak is located at the acute-angled triangle configuration. However, we find that the amplitude is significantly smaller than the 0_2^+ state and less small peaks in the internal regions. The difference of these peak structures between the 0_2^+ and 2_2^+ states implies different intrinsic structure, which will be discussed in the next subsection.

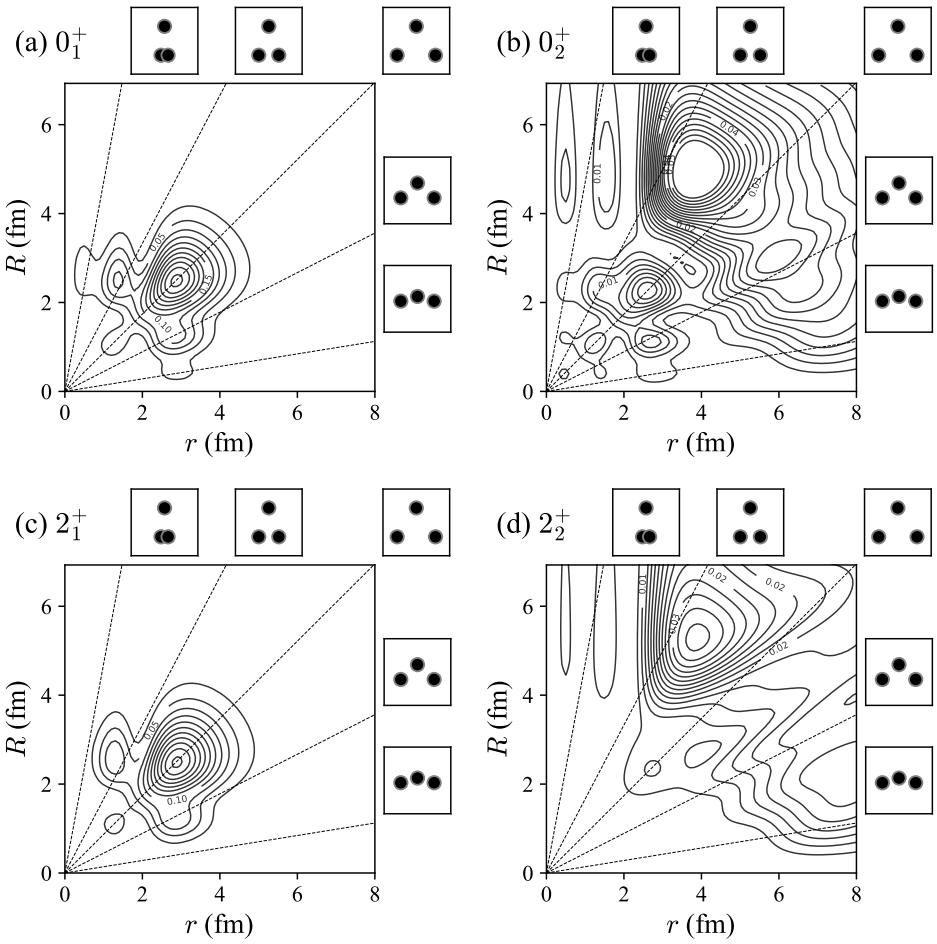

Figure 3.4: Two-body density distribution $\rho(r, R)$ of the (a) $J^\pi = 0_1^+$, (b) 0_2^+, (c) 2_1^+, and (d) 2_2^+ states. Contour intervals are 0.025 fm^{-2} for 0_1^+ and 2_1^+ and 0.0025 fm^{-2} for 0_2^+ and 2_2^+. Specific r/R ratios are indicated by dashed lines and their geometric configurations are illustrated in small panels, e.g., the diagonal dashed line indicates the equilateral triangle configurations.

3.3.3 Partial-wave and ^{8}Be components in the three-α wave functions

In this subsection, we discuss more detailed structure of these three-α wave functions. For this purpose it is convenient to calculate the partial-wave component and ^{8}Be spectroscopic factor, which are respectively defined by

$$P_{l_1 l_2} = \frac{3!}{2!1!} \left| \langle [Y_{l_1}(\hat{\boldsymbol{x}}_1) Y_{l_2}(\hat{\boldsymbol{x}}_2)]_{JM} | \, \Psi_{JM} \rangle \right|^2 , \tag{3.8}$$

$$S_{l_1 l_2} = \frac{3!}{2!1!} \left| \langle \phi_{l_1}(x_1) [Y_{l_1}(\hat{\boldsymbol{x}}_1) Y_{l_2}(\hat{\boldsymbol{x}}_2)]_{JM} | \, \Psi_{JM} \rangle \right|^2 , \tag{3.9}$$

where ϕ_l is the radial wave functions of ^{8}Be with the relative angular momentum $l = 0, 2$, or 4, which correspond to physical resonant states with $J^\pi = 0^+, 2^+$ or 4^+, respectively, obtained by solving the two-α system using the same two-α potential adopted in this chapter. The $P_{l_1 l_2}$ value is the probability of finding (l_1, l_2) component in the three-α wave function, while the $S_{l_1 l_2}$ value can be a measure of the the $^8\mathrm{Be} + \alpha$ clustering. Note that given l_1 and l_2, $S_{l_1 l_2}$ is a subspace of $P_{l_1 l_2}$, hence $S_{l_1 l_2} \leq P_{l_1 l_2}$ always holds.

Table **??** lists the $P_{l_1 l_2}$ and $S_{l_1 l_2}$ values for the 0^+ and 2^+ states. The 0_1^+ state has almost equal $P_{l_1 l_2}$ values for $l_1 = l_2 = 0, 2$, and 4, which can be explained by reminding that the state has the SU(3)-like character [57]. The higher partial-wave components is found to be $\approx 5\%$. The 0_1^+ wave function has about 50% of the $^8\mathrm{Be} + \alpha$ component. The 2_1^+ state is mainly composed of $(l_1, l_2) = (2, 2)$ and (4,4) components, P_{22} and P_{44}, reflecting SU(3) character as like the 0_1^+ state [57] and also contains about half of the $^8\mathrm{Be} + \alpha$ component. Consequently, the structure of the 2_1^+ state can be interpreted as a rigid rotational excited state of the 0_1^+ while keeping its geometric shape as was shown in Fig. 3.4.

On contrary, the $P_{l_1 l_2}$ values of 0_2^+ concentrate only on the $l_1 = l_2 = 0$ channel about 70%, which is consistent with the microscopic cluster model calculations [57,80]. This characteristic behavior is often interpreted as the bosonic condensate state of the three-α particles [26, 57]. This $(l_1, l_2) = (0, 0)$ channel mostly consists of the $^8\mathrm{Be}(0^+) + \alpha$ component shown in Table **??**, forming the acute-angled triangle shape in the two-body density distribution [56].

For the 2_2^+ state, dominant partial-wave components are the $(l_1, l_2) = (0, 2)$ and (2,0) channels. The $^8\mathrm{Be}(0^+) + \alpha$ component is dominant in the $(l_1, l_2) = (0, 2)$ channel, while few $^8\mathrm{Be}(2^+) + \alpha$ component is found in the $(l_1, l_2) = (2, 0)$ channel, which is in contrast to the 0_2^+ state mainly consisting of the $^8\mathrm{Be} + \alpha$ configuration. This strong suppression can naturally be understood by considering the fact that the excitation energy of $^8\mathrm{Be}(2^+)$ is rather high 3.26 MeV (Expt.: 3.12 MeV [81]), compared to the calculated energy spacing between 0_2^+ and 2_2^+, ≈ 1.4 MeV.

3.3.4 Spectroscopic amplitude

To discuss the role of the dominant channels in the geometric configurations in the 0_2^+ and 2_2^+ states, it is useful to evaluate the ^{8}Be spectroscopic amplitude (SA)

$$\theta_{l_1 l_2}(R) = \sqrt{\frac{3!}{2!1!}} \frac{1}{R^2} \times \left\langle \phi_{l_1}(x_1) \left[Y_{l_1}(\hat{\boldsymbol{x}}_1) Y_{l_2}(\hat{\boldsymbol{x}}_2) \right]_{JM} \delta(|\boldsymbol{x}_2| - R) \, \middle| \, \Psi_{JM} \right\rangle . \tag{3.10}$$

Note that $\int_0^\infty dR \, [R\theta_{l_1 l_2}(R)]^2 = S_{l_1 l_2}$. For practical calculations, see Appendix A of Ref. [82], where an explicit formula of the SA with the correlated Gaussian basis function was given.

Table 3.2: Partial-wave component and the ^{8}Be spectroscopic factor of the $J^\pi = 0^+$ and 2^+ states. Note that the rms distances of two-α system, ^{8}Be, is 5.32 fm for 0^+, 6.12 fm for 2^+, and 4.87 fm for 4^+. See text for details.

	0_1^+			2_1^+		
$(l_1 l_2)$	$P_{l_1 l_2}$	$S_{l_1 l_2}$	$D_{l_1 l_2}$	$P_{l_1 l_2}$	$S_{l_1 l_2}$	$D_{l_1 l_2}$
(00)	0.352	0.193	3.06	–	–	–
(02)	–	–	–	0.096	0.058	3.23
Subtotal ($l_1 = 0$)	0.352	0.193	3.06	0.096	0.058	3.23
(20)	–	–	–	0.095	0.054	3.19
(22)	0.351	0.175	2.67	0.483	0.268	2.92
(24)	–	–	–	0.006	0.003	2.49
Subtotal ($l_1 = 2$)	0.351	0.175	2.67	0.584	0.325	2.96
(42)	–	–	–	0.007	0.003	2.73
(44)	0.285	0.100	2.10	0.299	0.114	2.18
(46)	–	–	–	$\sim 10^{-4}$	$\sim 10^{-5}$	3.88
Subtotal ($l_1 = 4$)	0.285	0.100	2.10	0.306	0.117	2.20
Total	0.988	0.468	2.73	0.986	0.500	2.84

Figure 3.6 shows the SA with $(l_1, l_2) = (0, 0)$ for the 0_2^+ state and (0,2) for the 2_2^+ state, which respectively correspond to the dominant configurations for each state. The SA of the 2_2^+ state is smaller than that of the 0_2^+ state reflecting the magnitudes of the $S_{l_1 l_2}$ values. For the sake of comparison, we also plot the radial wave function of ^{8}Be(0^+), $\phi_0(r)$. The peak position of $r\phi_0(r)$ is located at 3.68 fm, while the SA has the largest peak at 4.97 fm for the 0_2^+ state and 6.20 fm for the 2_2^+ state. These are consistent with the fact that the highest peak of the two-body density distribution is located at $(r, R) = (3.9, 5.1)$ fm for the 0_2^+ state and $(r, R) = (3.9, 5.3)$ fm for the 2_2^+ state, exhibiting the acute-angled triangle configuration as shown in Fig. 3.4. SAs for other l_1 channels are also shown in Fig. 3.6, summed up for all l_2 and compared with the partial wave component defined as $\langle\Psi|\hat{P}(r)|\Psi\rangle$ where $\hat{P}(r) = \delta(|\boldsymbol{x}_2| - r)\,|l_1\rangle\,\langle l_1|$ and $|l_1\rangle$ is all channel having l_1.

We also evaluate the rms radii of the SA defined by $D_{l_1 l_2} = \sqrt{\int_0^\infty dR\, R^2 [R\theta_{l_1 l_2}(R)]^2 / S_{l_1 l_2}}$, listed in Table 3.2 and Table 3.3. The SA radii of the dominant channel of the 0_2^+ and 2_2^+ states are 5.84 fm with $(l_1, l_2) = (0, 0)$ and 7.38 fm with $(l_1, l_2) = (0, 2)$, respectively. Remanding that the rms distance of the ^{8}Be wave function is 5.32 fm, the $^8\mathrm{Be} + \alpha$ configuration induces an acute-angled triangle geometry.

3.4 Conclusion

How similar is the structure of the 2_2^+ state in the ^{12}C as compared to the Hoyle state? We have made comprehensive investigations of the structure of ^{12}C with a special emphasis on the geometric configurations of α particles. The 0^+ and 2^+ states of ^{12}C are described by a three-α cluster model with the orthogonality constraint. Precise three-α wave functions are obtained by using the correlated Gaussian expansion with the stochastic variational method. We introduce a confining potential to obtain a physical state, allowing us to visualize the three-α configuration by using square integrable basis functions.

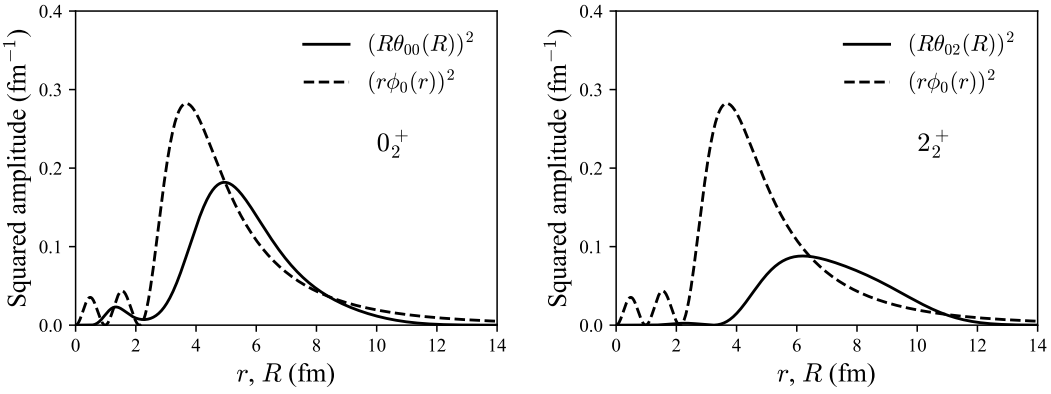

Figure 3.5: Square of ^{8}Be spectroscopic amplitudes, $\theta_{l_1 l_2}(R)$ with (a) $(l_1, l_2) = (0, 0)$ and (b) $(l_1, l_2) = (0, 2)$ for the 0_2^+ and 2_2^+ states. The radial wave function of the ^{8}Be(0^+) state $\phi_0(r)$ is also compared.

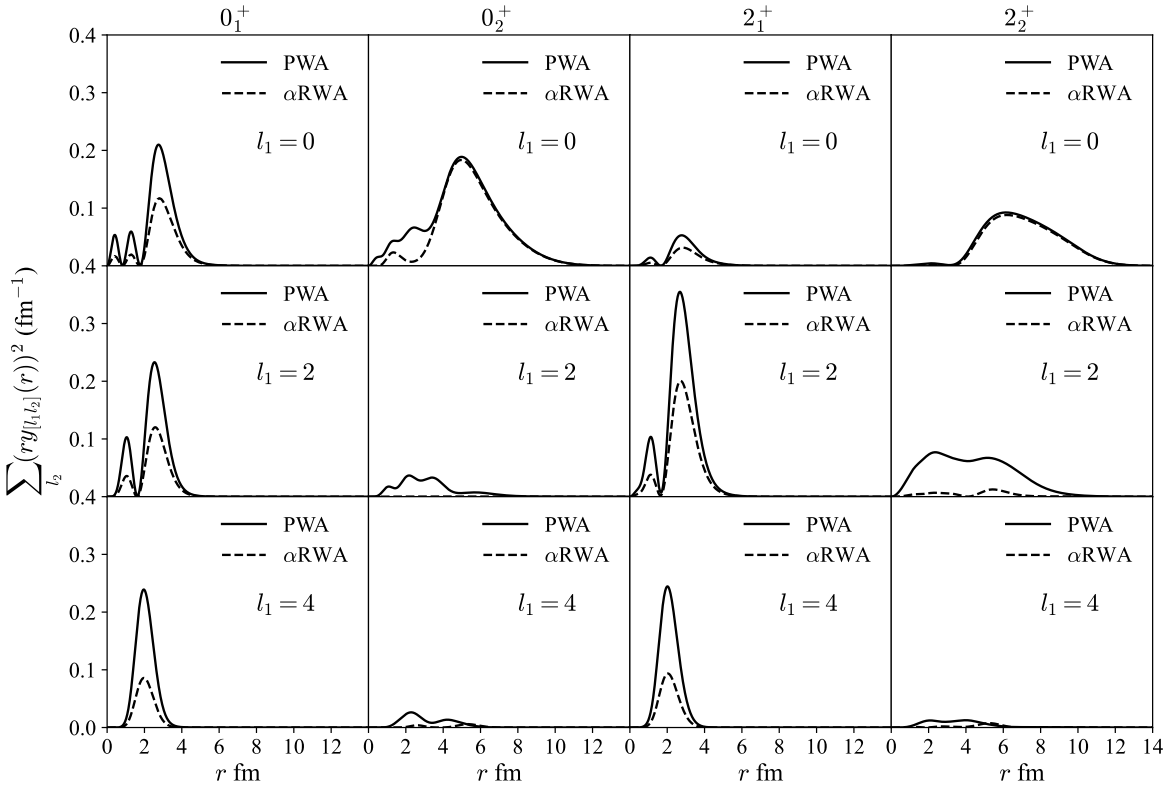

Figure 3.6: The partial wave amplitude and the total ^{8}Be spectroscopic amplitude of $0_1^+, 0_2^+, 2_1^+, 2_2^+$ states for l_1 =0, 2, and 4.

Table 3.3: Same as the Tab. 3.2 but for 0_2^+ and 2_2^+.

	0_2^+			2_2^+		
$(l_1 l_2)$	$P_{l_1 l_2}$	$S_{l_1 l_2}$	$D_{l_1 l_2}$	$P_{l_1 l_2}$	$S_{l_1 l_2}$	$D_{l_1 l_2}$
(00)	0.786	0.668	5.84	–	–	–
(02)	–	–	–	0.451	0.419	7.38
Subtotal ($l_1 = 0$)	0.786	0.668	5.84	0.451	0.419	7.38
(20)	–	–	–	0.374	0.021	4.60
(22)	0.112	0.027	4.00	0.044	0.011	5.45
(24)	–	–	–	0.020	0.007	5.17
Subtotal ($l_1 = 2$)	0.112	0.027	4.00	0.438	0.039	4.96
(42)	–	–	–	0.029	0.007	5.10
(44)	0.060	0.013	4.75	0.017	0.008	5.15
(46)	–	–	–	0.006	0.004	5.49
Subtotal ($l_1 = 4$)	0.060	0.013	4.75	0.052	0.019	5.20
Total	0.958	0.708	5.76	0.941	0.477	7.13

In comparison of the two-body density distributions of the 0_2^+ and 2_2^+ state, the main three-α configurations are found to be the same; the acute-angled triangle shape coming from the $^8\mathrm{Be}(0^+) + \alpha$ component. However, the magnitude is significantly small for the 2_2^+ state compared to the 0_2^+ state. We find that the 2_2^+ state can be mainly excited by the relative coordinate between ^{8}Be and α consistently with the interpretation given in Refs [19, 20, 70]. The ^{8}Be cluster in the 0_2^+ state is hardly excited because the excitation energy of the $^8\mathrm{Be}(2^+)$ is higher than the energy difference of 2_2^+ state from the Hoyle state. Therefore, we conclude that the 2_2^+ state is not an ideal rigid Hoyle band but could be interpreted as a partially rotational excited state of 0_2^+. It is interesting to study the 4_2^+ state, which is observed recently [39] and considered also as a candidate of the Hoyle band member.

Chapter 4

Three-alpha system in dilute neutron matter

We investigate two and three α particles in cold neutron matter by focusing on an analogy between such α systems and Fermi polarons realized in ultracold atoms. We describe in-medium excitation properties of an α particle and neutron-mediated two- and three-α interactions using theoretical approaches developed for studies of cold atomic systems. We precisely solve the few-body Schrödinger equation of α particles within OCM with evaluated in-medium properties of α particles. We point out that the two-α ground state and three-α first excited state, which are ^{8}Be and the Hoyle state, respectively, known as main components in the triple-α reaction, can become bound states in such a many-neutron background although these states are unstable in vacuum. Our results suggest a significance of these in-medium cluster states not only in astrophysical environments such as core-collapsed supernova explosions and neutron star mergers but also in neutron-rich nuclei.

4.1 Background of the Hoyle state in medium

In light $N = Z$ nuclei, the threshold energy for α particle disintegration becomes low and even comparable to the one-α separation energy, which helps the α cluster structure to emerge in the spectrum of such light nuclei as predicted by the Ikeda diagram [3].

As introduced in the chapter 1.2, one of the most famous examples of the α cluster structure is the first excited $J^\pi = 0^+$ state of ^{12}C, which was originally predicted by Fred Hoyle [7], This state is known to have a well-developed three-α cluster structure [69, 70]. The existence of such cluster states plays a role in enhancing the reaction rate at extremely low energies near the Gamow window. The ^{12}C element forms dominantly through a sequential reaction in which a resonant two-α system, the ground state of ^{8}Be, absorbs another α particle via radiative capture process [83]. The accurate description of such α induced reactions can impact astrophysically important explosive phenomena [63], such as core collapse supernovae and neutron star mergers, which have recently started to be measured through gravitational waves [62].

α clusters is also important in many-nucleon systems such as medium-heavy nuclei and nuclear matter. The role of α particles in supernova explosions has attracted attention [61], which is related with its equation of state. Very recently, an interesting indication that α clusters emerge in a surface region of medium-heavy mass nuclei have been obtained by a

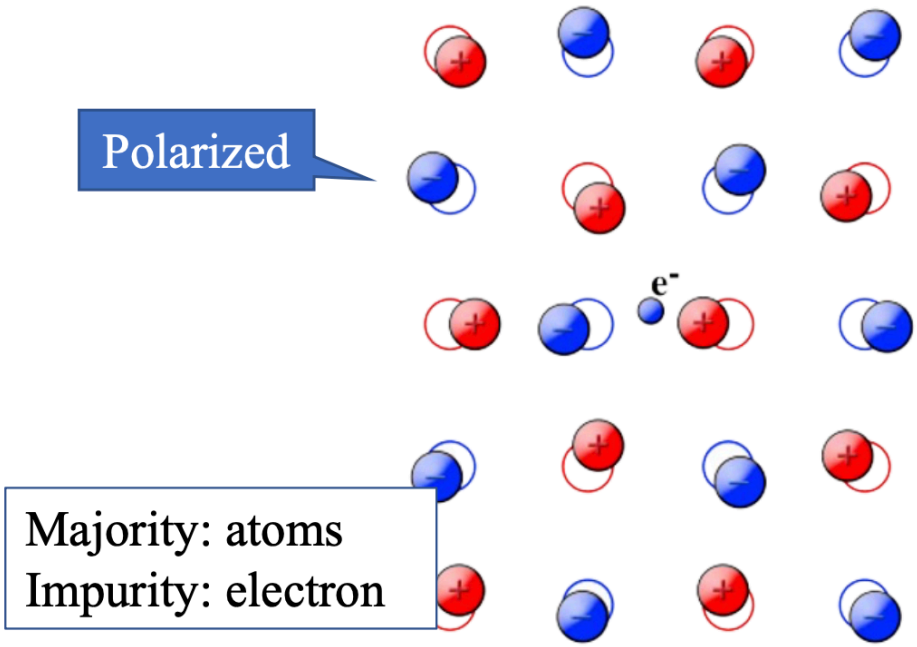

Figure 4.1: Schematic picture of the polaron in atomic physics. The figure of the atom crystals and electron is taken from the wikipedia (https://en.wikipedia.org/wiki/Polaron)

systematic measurement via the α knockout reactions [5]. These backgrounds motivate us to study the formation and structure of an α particle in dilute neutron-rich matter. In Ref. [84], the static properties of an α particle in cold dilute neutron matter has been discussed. The effective mass of the in-medium α particle is enhanced by the interaction with the neutron matter, implying the possibility of binding the ground state resonance of ^{8}Be and the Hoyle state in such an extreme environment. If these ingredients become stable, they should be incorporated explicitly as ingredients of simulations of astrophysical nuclear processes [85], which may affect the local abundance of the chemical elements.

In the theoretical side, it is challenging to evaluate how impurity particles behave and are affected in many-body backgrounds like a Fermi sea due to infinitely large degrees of freedom. Nevertheless, this problem has been approached in ultracold atoms theoretically and experimentally in terms of Fermi polarons [86–88]; an impurity atom is dressed by excitations of majority Fermi atoms via interspecies interactions. For example in Fig. 4.1, an impurity electron is moving in the majority atom crystals. The moving electron is dressed by the phonon cloud by the excitations via interaction with the atoms, which is treated as a quasiparticle, polaron. This picture can be extended to impurity α clusters in the majority cold dilute neutron matter as shown in Fig. 4.2. Quasiparticle properties of a single polaron such as the effective mass have precisely been measured in experiments [89–97] and successfully described by various theoretical frameworks such as a variational method [98] and a T-matrix approximation [99]. Moreover, fermion-mediated interactions between polarons have also been observed experimentally [100, 101].

In this work, we investigate the structure of two- and three-α systems in dilute neutron matter of density lower than about 1/100 of the saturation density $\sim 0.01\rho_0$ at zero temperature. We discuss their medium-induced stabilization by regarding each α particle as a moving

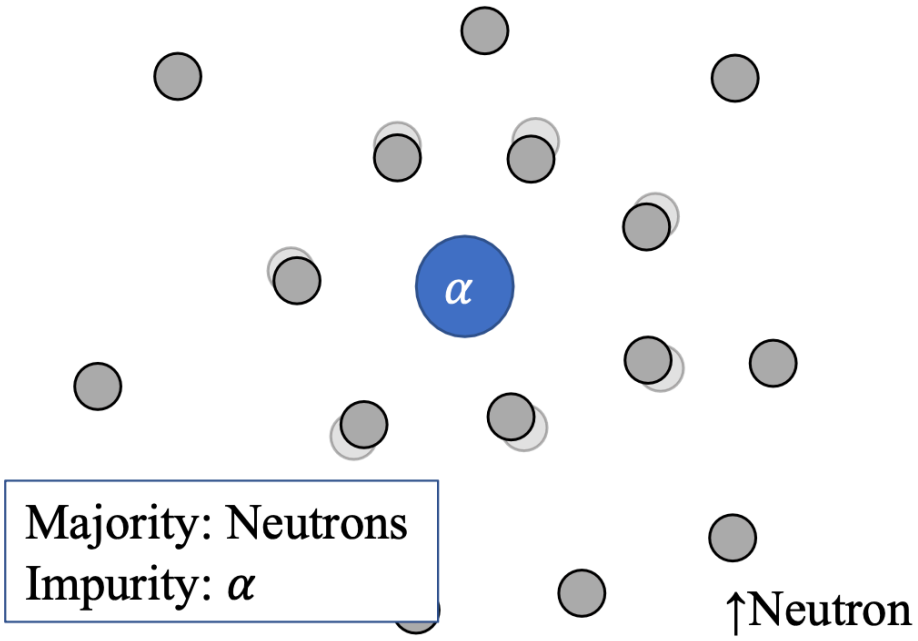

Figure 4.2: Schematic picture of the polaron of α cluster in the cold dilute neutron matter.

impurity immersed in the neutron medium. Analogy with Fermi polarons in ultracold atoms allows us to utilize the results obtained for quasiparticle properties of a single α particle in neutron matter [84] by using Chevy's variational ansatz which gives a quantitative description of Fermi atomic polarons. To incorporate in-medium effect to two- and three-α particles immersed in neutron matter, moreover, we derive medium-induced two- and three-body interactions among polarons using a diagrammatic approach. These quasiparticle properties modify the few-α Hamiltonian in vacuum to the one in the neutron medium. Once the effective Hamiltonian is set, the structure of the in-medium two- and three-α systems can be accurately obtained from the solution of the corresponding few-body Schrödinger equation by utilizing the SVM explained in chapter 2. This study offers the first quantitative evaluation of the energy and the pair density distribution of two and three-α systems in cold neutron matter.

This chapter is organized as follows. The next section describes models of the in-medium multi-α systems. Section 4.2.1 is devoted to the derivation of induced two- and three-α interactions in a neutron Fermi sea. Section 4.2.2 gives the effective Hamiltonian for the multi-α systems in the cold neutron matter. The two cluster models employed in this study are briefly described in Sec. 4.2.3. Section 4.3 presents our results. The possibility of the medium-induced stabilization of the two- and three-α systems is discussed. The conclusion and future prospects are given in Sec. 4.4.

4.2 Models of in-medium two- and three-α systems

Let us proceed to construct models for the systems of two and three α particles of bare mass M in a dilute gas of neutrons of bare mass m at zero temperature. Since we are interested in α particles in astrophysical environments where the temperature is higher than the neutron

superfluid critical temperature [63], we can safely assume that the neutron gas is in a normal state. We also ignore the neutron-neutron interaction for simplicity. Although we employ the zero-temperature results for the induced interactions among α particles and the α effective mass as will be discussed below, such zero-temperature treatment can be justified when the temperature is below both the neutron Fermi temperature $T_F = \frac{\hbar^2 k_F^2}{2m}$ and the cutoff energy scale $\frac{\hbar^2}{m_r r_0^2} \simeq 25$ MeV of the neutron-α interaction with the effective range $r_0 = 1.43$ fm [84]. We finally remark that at sufficiently high neutron densities corresponding to $k_F \gtrsim 0.3$ fm^{-1}, a p-wave resonance (^{5}He) could be stabilized by the Pauli blocking effect and emerge as a nuclear ingredient [84, 85]. This possibility is another issue to be tackled with, but is beyond the scope of this work.

4.2.1 Derivation of induced two- and three-body interactions in cold neutron matter

We start with diagrammatic derivation of the medium-induced two- and three-body interactions among α particles in a neutron Fermi sea. As depicted diagrammatically in Fig. 4.3(a), the induced two-body interaction between two α particles can be obtained up to leading order in a as [102]

$$V_{\rm eff}^{(2)}(\boldsymbol{q}, i\nu_\ell) = -\left(\frac{2\pi\hbar^2 a}{m_r}\right)^2 \frac{k_B T}{\hbar^2} \sum_{\sigma=\uparrow,\downarrow} \sum_{\boldsymbol{p},\omega_n} G_\sigma(\boldsymbol{p}+\boldsymbol{q}, i\omega_n + i\nu_\ell) G_\sigma(\boldsymbol{p}, i\omega_n),$$

where k_B is the Boltzmann constant, $(\boldsymbol{q}, i\nu_\ell) = (\boldsymbol{k}-\boldsymbol{k}', i\nu_s - i\nu_{s'})$ is the transferred four-momentum, $\nu_\ell = 2\ell\pi k_B T/\hbar$ is the bosonic Matsubara frequency [103], $G_\sigma(\boldsymbol{p}, i\omega_n) = (i\omega_n - \xi_{\boldsymbol{p}})^{-1}$ is the thermal Green's function of a neutron with energy $\xi_{\boldsymbol{p}} = \frac{p^2}{2m} - \varepsilon_F$ relative to the neutron Fermi energy ε_F, and $m_r = (m^{-1} + M^{-1})^{-1}$ is the reduced mass. $a = 2.64$ fm is the s-wave neutron-α scattering length [84]. Taking the summation of the fermionic Matsubara frequency $\omega_n = (2n+1)\pi k_B T/\hbar$ [103], we obtain the induced two-body interaction as

$$V_{\rm eff}^{(2)}(\boldsymbol{q}, i\nu_\ell) = 2\left(\frac{2\pi\hbar^2 a}{m_r}\right)^2 \sum_{\boldsymbol{p}} \frac{f(\xi_{\boldsymbol{p}}) - f(\xi_{\boldsymbol{p}+\boldsymbol{q}})}{i\hbar\nu_\ell + \xi_{\boldsymbol{p}} - \xi_{\boldsymbol{p}+\boldsymbol{q}}}. \tag{4.1}$$

In the low-energy limit $\nu_\ell = 0$ at $T = 0$, Eq. (4.1) reduces to

$$V_{\rm eff}^{(2)}(\boldsymbol{q}, 0) = -\frac{m k_F}{2\pi^2\hbar^2}\left(\frac{2\pi\hbar^2 a}{m_r}\right)^2 \left[1 + \frac{k_F}{q}\left(1 - \frac{q^2}{4k_F^2}\right)\ln\left|\frac{q+2k_F}{q-2k_F}\right|\right].$$

Note that in the long wavelength limit ($\boldsymbol{q} \to 0$), Eq. (4.2) can be expressed by the compressibility $\kappa = \frac{1}{\rho^2}\left(\frac{\partial\rho}{\partial\mu}\right)$ of neutron matter as $V_{\rm eff}^{(2)}(\boldsymbol{q}\to\boldsymbol{0}, 0) = -\left(\frac{2\pi\hbar^2 a}{m_r}\right)^2 \rho^2\kappa$. By taking the inverse Fourier transformation of Eq. (4.2), we obtain the well-known Ruderman-Kittel-Kasuya-Yosida (RKKY) form of the induced two-body interaction in the coordinate space as [104–108]

$$V_{\rm eff}^{(2)}(\boldsymbol{r}_1, \boldsymbol{r}_2) = \frac{m}{8\pi^3\hbar^2}\left(\frac{2\pi\hbar^2 a}{m_r}\right)^2 \frac{(2k_F r)\cos(2k_F r) - \sin(2k_F r)}{r^4},$$

where $r = |\boldsymbol{r}_1 - \boldsymbol{r}_2|$.

In addition to this, as diagrammatically drawn in Fig. 4.3(b), the induced three-body interaction up to leading order in a is given by [109]

$$V_{\rm eff}^{(3)}(\boldsymbol{k},\boldsymbol{q},i\nu_\ell,i\nu_u) = 2\left(\frac{2\pi\hbar^2 a}{m_r}\right)^3 \times \frac{k_BT}{\hbar^3}\sum_{\sigma=\uparrow,\downarrow}\sum_{\boldsymbol{p},\omega_n} G_\sigma(\boldsymbol{p},i\omega_n)G_\sigma(\boldsymbol{p}+\boldsymbol{k}+\boldsymbol{q}/2,i\omega_n+i\nu_\ell) \times G_\sigma(\boldsymbol{p}+\boldsymbol{k}-\boldsymbol{q}/2,i\omega_n+i\nu_\ell-i\nu_u), \tag{4.2}$$

where $\boldsymbol{k}=\boldsymbol{k}_1-\boldsymbol{k}_2$, $\boldsymbol{q}=\boldsymbol{q}_1-\boldsymbol{q}_2$ $i\nu_\ell = i\nu_{s_1}-i\nu_{s_2}$, and $i\nu_u = i\nu_{j_1}-i\nu_{j_2}$ are the transferred four-momenta. In the low-energy limit ($i\nu_\ell = i\nu_u = 0$), the induced three-body interaction in the coordinate space can be obtained as

$$V_{\rm eff}^{(3)}(\boldsymbol{r}_1,\boldsymbol{r}_2,\boldsymbol{r}_3) = \sum_{\boldsymbol{k},\boldsymbol{q}} V_{\rm eff}^{(3)}(\boldsymbol{k},\boldsymbol{q},0,0)e^{-i\boldsymbol{k}\cdot\boldsymbol{x}_1+i\boldsymbol{q}\cdot\boldsymbol{x}_2}, \tag{4.3}$$

where $\boldsymbol{x}_1=\boldsymbol{r}_1-\boldsymbol{r}_2$ and $\boldsymbol{x}_2=\boldsymbol{r}_3-(\boldsymbol{r}_1+\boldsymbol{r}_2)/2$. For simplicity, we employ the contact-type three-body interaction whose coupling constant is given by

$$\begin{aligned} V_{\rm eff}^{(3)}(\boldsymbol{0},\boldsymbol{0},0,0) &= 2\left(\frac{2\pi\hbar^2 a}{m_r}\right)^3 \frac{k_BT}{\hbar^3}\sum_\sigma\sum_{\boldsymbol{p},i\omega_n}[G_\sigma(\boldsymbol{p},i\omega_n)]^3 \\ &= \frac{m^2}{\pi^2\hbar^4 k_F}\left(\frac{2\pi\hbar^2 a}{m_r}\right)^3. \end{aligned} \tag{4.4}$$

Thus, we obtain

$$V_{\rm eff}^{(3)}(\boldsymbol{r}_1,\boldsymbol{r}_2,\boldsymbol{r}_3) = \frac{m^2}{\pi^2\hbar^4 k_F}\left(\frac{2\pi\hbar^2 a}{m_r}\right)^3 \delta(\boldsymbol{x}_1)\delta(\boldsymbol{x}_2). \tag{4.5}$$

Note that to adopt the contact interaction (4.5) is equivalent to the local density approximation.

4.2.2 Hamiltonian for two- and three-α particles in cold neutron matter

A single α particle immersed in cold neutron matter has its mass M changed into the effective mass M^* by the interaction with neutrons in the medium. This particle, dressed with neutron excitations, can be regarded as a polaron. As a natural extension of the previous study on this polaron [84], we consider two- and three-α systems immersed in cold neutron matter. As we shall see, the mass enhancement through M^* acts to increase binding of these systems. The explicit form of the Hamiltonian of the three-α system in cold neutron matter is

$$H = \sum_{i=1}^3 \frac{\boldsymbol{p}_i^2}{2M^*} - T_{\rm cm} + \sum_{i<j=1}^3 \left[U_{ij}^{(2)} + V_{{\rm eff};ij}^{(2)}\right] + U^{(3)} + V_{\rm eff}^{(3)},$$

where the center-of-mass kinetic energy term $T_{\rm cm}$ is subtracted, $U^{(x)}$ ($x=2,3$) denotes the $x\alpha$ potential in vacuum including the Coulomb term, and $V_{\rm eff}^{(x)}$ is the induced $x\alpha$ interaction in the neutron medium with the Fermi momentum k_F. Note that M^* and $V_{\rm eff}^{(x)}$ depend on k_F. The k_F dependence of M^*/M is taken from Ref. [84]. We take the neutron mass as $\hbar^2/m=$ 41.47 MeV fm^2 and $M=4m$ to keep the consistency of the parameters given in Ref. [84].

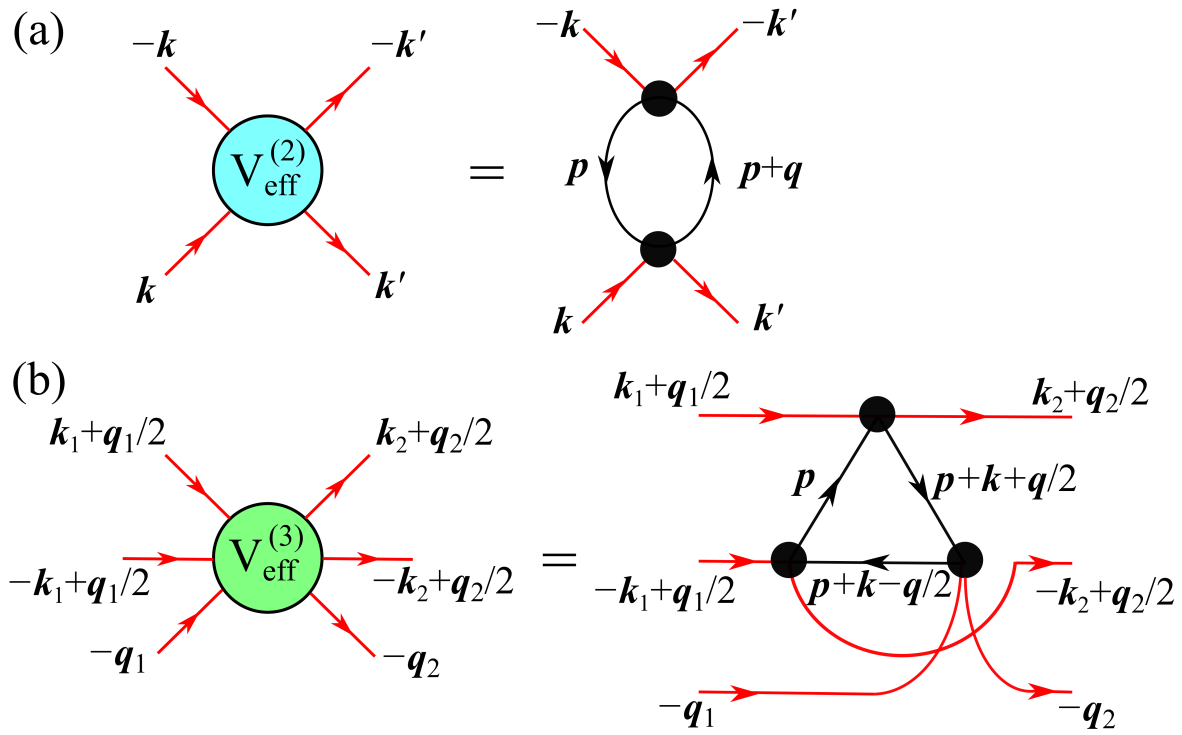

Figure 4.3: Feynman diagrams that represent the induced (a) two-body interaction $V_{\rm eff}^{(2)}(\boldsymbol{q}, i\nu_\ell)$ and (b) three-body interaction $V_{\rm eff}^{(3)}(\boldsymbol{k}, \boldsymbol{q}, i\nu_\ell, i\nu_u)$ among α particles immersed in neutron matter. For $V_{\rm eff}^{(2)}(\boldsymbol{q}, i\nu_\ell)$, the incoming (outgoing) momenta of α particles are given by $\boldsymbol{k}$ and $-\boldsymbol{k}$ ($\boldsymbol{k}'$ and $-\boldsymbol{k}'$). For $V_{\rm eff}^{(3)}(\boldsymbol{k}, \boldsymbol{q}, i\nu_\ell, i\nu_u)$, the incoming (outgoing) momenta of α particles are given by $\boldsymbol{k}_1 + \boldsymbol{q}_1/2$, $-\boldsymbol{k}_1 + \boldsymbol{q}_1/2$, and $-\boldsymbol{q}_1$ ($\boldsymbol{k}_2 + \boldsymbol{q}_2/2$, $-\boldsymbol{k}_2 + \boldsymbol{q}_2/2$, and $-\boldsymbol{q}_2$). The internal solid lines denote the thermal Green's function of a neutron. This figure is taken from the Ref. [110].

Here we incorporate $V_{\rm eff}^{(2)}$ and $V_{\rm eff}^{(3)}$ derived in the previous subsection into the Hamiltonian. The original RKKY potential (4.2) behaves as $\sim r^{-1}$ at small r and hence has a singularity at the origin. This is regularized by folding the harmonic oscillator type form factor of the α particle associated with the nuclear force, $\left(\frac{8\nu}{3\pi}\right)^{\frac{3}{2}} e^{-\frac{8}{3}\nu u^2}$, which leads to

$$V_{\rm eff}^{(2)}(r) = V_{\rm RKKY}(r) \mathrm{erf}\left(\frac{4}{3}\sqrt{\nu} r\right), \tag{4.6}$$

where ν is also taken as 0.2675 fm^{-2} in a way that is consistent with the width parameter of the α particle [73]. Note that this range is shorter than the α-n scattering length a and $1/k_F$ considered in this work. It is reasonable to take the range of the induced three-body force as the same as the one for the induced two-α interaction, which leads to

$$V_{\rm eff}^{(3)}(R) = \frac{m^2}{\pi^2 \hbar^4 k_F} \left(\frac{2\pi\hbar^2 a}{m_r}\right)^3 N_\nu e^{-\frac{16}{9}\nu R^2} \tag{4.7}$$

with the normalization constant of the form factor $N_\nu = \left(\frac{16\nu}{3\pi}\right)^3$. Note that $R^2 = (\boldsymbol{r}_1 - \boldsymbol{r}_2)^2 + (\boldsymbol{r}_2 - \boldsymbol{r}_3)^2 + (\boldsymbol{r}_3 - \boldsymbol{r}_1)^2 = \frac{3}{2}x_1^2 + 2x_2^2$, which is symmetric in any particle exchange.

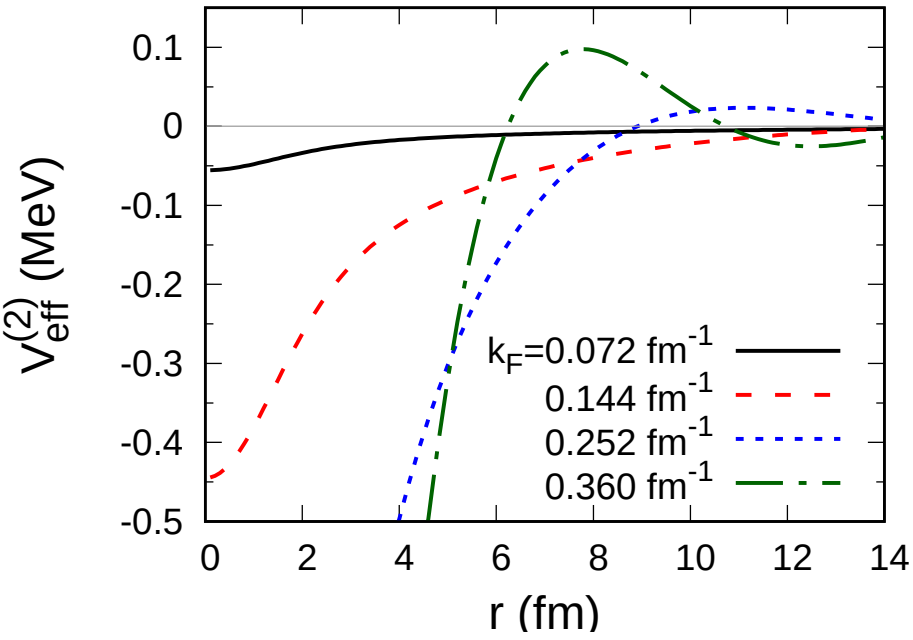

Figure 4.4: Induced two-body interaction $V^{(2)}_{\rm eff}(r)$ as a function of the α-α distance r for various values of the Fermi momenta k_F of cold neutron matter. The thin horizontal line indicates zero. This figure is taken from the Ref. [110].

Since a is positive, the induced three-α potential is always repulsive; its strength is inversely proportional to k_F.

Figure 4.4 plots the k_F dependence of the induced two-α potential, Eq. (4.6). At short distances, this two-α interaction is attractive, leading to more stability of multi-α systems. The range of such attraction increases with k_F, while, for sufficiently large k_F, some oscillatory behavior appears, a feature reflecting the Friedel oscillation associated with the presence of the neutron Fermi surface. The induced three-α interaction, on the other hand, is repulsive and weakens as k_F increases. The optimal stability of the three-α system can thus be realized at a certain k_F that is determined in balance with the purely repulsive induced three-α potential.

The difference of the effective mass from the bare mass, together with the induced interactions, can crucially affect the relative motion between α particles. In this work, we consider each α particle to be a structureless particle but treats the Pauli principle in the interaction between α particles in two different ways. Both potential models well reproduce the empirical α-α scattering phase shift. Although it is difficult to obtain empirical information on the closest motion, they are known to give different results for the internal region of the relative wave function. See, e.g., [56, 111, 112] for some examples in light cluster systems. We utilize such two potential models to evaluate the uncertainty that comes from model choice.

4.2.3 Multi-α cluster models

We employed two standard types of α cluster model OCM and the shallow potential model to see the model dependence. As the shallow potential model, we employ the Ali-Bodmer (AB) potential [**?**] (Set a$'$ [113]), which reproduces the α-α scattering phase shift and produces the S-wave ^{8}Be (0^+_1) resonance position with 0.093 MeV, a value close to the empirical one 0.092

MeV [81]. Note that we get 0.086 MeV in the present calculation because of the use of the different mass parameter of an α particle ($M = 4m$). The AB potential is l-dependent and its explicit form is

$$U_{\rm AB}(r) = \left(125\hat{P}_{l=0} + 20\hat{P}_{l=2}\right) \exp\left(-\frac{r^2}{1.53^2}\right) - 30.18 \exp\left(-\frac{r^2}{2.85^2}\right),$$

where the energy and length are given in units of MeV and fm, and $\hat{P}_l$ is the projection operator onto the relative angular momentum l. This potential is so shallow that no bound state appears. The Pauli principle in the interaction between α particles is simulated by the first repulsive term of the potential. It is known that the empirical energies of states close to the threshold energy of the three-α system are not well reproduced by the two-body interaction alone [114]. Then, one often introduces a phenomenological three-α potential as $U^{(3)}$, which only has a single Gaussian attractive term [115]. Because of such simplicity, a similar sort of potential model has often been used to describe astrophysically important reactions [45, 46, 115–118]. This three-α interaction, together with the two-α one, leads to the Hoyle state energy of 0.38 MeV with respect to the three-α threshold, which perfectly agrees with the empirical Hoyle state energy [74].

As the OCM, in the present study, we employ a folding-type two-α potential that was based on the effective nucleon-nucleon interaction [120] and readjusted in Ref. [73]. This potential is expressed in a single Gaussian form that only includes attractive term. The calculated energy of ^{8}Be is 0.095 MeV, reproducing the empirical energy. The explicit form of the potential is a simple Gaussian form:

$$U_{\rm OCM}(r) = -106.1 \exp\left(-\frac{r^2}{2.23^2}\right). \tag{4.8}$$

This potential is apparently much deeper than the AB potential of Eq. (**??**), and produces the three redundant forbidden states, which should be removed from all the pairwise wave functions in the three-α systems. The present Hamiltonian makes the ground- and Hoyle states overbound only with the two-α interaction, and hence a repulsive phenomenological three-α potential is often introduced to adjust these energies to the empirical values. Some applications with this potential set are given in Refs. [**?**, 121, 122]. Because the calculated Hoyle state energy amounts to no less than 0.78 MeV, here we newly parametrize a three-α potential better able to reproduce the empirical Hoyle state energy 0.38 MeV [74] for a fair comparison with the AB result. The explicit form of the potential in MeV is

$$U^{(3)}(R) = 77.0 \exp(-0.12R^2) - 10.0 \exp(-0.03R^2). \tag{4.9}$$

The calculated Hoyle state energy is 0.34 MeV, which is close to the empirical energy of the Hoyle state. Within these two models, we numerically obtained the precise wave functions by using the SVM and the the fully symmetrized correlated Gaussian basis as explained in chapter 2.

4.3 Results and discussions

In neutron matter, the effective mass M^* of an α particle as well as the induced two- and three-α interactions, changes with k_F [84]. Here we discuss the influence of these medium effects on the binding energy of the two- and three-α systems. More specifically, we analyze

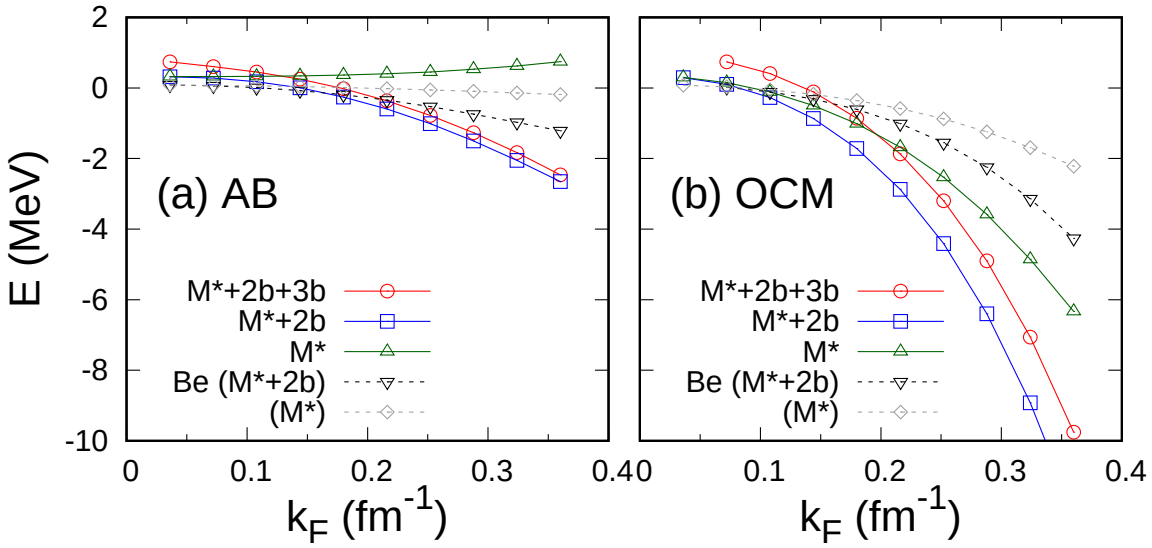

Figure 4.5: Energies of the three-α system in neutron matter calculated as a function of the neutron Fermi momentum with different potential models, (a) AB and (b) OCM. The calculations including the effective mass alone as medium effects are denoted by M^*, while those additionally including the induced two-body force and also the induced three-body force are denoted by M^* + 2b and M^* + 2b+3b, respectively. The results for the two-α system (^{8}Be) are also plotted for comparison. The lines are guide for the eye. This figure is taken from the Ref. [110]

the ground state of the two-α system, i.e., ^{8}Be, and the first excited state of the three-α system, i.e., the Hoyle state of ^{12}C, both of which exhibit a resonance in vacuum. We shall show that both the ^{8}Be and Hoyle states become bound in the neutron medium of sufficiently large k_F.

Figure 4.5 shows the energies of the three-α systems relative to the three-α threshold, calculated for AB and OCM as a function of the Fermi momentum of the neutron medium k_F. To see the contributions of the induced interactions, we compare the energies including the two-body and/or three-body induced interactions with the one in the absence of the induced interactions. In general, each energy thus calculated gains as k_F increases except for the Hoyle state energies only with M^* for AB. Note that M^* increases with k_F [84], leading to further localization near the potential minima. In fact, the results only with M^* contribution clearly reflect the properties that the OCM potential only have an attractive component while the AB potential has repulsive and attractive components at short and intermediate distances, respectively.

For the same reason, α particles of larger M^* come closer to each other once the induced two-α interaction, which is attractive at short distances as shown in Fig. 4.4, is taken into account. Then, the induced two-body interaction always plays a role in gaining the binding energy, which can be seen in the results allowing for the induced two-body interaction (M^* + 2b). On the other hand, the induced three-α interaction is always repulsive, which leads to increase in the energy denoted by M^*+2b+3b as compared with the one denoted by M^*+2b. The result of OCM (M^* + 2b + 3b) with $k_F = 0.036$ fm^{-1} is not shown because no physically stable state is obtained due to too strong repulsion of the induced three-α interaction.

While all the above-mentioned tendencies apply to the two cluster models, quantitative details look very different. For AB, virtually no contribution from the induced three-body interaction is found because there is only a negligible wave function amplitude in the internal region due to the repulsive component of the AB potential, which will be shown in the next paragraph. The ground state of ^{8}Be become bound at $k_F \gtrsim 0.11$ fm^{-1} for AB and $\gtrsim 0.08$ fm^{-1} for OCM. The Hoyle state becomes bound, i.e., the energy is located below the ^{8}Be energy, at $k_F \gtrsim 0.22$ fm^{-1} for AB and $\gtrsim 0.16$ fm^{-1} for OCM. In the OCM case, the condition for binding of the Hoyle state is determined by a subtle competition between the attractive and repulsive contributions from the induced two- and three-body interactions, respectively. Incidentally, one can safely ignore the excited states and dissociation of an α particle because the excitation energy to the first excited state in vacuum is far larger than the neutron Fermi energy at neutron densities of interest here. Also, we ignore possible increase in the kinetic energy of the two- and three-α systems due to the Pauli blocking effect, which, in the case of dissolution of α clusters, would become significant when the density of the nuclear medium exceeds 0.03 fm^{-3} [85], again far higher than the medium density considered here.

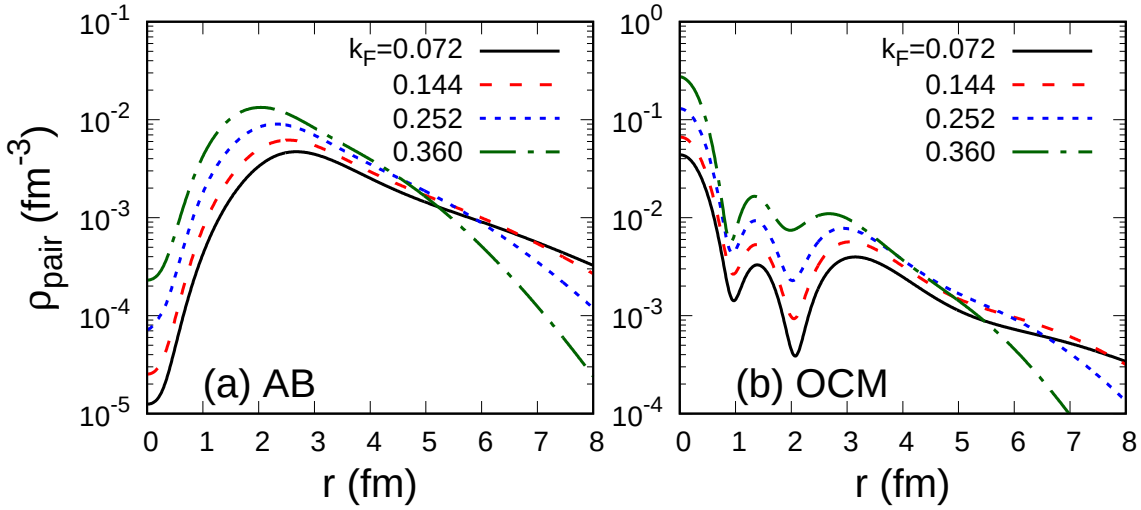

Figure 4.6: Pair density distributions $\rho_{\rm pair}(r)$ of the three-α system in cold neutron matter of various k_F with (a) AB and (b) OCM.

This model dependence of the system energy comes from the difference of the internal structure of the relative wave function between α clusters. To see such difference explicitly we calculate the pair density distributions defined by

$$\rho_{\rm pair}(r) = \left\langle \frac{\delta(|\boldsymbol{r}_1 - \boldsymbol{r}_2| - r)}{4\pi r^2} \right\rangle, \tag{4.10}$$

where the bracket denotes the expectation value with the first excited state wave function of the three-α system and $4\pi \int_0^\infty r^2 \rho_{\rm pair}(r) dr = 1$. Figure 4.6 compares the results for the pair density distribution obtained at various k_F. For AB, the amplitude of the wave function is strongly suppressed due to the repulsive potential component at short distances, $\lesssim 2$ fm, while the peak of the amplitude, located near the potential minimum that arises from $U^{(3)}$, naturally increases with k_F or M^*. In the OCM results, on the other hand, an oscillatory behavior is found at distances $\lesssim 3$ fm due to the orthogonality condition to the Pauli forbidden

states. Since a significant amount of amplitude is present in such an internal region, the wave function in this region is strongly modified as the Hamiltonian changes. For larger k_F or M^*, the amplitude of the internal wave function becomes larger, which is natural considering that heavier α particles are more difficult to move near the OCM potential minimum of zero separation.

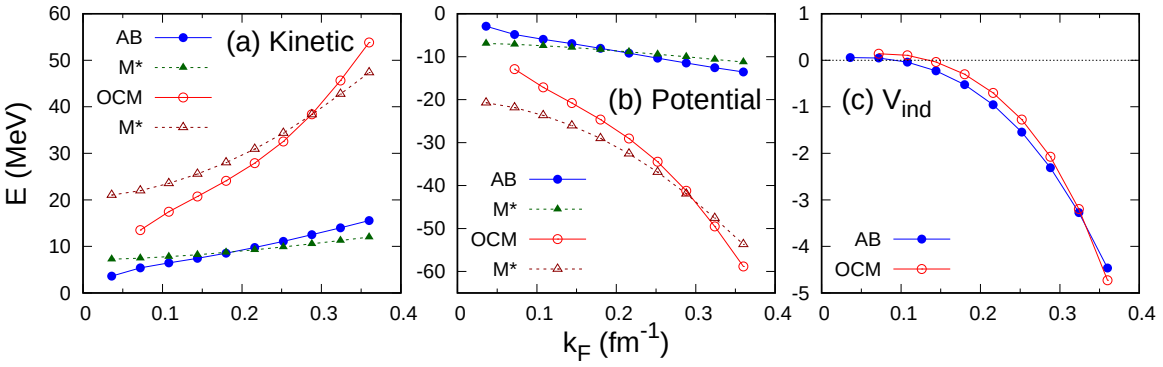

Figure 4.7: Decomposition of the total three-α energy into the kinetic term (a), the direct potential term (b), and the induced interaction term (c), which are calculated with AB and OCM as a function of the neutron Fermi momentum. See text for details. The thin horizontal line in the panel (c) indicates zero. This figure is taken from the Ref. [110]

We conclude this section by examining how the difference in the pair density distribution between AB and OCM is reflected in the expectation values of the Hamiltonian terms. Figure 4.7 displays decomposition of the total energy into the contributions of the kinetic, direct interaction, and induced interaction terms. Since the OCM wave function has its internal amplitude disturbed drastically by the medium, the expectation value of the kinetic energy rapidly increases as the k_F increases for OCM, as can be seen from Fig. 4.7 (a). This energy cost is dominated by the energy gain from the direct term $\left\langle \sum_{ij} U^{(2)}_{ij} + U^{(3)} \right\rangle$ as plotted in Fig. 4.7 (b), which is in turn controlled by the two-body OCM potential responsible for the zero-separation potential minimum. For the AB model, the same kind of behavior of both terms occurs, but the medium effects are suppressed due to the repulsive nature of the AB potential at short distances. Finally, Fig. 4.7 (c) compares the sum of the expectation values from the induced two- and three-body interactions $\left\langle \sum_{ij} V^{(2)}_{\mathrm{eff};ij} + V^{(3)}_{\mathrm{eff}} \right\rangle$ (denoted by $\mathrm{V_{ind}}$) between AB and OCM. In either case, the contribution of the induced three-body force is about one or two orders of magnitude smaller than that of the induced two-body force. The model dependence of the induced interaction term is appreciable at large k_F, a feature that stems from the difference in the amplitude of the wave function near zero separation via the induced two-body force. At small k_F, the expectation values of the induced two and three-α interactions become positive, where the magnitude of the repulsive induced three-α interaction is larger than that of the induced two-α interaction. This confirms why we do not find any stable Hoyle state for the OCM result with $k_F = 0.036$ fm^{-1}.

The decomposition in the absence of the induced two- and three-body interactions is also plotted in Figs. 4.7 (a) and (b) as denoted by M^*. We see that both the kinetic and direct interaction terms almost follow the full calculations. Since the contributions from the induced interactions are minor, i.e., one order of magnitude smaller than the expectation values of the

kinetic and direct interaction terms, the k_F dependence is predominantly determined by the Hamiltonian in the absence of the medium effects except the effective mass correction. The modeling of the α cluster structure is more essential than the medium-induced interactions to describe the k_F dependence of the properties of the three-α system in cold neutron matter.

4.4 Conclusion and future prospective

The possibility that normally resonant two- and three-α systems become bound in cold neutron matter has been pointed out for the first time by combining precise quantum-mechanical calculations with a polaron picture of α particles. We have examined two standard α-cluster models that take into account the Pauli principle in a different way, i.e., via the Pauli potential and the orthogonality condition to the Pauli forbidden bound states. We have shown that the ground state of ^{8}Be and the Hoyle state can be bound at $k_F \gtrsim 0.08$–0.11 fm^{-1} and $k_F \gtrsim 0.16$–0.22 fm^{-1}, respectively, for the two models. The presence of these light nuclear ingredients as bound states would give a significant impact on the modeling of matter in stellar collapse and neutron star mergers and also affect reaction rates for nucleosynthesis therein.

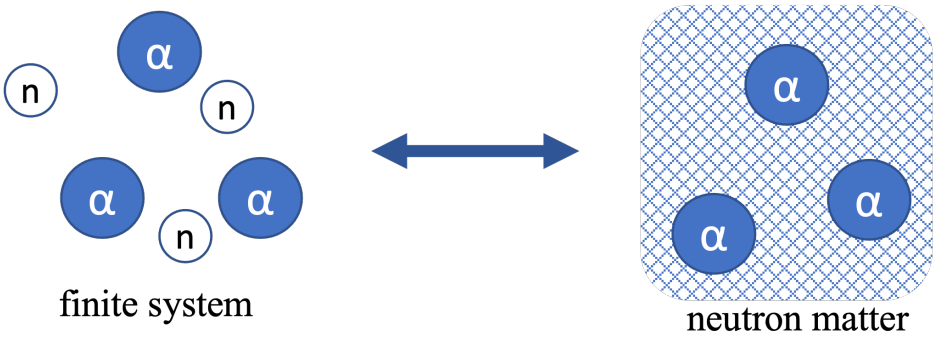

Figure 4.8: The schematic figure shows that the in-medium effects of the neutron matter to the α cluster systems are realized in the finite neutron system.

It is interesting to note that the in-medium attraction discussed in this work has to be realized in finite nuclear systems (schematically depicted in the Fig. 4.8), e.g., Be and C isotopes, where the α cluster structure is well developed. See, e.g., Ref. [123] and references therein. Isotope dependence of the structure of $2\alpha + Xn$ and $3\alpha + Xn$ systems would drop a hint at the stability of α clusters in cold neutron matter. As this is just the first evaluation, for simplicity, we ignore the distortion of an α particle and the Pauli constraint of the relative wave function of α particles by the surrounding neutron matter. The latter contribution would work as repulsion and might counteract the stability of the 'bound' ^{8}Be and Hoyle states. α particles and neutron are usually correlated in p-wave due to the Pauli principle. Recently, the p-wave polaron picture of α particles and neutron matter has been developed [124]. In that study, it is shown that the α particle and neutron, ^{5}He possibly become bound state, while the ground state of the ^{5}He is known as the resonance state in vacuum. This fact might change our results drastically.

Moreover, finite temperature effects would be important in core-collapse supernovae and neutron star mergers. Although we use the zero-temperature results for in-medium excitation properties of a single α particle and induced two- and three-α interactions, the description of

such in-medium properties can be extended to the finite-temperature case along the theoretical developments in cold atom physics [125–127].

Chapter 5

Novel approach to the removal of the Pauli forbidden states in the multi-α systems

I propose the new forbidden free basis function of multi cluster systems in which anti-symmetrization are analytically implied by the Slater determinant. Comparing with the conventional method, i.e., the orthogonal condition model (OCM) and Kukulin's projection operator that numerically exclude forbidden states, I demonstrate efficiency of the new basis function with the ^{12}C, three-alpha system. I see that the strong ^{8}Be correlation in the Hoyle state originated from the orthogonality between alpha clusters.

5.1 Introduction

A cluster is an essential aspect of nuclear structure, particularly to understand the low lying state of light nuclei. One of the most important cluster is ^{4}He, α cluster, which is a tightly bound system [3]. In particular the ^{12}C has been studied actively by the three-α cluster model because of its first excited state of $J^{\pi} = 0^{+}$ known as the Hoyle state [7] located at slightly above the three-α threshold in which well developed three α clusters have gas-like structure and bosonic condensation state in the S orbit [26, 27]. It is also known that, in the Hoyle state, the $^{8}\mathrm{Be}(0^{+}) + \alpha$ configuration is significantly large [**?**, 19, 22, 23]. Consequently, the three α clusters in the Hoyle state configure in the acute-angle isosceles triangle [110].

It is interesting to ask the question, from what does the $^{8}\mathrm{Be}(0^{+}) + \alpha$ structure emergence comes? To give answer this question, I need to discuss the origin of the structure of the Hoyle state. If its origin is universal to the same-mass multi cluster systems, the discussion of the three-α structure naturally can be extended to 4α, 5α, and more-α systems which are also candidate of the α condensation discussed in theoretically [**?**, **?**, **?**, 26, 58] and experimentally [128, 129].

The structure of the Hoyle state has been well understood by the microscopic calculations in which the nucleons are degree of freedom and the Pauli principle is properly taken into account by the antisymmetrization. The $N\alpha$-cluster condensate type microscopic wave function [26], so called "THSR" wave function has been proposed, which describes the α clusters occupying the same S orbit. This $N\alpha$ condensate wave function has been confirm to be almost equivalent to the full microscopic three-α wave function by Uegaki et al. [19, 20], and

Kamimura [21]. Moreover, in the Ref. [27], the "THSR"-type wave function orthogonal to the lowest energy state has been shown to perfectly reproduce the wave function by Uegaki et al. [19,20], and Kamimura [21]. In their conclusion the Hoyle state has a gas-like structure with three-α Bose condensation. The "THSR"-type wave function has been also applied to the more-*alpha* systems, e.g., ^{16}O [26], ^{20}Ne [**?**].

On the contrary, in the macroscopic framework where the clusters are treated as structureless point particles, multi-cluster systems have been studied mainly by the orthogonality condition model (OCM) [16–18]. In the OCM, the Pauli forbidden states [**?**] are numerically excluded by the projection operator [54] having the large strength λ MeV defined as

$$\Lambda = \lambda \sum_{nlm \in \text{f.s.}} |\phi_{nlm}\rangle \langle \phi_{nlm}| \,. \tag{5.1}$$

However, calculations using the projection operator become unstable and inefficient [59], which makes calculation of more-*alpha* systems difficult. So far, only four-α OCM calculation by the Funaki et al. [58] has been reported and 5α OCM calculation has not been reached yet.

To overcome the difficulties in the macroscopic calculation for cluster model, in this paper, I propose the novel macroscopic forbidden free basis function derived from the microscopic multi-cluster wave function and present its efficiency by calculating three-α system, ^{12}C. Using the novel basis function, I see the agreement on the Hoyle state structure with the microscopic wave function, namely THSR wave function.

In the next section, I will describe the derivation of the novel basis function and the macroscopic three-α model. In the Sec. 5.3, I will demonstrate the efficiency of the novel basis function by comparing with conventional basis function. Considering the "THSR"-type wave function in the macroscopic framework , I discuss the three-α structure in the Hoyle state by the density distributions. In the end, Sec. 5.4, I summarized strong points and possibilities of the novel basis function.

5.2 Formalism

5.2.1 Forbidden free correlated Gaussian

For a stable calculation of multo-cluster systems in the macroscopic framework, I introduce the novel forbidden free basis function in this section. Here, I only focus on the $N\alpha$-cluster systems. An application for the arbitral cluster systems is straightforward. Starting from a microscopic wave function, I consider the spectroscopic amplitude (SA) of the constituent clusters as the novel macroscopic basis function which properly satisfies the Pauli principle. By using this basis function, one can avoid numerically unstable calculation, particularly the pseudo-potential projecting onto the Pauli forbidden states.

Generally, a microscopic wave function of N-cluster system consisted of clusters, $C_1 \dots C_N$, can be written as an antisymmetrized product of internal wave functions of clusters $\phi(C_i)$ and a wave function of relative motion of clusters $\chi(\boldsymbol{x}_1, \dots \boldsymbol{x}_N)$:

$$\Psi_{\text{micro}} = \mathcal{A}\left[\phi(C_1) \cdots \phi(C_N)\chi(\boldsymbol{x}_1, \dots \boldsymbol{x}_N)\right], \tag{5.2}$$

where $\mathcal{A}$ stands for the antisymmetrizer that properly makes the wave function satisfy the

Pauli principle. A set of relative Jacobi coordinate $\tilde{\boldsymbol{x}} = (\boldsymbol{x}_1, \ldots \boldsymbol{x}_N)$ is defined by

$$\boldsymbol{x}_1 = \boldsymbol{R}_2 - \boldsymbol{R}_1 \tag{5.3}$$

$$\boldsymbol{x}_2 = \frac{\boldsymbol{R}_1 + \boldsymbol{R}_2}{2} - \boldsymbol{R}_3 \tag{5.4}$$

$$\vdots \tag{5.5}$$

$$\boldsymbol{x}_N = \frac{\boldsymbol{R}_1 + \boldsymbol{R}_2 + \cdots + \boldsymbol{R}_N}{N},$$

where the $\boldsymbol{R}_i$ indicate the position vector of the center-of-mass of the ith cluster. I ignore the center-of-mass motion of the entire system, thus I omit the dependence on the $\boldsymbol{x}_N$ from χ in the followings.

Let us consider the test function Ψ_t defined as

$$\Psi_t = \mathcal{A}\left[\phi(C_1)\cdots\phi(C_N)\delta(\boldsymbol{x}_1 - \boldsymbol{t}_1)\cdots\delta(\boldsymbol{x}_{N-1} - \boldsymbol{t}_{N-1})\right] \tag{5.6}$$

which pins clusters down at the specific coordinate $\tilde{\boldsymbol{t}} = (\boldsymbol{t}_1, \ldots, \boldsymbol{t}_{N-1})$. Then, the SA can be described as

$$g(\boldsymbol{t}) = \langle \Psi_t | \Psi_{\rm micro} \rangle \tag{5.7}$$

$$= \int d\boldsymbol{t}' N(\boldsymbol{t}, \boldsymbol{t}')\chi(\boldsymbol{t}') \equiv \mathcal{N}\chi(\boldsymbol{t}), \tag{5.8}$$

where $N(\boldsymbol{t}, \boldsymbol{t}') = \langle \Psi_{\boldsymbol{t}} | \Psi_{\boldsymbol{t}'} \rangle$ is the norm kernel. Considering the orthonomality of the microscopic wave function,

$$\langle \Psi_{\rm micro} | \Psi'_{\rm micro} \rangle = \langle \chi | \mathcal{N}\chi' \rangle = 0 \text{ or } 1, \tag{5.9}$$

the properly normalized wave function of relative motion of the clusters in the microscopic framework should be $\Psi_{\rm rel.} = \mathcal{N}^{1/2}\chi$. On the other hand for the macroscopic cluster model, the orthonomality condition is approximately made by taking only the diagonal part of $\mathcal{N}$: $\langle \chi\mathcal{N} | \mathcal{N}\chi' \rangle = 0$ or 1. Therefore, the novel basis function in the macroscopic framework is turned out to be $\psi = g/\sqrt{\langle g|g \rangle}$ in which the Pauli principle is properly satisfied.

The SA of the constituent clusters, $C_1 \ldots C_N$, can be analytically derived if χ is described by the correlated gaussian (CG) [64]:

$$G(A_i, \boldsymbol{x}) = \exp\left(-\frac{1}{2}\nu\tilde{\boldsymbol{x}}A_i\boldsymbol{x}\right), \tag{5.10}$$

where A_i is positive definite $(N-1)\times(N-1)$ symmetric matrix. $\tilde{\boldsymbol{x}}A_i\boldsymbol{x}$ is a brief writing of $\sum_{n,m} A_{i,nm}\boldsymbol{x}_n \cdot \boldsymbol{x}_m$. In the appendix of Ref. [80], detail steps of calculation for the SA are explained on the assumption that the internal wave function of all clusters are described with the same $(0s)$ harmonic oscillator. The parameter ν fm^{-2} is the size parameter of the $(0s)$ harmonic oscillator. Following that steps, the novel basis function finally can be written as

$$\psi^{\rm NB}(A_i, \boldsymbol{x}) = \sum_p F_p \left(\frac{\det(Q+\Gamma)}{\det M_p}\right)^{\frac{3}{2}} \times \exp\left\{-\frac{1}{2}\nu\tilde{\boldsymbol{x}}(\Gamma - 4W_pM_p^{-1}W_p^{-1}\widetilde{W}_p)\boldsymbol{x}\right\}. \tag{5.11}$$

The reduced mass matrix Γ is defined by $\Gamma_{ij} = 2\mu_i\delta_{ij}$, where the reduced mass factors of the same mass clusters are

$$\begin{cases} \mu_i = \dfrac{4i}{i+1} & (i = 1, \cdots, N-1) \\ \mu_N = 4N \end{cases} \tag{5.12}$$

The $(N-1)\times(N-1)$ matrices Q and M_p are defined by

$$Q = \Gamma(\Gamma - A_i)^{-1}\Gamma - \Gamma \tag{5.13}$$

$$M_p = Q + \frac{1}{2}\Gamma + 2\widetilde{W_p}\Gamma^{-1}W_p. \tag{5.14}$$

The coefficient F_p and $(N-1)\times(N-1)$ matrix W_p can be determined by the algebraic manipulations in the calculation of the SA. It is note that the SA also can be described by the superposition of correlated Gaussian, which is a convenient feature for evaluation of matrix elements. For example, the case of $N\alpha$ systems, the practical number of terms in the novel basis function is 5, 120, and 10147 for 2α, 3α, and 4α, respectively. Derived F_p and W_p are provided in the supplemental material.

5.2.2 Two- and three-alpha model

To demonstrate efficiency of the novel basis function, I adopt the case of the two- and three-α system. The Hamiltonian is reads

$$H = \sum_{i=1}^{N} T_i - T_{\rm cm} + \sum_{i>j=1}^{N}\left(V_{2\alpha}^{ij} + V_{\rm Coul.}^{ij}\right), \tag{5.15}$$

where T_i is the kinetic energy of ith particle and the kinetic energy of the center-of-mass motion $T_{\rm cm}$ is excluded. $V_{2\alpha}$ is the two-α interaction that is the same used in the Ref. [73], which is derived by a folding procedure with an effective nucleon-nucleon interaction. $V_{\rm Coul.}$ is the Coulomb interaction that is also taken as used in the Ref. [73]. $V_{3\alpha}$ is the J^π dependent three-α interaction taken from Ref. [**?**] to adjust the three-α threshold, which is introduced for three-α case. The mass parameter of the α particle and the elementary charge are $\hbar^2/m_\alpha = 10.654$ MeV fm^2 and $e^2 = 1.440$ MeV fm^2, respectively. I utilize the SVM to obtain wave function with this new basis function.

5.3 Results

5.3.1 Test convergence

I present numerical efficiency of the novel basis function in this section. Here I take $\nu = 0.26$ fm^{-2} that reproduces the size of the α particle [80]. I compare the novel basis function with the fully symmetrized CG: $\psi_i^{CG} = \mathcal{S}G(A_i, \boldsymbol{x})$, where the $\mathcal{S}$ is a symmetrizer which makes the CG symmetric under all exchanges of α particles to ensure the bosonic property of α particles. Note that the fully symmetrized CG is not orthogonal to the forbidden states and the pseudo-potential Γ defined in the eq. (5.1) is needed to impose the orthogonality condition. For the fair comparison, the conditions of the SVM is arranged in common: (i) number of the candidates are 20 for each dimension, (ii) the variational parameter A_i is randomly generated

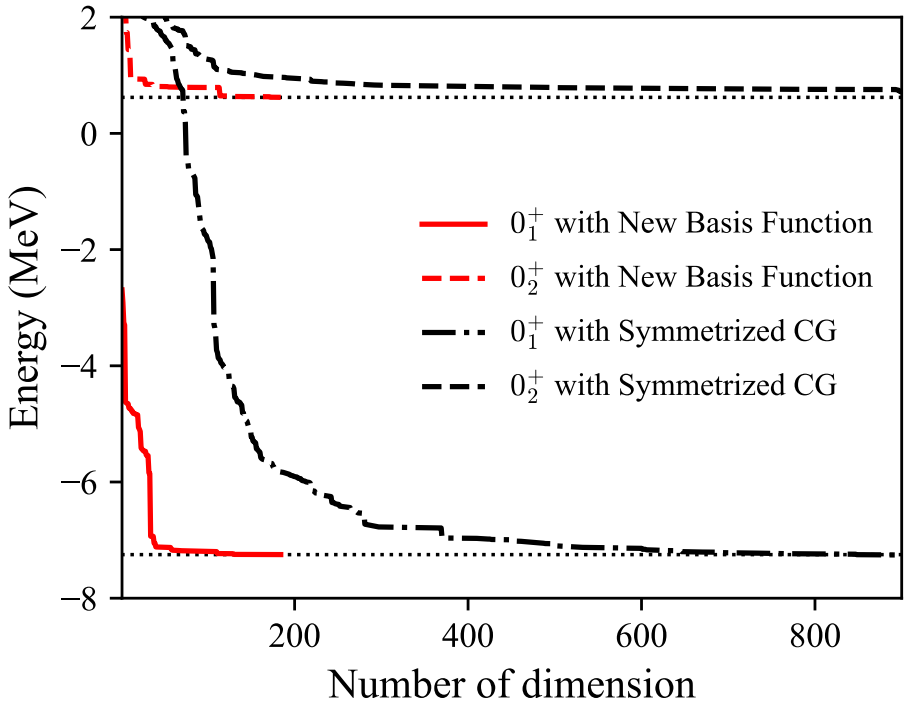

Figure 5.1: Convergence curve of the $J^\pi = 0^+$ states energies calculated by the novel basis functions (solid and dashed lines) and the fully symmetrized CG and the pseudo potential defined in the eq. (5.1) (dashed and dash-dot lines). The dotted line are converged energies, -7.25 MeV and 0.75 MeV for 0_1^+ and 0_2^+ states, respectively.

by $A_i = \mathcal{R}(\theta)a$, where $\mathcal{R}(\theta)$ is the rotation matrix and $a(b_1, b_2)$ is a diagonal matrix defined as

$$a_i(b_1, b_2) = \begin{pmatrix} 1/b_1^2 & 0 \\ 0 & 1/b_2^2 \end{pmatrix}. \tag{5.16}$$

θ, b_1, and b_2 are randomly generated in the range of $0 < \theta < 2\pi$ and $b_1/\sqrt{\nu}, b_2/\sqrt{\nu} < 12$ fm.

Figure 5.1 plots the energy convergence for the number of basis functions, K. It can be seen that the number of the basis function for the convergence of energy by the novel basis function is surprisingly smaller than that by the fully symmetrized CG. The energy calculated by the fully symmetrized CG is not bound at smaller $K \lesssim 100$ because the CG has the large Pauli forbidden component in the fully symmetrized CG and need to be orthogonal to them. On the other hand for the novel basis function which is properly orthogonal to the Pauli forbidden states, the energy start bound with small K.

5.3.2 Macroscopic "THSR"-type wave function

The novel basis function can describe "THSR"-type wave function in macroscopic framework if I consider A_i is a diagonal matrix, $A_i = a_i$. In the Fig. 5.2 I show the energy surface of $J^\pi = 0^+$ as a function of the b_1 and b_2. Energies along $b_1\sqrt{\nu} \sim 1$ fm is exceptionally high because the relative motion between two α particles is forbidden. In the area where b_1 and b_2 are small, $b_1/\sqrt{\nu} \lesssim 1$ fm and $b_2/\sqrt{\nu} \lesssim 1$ fm, energies are very high because the clusters are too close to satisfy the orthogonality condition. In the area where 1 fm $\lesssim b_1/\sqrt{\nu} \lesssim 2$ fm and

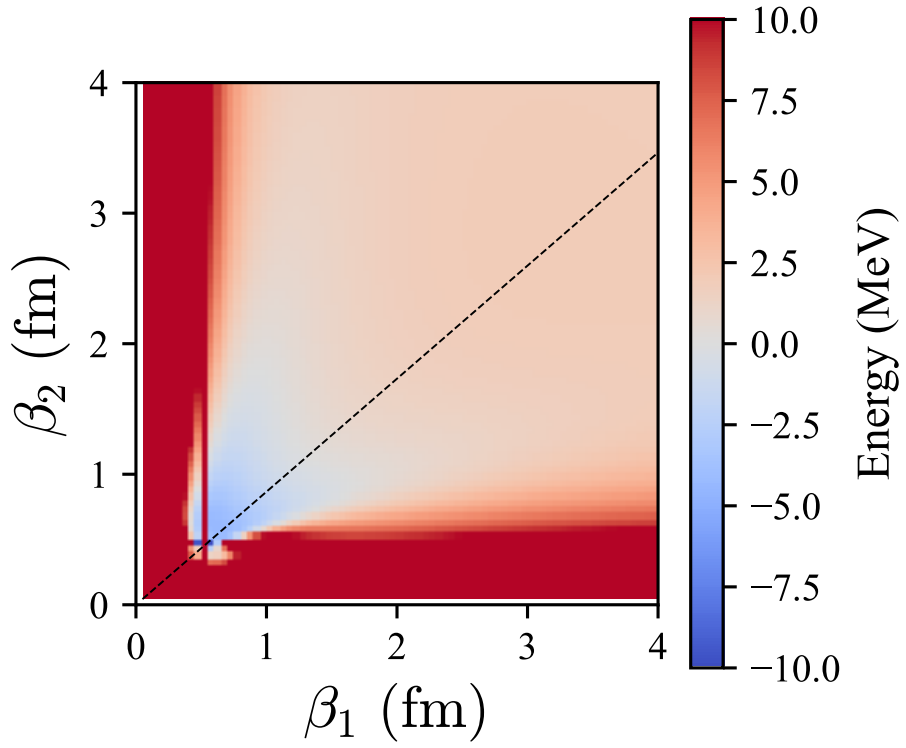

Figure 5.2: The energy surface calculated with THSR-type wave function. The cross symbol indicates the lowest energy -4.34 MeV at $(b_1/\sqrt{\nu}, b_2/\sqrt{\nu}) = (1.18, 1.08)$. The black dashed line shows $b_2 = \sqrt{3}b_1/2$ line representing the b_1 and b_2 ratio of the equilateral triangle configuration.

1 fm $\lesssim b_2/\sqrt{\nu} \lesssim$ 2 fm, the three-α system is bound and the lowest energy is -4.34 MeV at $(b_1/\sqrt{\nu}, b_2/\sqrt{\nu}) = (1.18, 1.08)$ fm, which is consistent location with the Ref. [27].

The right panel of the Fig. 5.3 shows the overlap with the wave function of the Hoyle state obtained by the full calculation, $\langle \psi^{\mathrm{THSR}} | \Psi(J^\pi = 0_2^+) \rangle$. Similarly to the energy surface, the forbidden line along $b_1/\sqrt{\nu} \sim 1$ fm can be seen, in which the overlap is difficult to evaluate numerically due to the cancellation of significant digits where the wave function is Pauli forbidden.

Dashed line in the Fig. 5.2 is corresponding to the condition $b_2 = \sqrt{3}b_1/2$ which indicates that three α particles are configured in symmetric way, indicating the equilateral triangle same as the Ref. [26]. Along the dashed line, the highest overlap with the Hoyle state is 0.83 at $(b_1/\sqrt{\nu}, b_2/\sqrt{\nu}) = (5.32, 4.61)$ fm.

In the overlap surface, there are mainly two areas having different phases: one is the area spanned by 1 fm $\lesssim b_1\sqrt{\nu} \lesssim$ 2 fm and 0 fm $\lesssim b_2\sqrt{\nu} \lesssim 0.8$ fm, the other is the area spanned by $b_1/\sqrt{\nu} \gtrsim 1$ fm and $b_2/\sqrt{\nu} \gtrsim 0.1$ fm. The former area contains the lowest energy location. On the other hand, the largest overlap with the Hoyle state is located at $(b_1/\sqrt{\nu}, b_2/\sqrt{\nu}) = (2.30, 7.69)$ fm in the latter area, in which the distance between two-α particles are smaller than the distance between the center-of-mass of two-α particles and the left α particle. The amount of overlap at that point is 0.90 that is consistent with the diagonal element of the overlap matrix $\langle g_i | g_j \rangle$ $i, j = 0_1^+, 0_2^+$ in the Ref. [80].

Furthermore, we can consider two-basis model using two novel basis function mentioned in

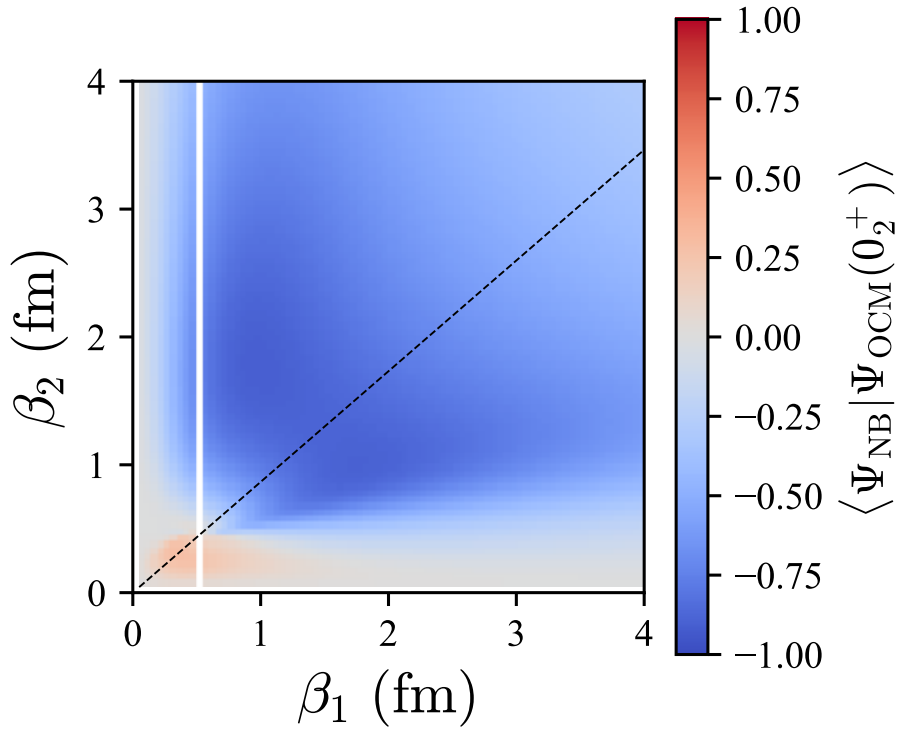

Figure 5.3: The overlap of the THSR wave function and the wave function of 0_2^+ state calculated by the SVM. The cross symbol indicates the largest overlap 0.90 at $(b_1/\sqrt{\nu}, b_2/\sqrt{\nu}) = (2.30, 7.69)$ The black dashed line shows $b_2 = \sqrt{3}/2 b_2$ line representing the b_1 and b_2 ratio of the equilateral triangle configuration.

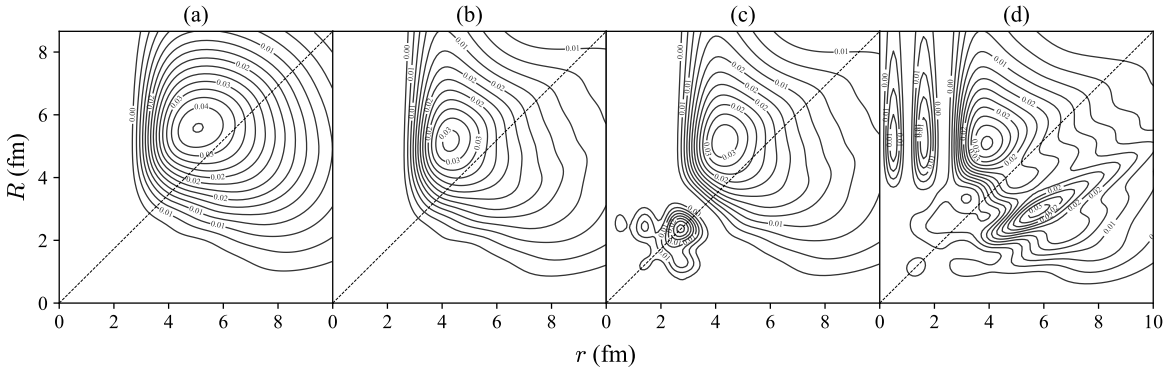

Figure 5.4: Two-body density distribution of (a)THSR-type restricted in $b_2 = \sqrt{3}b_1/2$, (b)THSR-type, (c)two-basis model, and (d)the Hoyle state by the SVM.

one basis model: the basis function that reproduces the lowest energy and the basis function that has the largest absolute overlap with the Hoyle state. Note that the wave function of the 0_1^+ and 0_2^+ are orthogonal by the diagonalization. Obtained energies of 0_1^+ and 0_2^+ are -4.34 MeV and 1. MeV, respectively.

To see the three-α structure of the Hoyle state, I show two-body density distributions (TBD) of "THSR"-type model, one-basis model, two-basis model, and full calculation in Fig. 5.4, which is defined as

$$\rho(r, R) = \langle \Psi | \delta(|\boldsymbol{x}_1| - r)\delta(|\boldsymbol{x}_2| - R)|\Psi\rangle \,. \tag{5.17}$$

TBD satisfies the normalization $\iint drdR\, \rho(r, R) = 1$. The diagonal dashed line is $R = \sqrt{3}r/2$ representing the equilateral triangle ratio of r and R. For the THSR-type model restricted in $b_2 = \sqrt{3}b_1/2$ and THSR-type model, the amplitude of the three α particles are widely spread with the peak at above the black dashed line representing the equilateral triangle configuration.

For the two-basis model, nodal behavior in the internal region emerge due to the orthogonality to the ground state. Comparing with the TBD by the full calculation, I see that TBD by the two-basis model reproduces structure of the Hoyle state except for nodal behavior in the range of 3 fm $\lesssim R \lesssim$ 8 fm and 0 fm $\lesssim r \lesssim$ 2 fm. Structure of the Hoyle state is originated from the orthogonality condition of the clusters and orthogonality to the ground state, which is consistent with the analysis by the microscopic THSR-type wave function [26, 27].

5.4 Summary

I propose the novel macroscopic basis function for the multi-cluster systems, starting form the microscopic multi-cluster wave function. Taking ^{12}C, three-α system as an example, I have presented the efficiency of the novel basis function. The number of basis function that need to converge eigen energy is surprisingly small, compared with the conventional OCM calculation by the fully symmetrized CG. Using THSR-type wave function in macroscopic framework, I also investigate the origin of the three-α configuration in the Hoyle state, which is determined by the orthogonality condition of the clusters and orthogonality to the ground state. That is agree with the previous studies by the microscopic cluster model. The calculation with the novel basis function is numerically stable because the Pauli principle is properly taken into

account. This advantages might pave the way to the heavier cluster systems, such as ^{16}O, ^{20}Ne, and so on. Further studies will be reported elsewhere.

Chapter 6

Conclusion of this dissertation

We have made comprehensive studies of ^{12}C by precise three-α cluster model wave functions obtained by the stochastic variational method with the correlated Gaussian basis functions. For future studies, a novel approach for more complex multi-cluster systems was also implemented.

In chapter 3, I showed the three-α cluster strucutre in the spectrum of ^{12}C by analyzing three-body wave functions. In the algebraic cluster model, the three-α particles are configurated into the equilateral triangle and they are vibrating and rotating. Based on this idea three-α geometric configurations were discussed through the density distributions, reduced width amplitudes, and the partial wave components without any geometrical assumptions. It is conluded that the $J^\pi = 0^+_1$ and 2^+_1 states are found to have the equilateral triangle configuration, on the other hand, 0^+_2, the Hoyle state and 2^+_2 state have isosceles triangles that indicates ^{8}Be+α structure. These findings are consistent with the previous works. It is also found that the 2^+_2 state is mainly excited by the relative coordinate between ^{8}Be and α as concluded in the Refs [19,20,70]. Due to the higher excitation energy of ^{8}Be(2^+) than that of 2^+_2 state, ^{8}Be subsystem is hardly exicited and the partial wave component of $l_1 = 2$ is strongly suppressed. Therefore, I conclude that the 2^+_2 is not ideal member of rigid rotational excitations, the Hoyle band, which is contradict to the concept of the ACM. Analysis of 4^+_2 state is also interesting, which is also a candidate of the Hoyle band member.

In chapter 4, I presented that the energy shifts and the structure chainges of the Hoyle state in cold dilute neutron matter, which situation may be realized in the astrophysical explosive phenomena such as core collapse supernovae or the neutron star mergers. The in-medium effect from the cold dilute neutron matter is evaluated based on the idea of the Fermi polarons for the first time. I found that the Hoyle state starts to bound in the neutorn matter having the Fermi momentum $k_F \gtrsim$ 0.16-0.22 fm^{-1} for the OCM and the AB. ^{8}Be is also confirmed to be stabilized in the neutron matter. The stabilization of the ingredients of the nucleosynthesis process, e.g., the triple alpha process, may affect the reaction rate or even modeling in the astrophysics. It is noted that the presented evaluation of in-medium effects is rather drastic to simulate realistic situation because, in our model, the α particles couple with background neutrons via only s wave, although α and neutrons generally couple via p wave due to the Pauli principle. Recently, to extend the α polaron picutre to the p wave coupling I investigate the ^{5}He as the $n + \alpha$ [124]. The ground state of ^{5}He is known as the $J^\pi = 3/2^-$ resonant state, which become bound state in the dilute neturon matter because the decay prosecc is forbidden due to the Pauli principle of background neutrons. These investigation

will show us the possibilities for the new physics that finite nuclear systems in medium are explicitly described, which is nessesary to be considered for applications to astrophyscis or clustering phenomena in heavy-mass nuclei.

In chapter 5, I suggested the novel approach for the multi-cluster systems. Started from the microscopic cluster wave function, the new basis function in macroscopic framework is implemented, in which the Puali principle is properly taken into account. Taking two- and three-α system as examples, I showed drastic reduction of number of dimension to obtain converged results, which shows how the new basis functions are efficient. The new basis function can simpulate THSR wave function in macroscopic framework. It is confirmed that the three-α strucutre of the Hoyle state by the new basis function reproduced relsults by the THSR wave function. The convergence with small basis function is strong advantage for the four- or more-α systems such as ^{16}O and ^{20}Ne.

In conclusion, I remark the points of the understanding of ^{12}C that become deeper and extended through these comprehensive studies. First, three-α cluster sturcutre in the ^{12}C spectrum are systematicallly analyzed with the precise wave functions. Second, new physics of ^{12}C in medium has been developed from the investigation on the Hoyle state in the cold dilute neutron matter, which may be relaized in the astrophysical environment and the medium-heavy mass nuclei. Third, the novel approach for multi-cluster systems has been implemented, which may overcome the difficulties of OCM calculations.

Appendix A

Matrix elements with the correlated Gaussian basis

Matrix elements with the correlated Gaussians and single global vector are presented. The calculation method and ideas are based on the Refs. [67, 130] Many body wave function is expanded by the correlated gaussians.

$$\Psi = \sum_k c_k \phi_k \tag{A.1}$$

$$\phi_k = \exp\left(-\frac{1}{2}\tilde{\boldsymbol{x}} A_k \boldsymbol{x}\right) |\boldsymbol{u}\cdot\boldsymbol{x}|^L Y_{LM}(\boldsymbol{u}\cdot\boldsymbol{x}) \tag{A.2}$$

where the $\boldsymbol{u}$ is the global vector.

$$\boldsymbol{u} = (u_1, \ldots, u_{N-1}) \tag{A.3}$$

A.1 Overlap

The overlap element is

$$\langle\phi_k|\phi_{k'}\rangle = \frac{(2L+1)!!}{4\pi}\left(\frac{(2\pi)^{N-1}}{\mathrm{detB}}\right)^{\frac{3}{2}} \rho^L \tag{A.4}$$

where

$$B = A_k + A_{k'} \tag{A.5}$$

$$\rho = \tilde{u}' B^{-1} u \tag{A.6}$$

If the total angular momentum is 0, the global vector is not needed. Then the trial function is

$$\phi_k = \exp\left(-\frac{1}{2}\tilde{\boldsymbol{x}} A_k \boldsymbol{x}\right) \tag{A.7}$$

The explicit form of overlap matrix element is

$$\langle\phi_k|\phi_{k'}\rangle = \left(\frac{(2\pi)^{N-1}}{\det(A_k + A_{k'})}\right)^{\frac{3}{2}} \tag{A.8}$$

A.2 Kinetic Energy

The matrix element of kinetic energy is

$$\langle\phi_k|\frac{1}{2}\tilde{\boldsymbol{\pi}}\Lambda\boldsymbol{\pi}|\phi_{k'}\rangle = \frac{\hbar^2}{2}(R+LQ\rho^{-1})\frac{(2L+1)!!}{4\pi}\left(\frac{(2\pi)^{N-1}}{\mathrm{detB}}\right)^{\frac{3}{2}}\rho^L \tag{A.9}$$

where

$$R = 3\mathrm{Tr}(AB^{-1}A'\Lambda) \tag{A.10}$$

$$Q = 2\tilde{u}'B^{-1}A\Lambda A'B^{-1}u \tag{A.11}$$

For the case of total angular momentum 0,

$$\langle\phi_k|\frac{1}{2}\tilde{\boldsymbol{\pi}}\Lambda\boldsymbol{\pi}|\phi_{k'}\rangle = \frac{3}{2}\hbar^2\mathrm{Tr}\left(A_k(A_k+A_{k'})^{-1}A_{k'}\Lambda\right)\langle\phi_k|\phi_{k'}\rangle \tag{A.12}$$

A.3 Two-body interaction

General form,

$$\begin{aligned}\langle\phi_k|V(|\boldsymbol{r}_i-\boldsymbol{r}_j|)|\phi_{k'}\rangle =& \frac{(2L+1)!!}{4\pi}\left(\frac{(2\pi)^{N-1}}{\mathrm{detB}}\right)^{\frac{3}{2}}\sum_{n=0}^{L}\frac{L!}{n!(L-n)!}\left(\frac{\gamma\gamma'}{c}\right)^n \\ &\times\bar{\rho}^{L-n}\frac{2^{n+2}}{\sqrt{\pi}(2n+1)!!}\int_0^\infty V\left(\sqrt{\frac{2}{c}}x\right)x^{2n+2}e^{-x^2}dx\end{aligned} \tag{A.13}$$

where

$$c^{-1} = \widetilde{\omega^{(ij)}}B^{-1}\omega^{(ij)} \tag{A.14}$$

$$\gamma = c\widetilde{\omega^{(ij)}}B^{-1}u \tag{A.15}$$

$$\gamma' = c\widetilde{\omega^{(ij)}}B^{-1}u' \tag{A.16}$$

For the case of total angular momentum 0,

$$\langle\phi_k|V(|\boldsymbol{r}_i-\boldsymbol{r}_j|)|\phi_{k'}\rangle = \langle\phi_k|\phi_{k'}\rangle\left(\frac{c}{2\pi}\right)^{\frac{3}{2}}\int V(\boldsymbol{r})\mathrm{e}^{-\frac{1}{2}cr^2}d\boldsymbol{r} \tag{A.17}$$

A.3.1 Gaussian

The matrix element of Gaussian

$$\langle\phi_k|\exp(-\beta r_{ij}^2)|\phi_{k'}\rangle = \frac{(2L+1)!!}{4\pi}\left(\frac{(2\pi)^{N-1}}{\mathrm{detB}}\right)^{\frac{3}{2}}\left(1+\frac{2\beta}{c}\right)^{-\frac{3}{2}}\left(\bar{\rho}+\frac{\gamma\gamma'}{c}\frac{1}{1+\frac{2\beta}{c}}\right)^L \tag{A.18}$$

where

$$\bar{\rho} = \rho - \frac{\gamma\gamma'}{c} \tag{A.19}$$

then

$$\langle\phi_k|\exp(-\beta r_{ij}^2)|\phi_{k'}\rangle = \frac{(2L+1)!!}{4\pi}\left(\frac{(2\pi)^{N-1}}{\mathrm{detB}}\right)^{\frac{3}{2}}\left(1+\frac{2\beta}{c}\right)^{-\frac{3}{2}}\left(\bar{\rho}+\frac{\gamma\gamma'}{c}\frac{1}{1+\frac{2\beta}{c}}\right)^{L} \tag{A.20}$$

$$= \frac{(2L+1)!!}{4\pi}\left(\frac{(2\pi)^{N-1}}{\mathrm{detB}}\right)^{\frac{3}{2}}\left(1+\frac{2\beta}{c}\right)^{-\frac{3}{2}}\left(\rho-\frac{\gamma\gamma'}{c}\frac{2\beta}{c+2\beta}\right)^{L} \tag{A.21}$$

$$= \frac{(2L+1)!!}{4\pi}\left(\frac{(2\pi)^{N-1}}{\mathrm{detB}}\right)^{\frac{3}{2}}\left(\frac{c}{c+2\beta}\right)^{\frac{3}{2}}\left(\rho-\frac{\gamma\gamma'}{c}\frac{2\beta}{c+2\beta}\right)^{L} \tag{A.22}$$

For the case of the total angular momentum 0,

$$\langle\phi_k|\exp(-\beta r_{ij}^2)|\phi_{k'}\rangle = \langle\phi_k|\phi_{k'}\rangle\left(\frac{c/2}{\beta+c/2}\right)^{\frac{3}{2}} \tag{A.23}$$

A.3.2 Shifted Gaussian

The matrix element of the shifted Gaussian $\exp(-\alpha r_{ij}^2-\beta r_{ij})$ is obtained by using eq.(A.13).

$$\langle\phi_k|\exp(-\alpha r_{ij}^2-\beta r_{ij})|\phi_l\rangle \tag{A.24}$$

$$= \frac{(2L+1)!!}{4\pi}\left(\frac{(2\pi)^{N-1}}{\mathrm{detB}}\right)^{\frac{3}{2}}\sum_{n=0}^{L}\frac{L!}{n!(L-n)!}\left(\frac{\gamma\gamma'}{c}\right)^{n}\bar{\rho}^{L-n}\frac{2^{n+2}}{\sqrt{\pi}(2n+1)!!} \tag{A.25}$$

$$\underline{\int_0^\infty \exp\left(-\left(\frac{2\alpha}{c}+1\right)x^2-\beta\sqrt{\frac{2}{c}}x\right)x^{2n+2}dx}$$

The unerlined integration is reduced to the imcomplete Gamma function.

$$\int_0^\infty \exp\left(-\left(\frac{2\alpha}{c}+1\right)x^2-\beta\sqrt{\frac{2}{c}}x\right)x^{2n+2}dx \tag{A.26}$$

$$= \int_0^\infty \exp\left(-A'x^2-B'x\right)x^{2n+2}dx \tag{A.27}$$

$$= \int_0^\infty \exp\left(-A'\left(x+\frac{B'}{2A'}\right)^2+\frac{B'^2}{4A'}\right)x^{2n+2}dx \tag{A.28}$$

$$= \exp\left(\frac{B'^2}{4A'}\right)\int_0^\infty \exp\left(-A'\left(x+\frac{B'}{2A'}\right)^2\right)x^{2n+2}dx \tag{A.29}$$

The integration part,

$$\int_0^\infty \exp\left(-A'\left(x+\frac{B'}{2A'}\right)^2\right)x^{2n+2}dx \tag{A.30}$$

$$= \int_{\frac{B'}{2A'}}^\infty \exp(-A'x^2)\left(x-\frac{B'}{2A'}\right)^{2n+2}dx \tag{A.31}$$

$$= \int_{\frac{B'}{2A'}}^\infty \exp(-A'x^2)\sum_{m=0}^{2n+2}\frac{(2n+2)!}{m!(2n+2-m)!}x^m\left(-\frac{B'}{2A'}\right)^{2n+n-m}dx \tag{A.32}$$

$$= \sum_{m=0}^{2n+2}\frac{(2n+2)!}{m!(2n+2-m)!}\left(-\frac{B'}{2A'}\right)^{2n+n-m}\int_{\frac{B'}{2A'}}^\infty \exp(-A'x^2)x^m dx. \tag{A.33}$$

By substituting $q = A'x^2$,

$$\sum_{m=0}^{2n+2} \frac{(2n+2)!}{m!(2n+2-m)!} \left(-\frac{B'}{2A'}\right)^{2n+n-m} \int_{\frac{B'^2}{4A'}}^{\infty} \exp(-q) \left(\frac{q}{A'}\right)^{\frac{m}{2}} \frac{1}{2A'} \sqrt{\frac{A'}{q}} dq \tag{A.34}$$

$$= \sum_{m=0}^{2n+2} \frac{(2n+2)!}{m!(2n+2-m)!} \left(-\frac{B'}{2A'}\right)^{2n+n-m} \frac{A'^{-\frac{1}{2}(m+1)}}{2} \int_{\frac{B'^2}{4A'}}^{\infty} \exp(-q) q^{\frac{1}{2}(m+1)-1} dq \tag{A.35}$$

$$= \sum_{m=0}^{2n+2} \frac{(2n+2)!}{m!(2n+2-m)!} \left(-\frac{B'}{2A'}\right)^{2n+n-m} \frac{A'^{-\frac{1}{2}(m+1)}}{2} \Gamma\left(\frac{1}{2}(m+1), \frac{B'^2}{4A'}\right), \tag{A.36}$$

where the $\Gamma(a,b)$ is the imcomplete Gamma function. Finally

$$\langle \phi_k | \exp(-\alpha r_{ij}^2 - \beta r_{ij}) | \phi_l \rangle \tag{A.37}$$

$$= \frac{(2L+1)!!}{4\pi} \left(\frac{(2\pi)^{N-1}}{\mathrm{detB}}\right)^{\frac{3}{2}} \sum_{n=0}^{L} \sum_{m=0}^{2n+2} \frac{L!}{n!(L-n)!} \left(\frac{\gamma\gamma'}{c}\right)^n \bar{\rho}^{L-n} \frac{2^{n+2}}{\sqrt{\pi}(2n+1)!!}$$
$$\exp\left(\frac{B'^2}{4A'}\right) \frac{(2n+2)!}{m!(2n+2-m)!} \left(-\frac{B'}{2A'}\right)^{2n+n-m} \frac{A'^{-\frac{1}{2}(m+1)}}{2} \Gamma\left(\frac{1}{2}(m+1), \frac{B'^2}{4A'}\right) \tag{A.38}$$

$$= \frac{(2L+1)!!}{4\pi} \left(\frac{(2\pi)^{N-1}}{\mathrm{detB}}\right)^{\frac{3}{2}} \exp\left(\frac{B'^2}{4A'}\right) \sum_{n=0}^{L} \sum_{m=0}^{2n+2} \frac{L!(2n+2)!}{n!(L-n)!m!(2n+2-m)!(2n+1)!!}$$
$$\left(\frac{\gamma\gamma'}{c}\right)^n \bar{\rho}^{L-n} \frac{2^{m-n-1}}{\sqrt{\pi}} A'^{\frac{m}{2}-2n-\frac{5}{2}} (-B')^{2n+2-m} \Gamma\left(\frac{1}{2}(m+1), \frac{B'^2}{4A'}\right) \tag{A.39}$$

where

$$A' = \frac{2\alpha}{c} + 1 \tag{A.40}$$

$$B' = \beta\sqrt{\frac{2}{c}}. \tag{A.41}$$

When $\alpha = 0$, the present matrix element is reduced to the matrix element of the exponential funtion. On the other hand when $\beta = 0$, the matrix element is reduced to the matrix element of the Gaussian just explained in Sec. **??**.

A.3.3 Coulomb potential

The matrix element of the Coulomb potential can be calculated by the Gaussian expansion.

$$\frac{1}{r} = \frac{2}{\sqrt{\pi}} \int_0^{\infty} dt \exp(-r^2 t^2) \tag{A.42}$$

$$\frac{1}{r}\mathrm{erf}(\kappa r) = \frac{2\kappa}{\sqrt{\pi}} \int_0^{1} dt \exp(-\kappa^2 r^2 t^2) \tag{A.43}$$

The Regular Coulomb potential

$$\langle\phi_k|\frac{1}{r}|\phi_{k'}\rangle \tag{A.44}$$

$$=\frac{2}{\sqrt{\pi}}\int_0^\infty dt\,\langle\phi_k|\exp(-r^2t^2)|\phi_{k'}\rangle \tag{A.45}$$

$$=\frac{2}{\sqrt{\pi}}\int_0^\infty dt\left(\frac{(2L+1)!!}{4\pi}\left(\frac{(2\pi)^{N-1}}{\text{detB}}\right)^{\frac{3}{2}}\left(\frac{c}{c+2t^2}\right)^{\frac{3}{2}}\left(\rho-\frac{\gamma\gamma'}{c}\frac{2t^2}{c+2t^2}\right)^L\right) \tag{A.46}$$

$$=\frac{2}{\sqrt{\pi}}\frac{(2L+1)!!}{4\pi}\left(\frac{(2\pi)^{N-1}}{\text{detB}}\right)^{\frac{3}{2}}\int_0^\infty dt\left(\frac{c}{c+2t^2}\right)^{\frac{3}{2}}\sum_{l=0}^{L}{}_LC_l\;\rho^l\left(-\frac{\gamma\gamma'}{c}\frac{2t^2}{c+2t^2}\right)^{L-l} \tag{A.47}$$

$$=\frac{2}{\sqrt{\pi}}\frac{(2L+1)!!}{4\pi}\left(\frac{(2\pi)^{N-1}}{\text{detB}}\right)^{\frac{3}{2}}\sum_{l=0}^{L}{}_LC_l\;\rho^l\left(-\frac{\gamma\gamma'}{c}\right)^{L-l}\int_0^\infty dt\left(\frac{c}{c+2t^2}\right)^{\frac{3}{2}}\left(\frac{2t^2}{c+2t^2}\right)^{L-l} \tag{A.48}$$

$$=\frac{2}{\sqrt{\pi}}\frac{(2L+1)!!}{4\pi}\left(\frac{(2\pi)^{N-1}}{\text{detB}}\right)^{\frac{3}{2}}\sum_{l=0}^{L}{}_LC_l\;\rho^l\left(-\frac{\gamma\gamma'}{c}\right)^{L-l}\underbrace{c^{\frac{3}{2}}c^{-L+l-\frac{3}{2}}c^{L-l}}_{=1}\int_0^\infty dt\frac{\left(\frac{2}{c}t^2\right)^{L-l}}{\left(\frac{2}{c}t^2+1\right)^{L-l+\frac{3}{2}}} \tag{A.49}$$

Let $u=\frac{2}{c}t^2$, then

$$\langle\phi_k|\frac{1}{r}|\phi_{k'}\rangle \tag{A.50}$$

$$=\frac{2}{\sqrt{\pi}}\frac{(2L+1)!!}{4\pi}\left(\frac{(2\pi)^{N-1}}{\text{detB}}\right)^{\frac{3}{2}}\sum_{l=0}^{L}{}_LC_l\;\rho^l\left(-\frac{\gamma\gamma'}{c}\right)^{L-l}\int_0^\infty dt\frac{\left(\frac{2}{c}t^2\right)^{L-l}}{\left(\frac{c}{2}t^2+1\right)^{L-l+\frac{3}{2}}} \tag{A.51}$$

$$=\frac{2}{\sqrt{\pi}}\frac{(2L+1)!!}{4\pi}\left(\frac{(2\pi)^{N-1}}{\text{detB}}\right)^{\frac{3}{2}}\sum_{l=0}^{L}{}_LC_l\;\rho^l\left(-\frac{\gamma\gamma'}{c}\right)^{L-l}\int_0^\infty du\frac{c}{4}\left(\frac{2}{c}\right)^{\frac{1}{2}}\frac{u^{L-l-\frac{1}{2}}}{(1+u)^{L-l+\frac{3}{2}}} \tag{A.52}$$

$$=\frac{2}{\sqrt{\pi}}\frac{(2L+1)!!}{4\pi}\left(\frac{(2\pi)^{N-1}}{\text{detB}}\right)^{\frac{3}{2}}\sum_{l=0}^{L}{}_LC_l\;\rho^l\left(-\frac{\gamma\gamma'}{c}\right)^{L-l}c^{\frac{1}{2}}2^{-\frac{3}{2}}\int_0^\infty du\frac{u^{(L-l+\frac{1}{2})-1}}{(1+u)^{(L-l+\frac{1}{2})+1}} \tag{A.53}$$

Here the definition of the Beta function (1st Euler) can be used,

$$B(p,q)=\int_0^\infty\frac{t^{p-1}}{(1+t)^{p+q}}dt. \tag{A.54}$$

Finally

$$\langle\phi_k|\frac{1}{r}|\phi_{k'}\rangle \tag{A.55}$$

$$=\frac{2}{\sqrt{\pi}}\frac{(2L+1)!!}{4\pi}\left(\frac{(2\pi)^{N-1}}{\text{detB}}\right)^{\frac{3}{2}}\sum_{l=0}^{L}{}_LC_l\;\rho^l\left(-\frac{\gamma\gamma'}{c}\right)^{L-l}c^{\frac{1}{2}}2^{-\frac{3}{2}}B(L-l+\frac{1}{2},1) \tag{A.56}$$

$$=\frac{2}{\sqrt{\pi}}\frac{(2L+1)!!}{4\pi}\left(\frac{(2\pi)^{N-1}}{\text{detB}}\right)^{\frac{3}{2}}\sum_{l=0}^{L}{}_LC_l\;\rho^l\left(-\frac{\gamma\gamma'}{c}\right)^{L-l}c^{\frac{1}{2}}2^{-\frac{3}{2}}\frac{\Gamma(L-l+\frac{1}{2})\Gamma(1)}{\Gamma(L-l+\frac{3}{2})} \tag{A.57}$$

$$=\frac{2}{\sqrt{\pi}}\frac{(2L+1)!!}{4\pi}\left(\frac{(2\pi)^{N-1}}{\text{detB}}\right)^{\frac{3}{2}}\sum_{l=0}^{L}{}_LC_l\;\rho^l\left(-\frac{\gamma\gamma'}{c}\right)^{L-l}c^{\frac{1}{2}}2^{-\frac{3}{2}}\frac{\Gamma(L-l+\frac{1}{2})}{\Gamma(L-l+\frac{3}{2})} \tag{A.58}$$

By using

$$\Gamma\left(n+\frac{1}{2}\right)=\frac{(2n-1)!!}{2^n}\sqrt{\pi} \tag{A.59}$$

The matrix element can be reduced,

$$\langle\phi_k|\frac{1}{r}|\phi_{k'}\rangle=\frac{2}{\sqrt{\pi}}\frac{(2L+1)!!}{4\pi}\left(\frac{(2\pi)^{N-1}}{\mathrm{detB}}\right)^{\frac{3}{2}}\sum_{l=0}^{L}{}_LC_l\ \rho^l\left(-\frac{\gamma\gamma'}{c}\right)^{L-l}\frac{c^{\frac{1}{2}}2^{-\frac{1}{2}}}{2(L-l)+1} \tag{A.60}$$

Error function type Coulomb potential

$$\langle\phi_k|\frac{1}{r}\mathrm{erf}(\kappa r)|\phi_{k'}\rangle \tag{A.61}$$

$$=\frac{2\kappa}{\sqrt{\pi}}\int_0^1 dt\,\langle\phi_k|\exp(-\kappa^2r^2t^2)|\phi_{k'}\rangle \tag{A.62}$$

$$=\frac{2\kappa}{\sqrt{\pi}}\int_0^1 dt\left(\frac{(2L+1)!!}{4\pi}\left(\frac{(2\pi)^{N-1}}{\mathrm{detB}}\right)^{\frac{3}{2}}\left(\frac{c}{c+2\kappa^2t^2}\right)^{\frac{3}{2}}\left(\rho-\frac{\gamma\gamma'}{c}\frac{2\kappa^2t^2}{c+2\kappa^2t^2}\right)^L\right) \tag{A.63}$$

$$=\frac{2\kappa}{\sqrt{\pi}}\frac{(2L+1)!!}{4\pi}\left(\frac{(2\pi)^{N-1}}{\mathrm{detB}}\right)^{\frac{3}{2}}\int_0^1 dt\left(\frac{1}{1+\frac{2\kappa^2}{c}t^2}\right)^{\frac{3}{2}}\sum_{l=0}^{L}{}_LC_l\ \rho^l\left(-\frac{\gamma\gamma'}{c}\frac{\frac{2\kappa^2}{c}t^2}{1+\frac{2\kappa^2}{c}t^2}\right)^{L-l} \tag{A.64}$$

$$=\frac{2\kappa}{\sqrt{\pi}}\frac{(2L+1)!!}{4\pi}\left(\frac{(2\pi)^{N-1}}{\mathrm{detB}}\right)^{\frac{3}{2}}\sum_{l=0}^{L}{}_LC_l\ \rho^l\left(-\frac{\gamma\gamma'}{c}\right)^{L-l}\underline{\int_0^1 dt\left(\frac{1}{1+\frac{2\kappa^2}{c}t^2}\right)^{\frac{3}{2}}\left(\frac{\frac{2\kappa^2}{c}t^2}{1+\frac{2\kappa^2}{c}t^2}\right)^{L-l}} \tag{A.65}$$

For the under-lined integration, let $u=\frac{2\kappa^2}{c}t^2$

$$\int_0^1 dt\left(\frac{1}{1+\frac{2\kappa^2}{c}t^2}\right)^{\frac{3}{2}}\left(\frac{\frac{2\kappa^2}{c}t^2}{1+\frac{2\kappa^2}{c}t^2}\right)^{L-l} \tag{A.66}$$

$$=\frac{c}{4\kappa^2}\left(\frac{2\kappa^2}{c}\right)^{\frac{1}{2}}\int_0^{\frac{2\kappa^2}{c}}du\left(\frac{1}{1+u}\right)^{L-l+\frac{3}{2}}u^{L-l-\frac{1}{2}} \tag{A.67}$$

Replacing the u as $u=\frac{1}{\tilde{u}}$ then

$$\frac{c}{4\kappa^2}\left(\frac{2\kappa^2}{c}\right)^{\frac{1}{2}}\int_0^{\frac{2\kappa^2}{c}}du\left(\frac{1}{1+u}\right)^{L-l+\frac{3}{2}}u^{L-l-\frac{1}{2}} \tag{A.68}$$

$$=\frac{c}{4\kappa^2}\left(\frac{2\kappa^2}{c}\right)^{\frac{1}{2}}\int_{\frac{c}{2\kappa^2}}^{\infty}d\tilde{u}\left(\frac{1}{1+\tilde{u}}\right)^{L-l+\frac{3}{2}} \tag{A.69}$$

$$=\frac{c}{4\kappa^2}\left(\frac{2\kappa^2}{c}\right)^{\frac{1}{2}}\frac{1}{L-l+\frac{1}{2}}\left(\frac{2\kappa^2}{c+2\kappa^2}\right)^{L-l+\frac{1}{2}} \tag{A.70}$$

Finally the matirx element is

$$\langle\phi_k|\frac{1}{r}\mathrm{erf}(\kappa r)|\phi_{k'}\rangle \tag{A.71}$$

$$=\frac{2\kappa}{\sqrt{\pi}}\frac{(2L+1)!!}{4\pi}\left(\frac{(2\pi)^{N-1}}{\mathrm{detB}}\right)^{\frac{3}{2}}\sum_{l=0}^{L}{}_LC_l\ \rho^l\left(-\frac{\gamma\gamma'}{c}\right)^{L-l}\frac{c}{4\kappa^2}\left(\frac{2\kappa^2}{c}\right)^{\frac{1}{2}}\frac{1}{L-l+\frac{1}{2}}\left(\frac{2\kappa^2}{c+2\kappa^2}\right)^{L-l+\frac{1}{2}} \tag{A.72}$$

$$=\frac{1}{\sqrt{\pi}}\left(\frac{c}{2}\right)^{\frac{1}{2}}\frac{(2L+1)!!}{4\pi}\left(\frac{(2\pi)^{N-1}}{\mathrm{detB}}\right)^{\frac{3}{2}}\sum_{l=0}^{L}{}_LC_l\ \rho^l\left(-\frac{\gamma\gamma'}{c}\right)^{L-l}\frac{1}{L-l+\frac{1}{2}}\left(\frac{2\kappa^2}{c+2\kappa^2}\right)^{L-l+\frac{1}{2}} \tag{A.73}$$

In the case of the totalangular momentum 0,

$$\langle\phi_k|\frac{1}{r}|\phi_{k'}\rangle=\langle\phi_k|\phi_{k'}\rangle\,\frac{2}{\sqrt{\pi}}\sqrt{\frac{c}{2}} \tag{A.74}$$

$$\langle\phi_k|\frac{1}{r}\mathrm{erf}(\kappa r)|\phi_{k'}\rangle=2\kappa\,\langle\phi_k|\phi_{k'}\rangle\sqrt{\frac{c/2}{\pi(\kappa^2+c/2)}} \tag{A.75}$$

A.3.4 Yukawa potential

The matrix element of the Yukawa potential is obtained by using the relation

$$\frac{1}{r}\exp(-\kappa r)=\frac{2}{\sqrt{\pi}}\int_0^\infty dt\exp\left(-r^2t^2-\frac{\kappa^2}{4t^2}\right) \tag{A.76}$$

Finally

$$\langle\phi_k|\frac{1}{r}\exp(-\kappa r)|\phi_l\rangle \tag{A.77}$$

$$=\sqrt{\frac{2c}{\pi}}\int_0^1 dt\exp\left(-\frac{\kappa^2}{2c}\frac{1-u^2}{u^2}\right)\langle\phi_k|\phi_l\rangle\,|_{\rho\to\rho-cu^2\gamma\gamma'}. \tag{A.78}$$

The integration is implemented with Gauss quadrature. The Yukawa potential is the same form as the point Coulomb potential with screening effect $\exp(-\kappa r)$.

A.3.5 ℓ^2-dependent potential of the Gaussian radial form

This subsection calculate the matrix element of the ℓ^2-dependent potential of the Gaussian radial form,

$$V(r)=\exp\left\{-\frac{1}{2}c'\tilde{\boldsymbol{x}}\boldsymbol{w}\tilde{\boldsymbol{w}}\boldsymbol{x}\right\}\ell^2, \tag{A.79}$$

where $\tilde{\boldsymbol{w}}\boldsymbol{x}=\boldsymbol{r}_i-\boldsymbol{r}_j=\boldsymbol{y}_1$ and $\boldsymbol{\ell}=\boldsymbol{y}_1\times(-i\hbar)\partial/\partial\boldsymbol{y}_1$. According to the ref. [65], the matrix element of the generating function $g(\boldsymbol{s};A,\boldsymbol{x})$ is calculated,

$$\langle g(\boldsymbol{s}';A',\boldsymbol{x})|\exp\left\{-\frac{1}{2}c'\tilde{\boldsymbol{x}}\boldsymbol{w}\tilde{\boldsymbol{w}}\boldsymbol{x}\right\}\ell^2|g(\boldsymbol{s};A,\boldsymbol{x})\rangle \tag{A.80}$$

$$=\hbar^2\,\langle g(\boldsymbol{s}';A',\boldsymbol{x})|\exp\left\{-\frac{1}{2}c'\tilde{\boldsymbol{x}}\boldsymbol{w}\tilde{\boldsymbol{w}}\boldsymbol{x}\right\}\mathcal{L}^2|g(\boldsymbol{s};A,\boldsymbol{x})\rangle \tag{A.81}$$

with

$$\mathcal{L}^2=(\tilde{\boldsymbol{w}}\boldsymbol{x}\times(\tilde{\zeta}\boldsymbol{s}'-\tilde{\zeta}A'\boldsymbol{x}))\cdot(\tilde{\boldsymbol{w}}\boldsymbol{x}\times(\tilde{\zeta}\boldsymbol{s}-\tilde{\zeta}A\boldsymbol{x})). \tag{A.82}$$

I consider only $J^\pi = 0^+$ states and $\boldsymbol{s}$ can be $\mathbf{0}$.

$$\mathcal{L}^2 = (\tilde{\boldsymbol{w}}\boldsymbol{x} \times (-\tilde{\zeta}A'\boldsymbol{x})) \cdot (\tilde{\boldsymbol{w}}\boldsymbol{x} \times (-\tilde{\zeta}A\boldsymbol{x})) \tag{A.83}$$

$$= \tilde{\boldsymbol{x}}\boldsymbol{w}\tilde{\boldsymbol{w}}\boldsymbol{x} \cdot \tilde{\boldsymbol{x}}A'\zeta\tilde{\zeta}A\boldsymbol{x} - \tilde{\boldsymbol{x}}A'\zeta\tilde{\boldsymbol{w}}\boldsymbol{x} \cdot \tilde{\boldsymbol{x}}A\zeta\tilde{\boldsymbol{w}}\boldsymbol{x} \tag{A.84}$$

The matrix element of squared quadratic form with Gaussian radial form $\exp\left\{-\frac{1}{2}c'\tilde{\boldsymbol{x}}\boldsymbol{w}\tilde{\boldsymbol{w}}\boldsymbol{x}\right\}\boldsymbol{x}Q_1\boldsymbol{x}\cdot\boldsymbol{x}Q_2\boldsymbol{x}$ is needed.

$$\tilde{\boldsymbol{x}}Q_1\boldsymbol{x} \cdot \tilde{\boldsymbol{x}}Q_2\boldsymbol{x} = \sum_{ijkl}^{N-1} Q_{1,ij}Q_{2,kl}(\boldsymbol{x}_i \cdot \boldsymbol{x}_j) \cdot (\boldsymbol{x}_k \cdot \boldsymbol{x}_l) \tag{A.85}$$

The integration can be carried out with the integration formula

$$\int \exp\left(-\frac{1}{2}\tilde{\boldsymbol{x}}A\boldsymbol{x} + \tilde{\boldsymbol{s}}\boldsymbol{x}\right) d\boldsymbol{x} = \left(\frac{(2\pi)^N}{\det A}\right)^{3/2} \exp\left(\frac{1}{2}\tilde{\boldsymbol{s}}A^{-1}\boldsymbol{s}\right). \tag{A.86}$$

See the SVM book for details. By differentiating both sides with respect to the mth component of the vector $\boldsymbol{s}_i$, $(\boldsymbol{s}_i)_m$, I obtain

$$\int (\boldsymbol{x}_i)_m \exp\left(-\frac{1}{2}\tilde{\boldsymbol{x}}A\boldsymbol{x} + \tilde{\boldsymbol{s}}\boldsymbol{x}\right) d\boldsymbol{x} = ((A^{-1}\boldsymbol{s})_i)_m \left(\frac{(2\pi)^N}{\det A}\right)^{3/2} \exp\left(\frac{1}{2}\tilde{\boldsymbol{s}}A^{-1}\boldsymbol{s}\right) \tag{A.87}$$

In the same way, by further differentiating with respect to the $(\boldsymbol{s}_j)_n$ and so on,

$$\int (\boldsymbol{x}_i)_m(\boldsymbol{x}_j)_n \exp\left(-\frac{1}{2}\tilde{\boldsymbol{x}}A\boldsymbol{x} + \tilde{\boldsymbol{s}}\boldsymbol{x}\right) d\boldsymbol{x} \tag{A.88}$$

$$= \left\{(A^{-1})_{ij}\delta_{mn} + ((A^{-1}\boldsymbol{s})_i)_m((A^{-1}\boldsymbol{s})_j)_n\right\} \left(\frac{(2\pi)^N}{\det A}\right)^{3/2} \exp\left(\frac{1}{2}\tilde{\boldsymbol{s}}A^{-1}\boldsymbol{s}\right) \tag{A.89}$$

$$\int (\boldsymbol{x}_i)_m(\boldsymbol{x}_j)_n(\boldsymbol{x}_k)_l \exp\left(-\frac{1}{2}\tilde{\boldsymbol{x}}A\boldsymbol{x} + \tilde{\boldsymbol{s}}\boldsymbol{x}\right) d\boldsymbol{x} \tag{A.90}$$

$$= \left\{(A^{-1})_{ik}\delta_{ml}((A^{-1}\boldsymbol{s})_j)_n + ((A^{-1}\boldsymbol{s})_i)_m(A^{-1})_{jk}\delta_{nl}\right\} \left(\frac{(2\pi)^N}{\det A}\right)^{3/2} \exp\left(\frac{1}{2}\tilde{\boldsymbol{s}}A^{-1}\boldsymbol{s}\right) \tag{A.91}$$

$$+ \left\{(A^{-1})_{ij}\delta_{mn} + ((A^{-1}\boldsymbol{s})_i)_m((A^{-1}\boldsymbol{s})_j)_n\right\} ((A^{-1}\boldsymbol{s})_k)_l \left(\frac{(2\pi)^N}{\det A}\right)^{3/2} \exp\left(\frac{1}{2}\tilde{\boldsymbol{s}}A^{-1}\boldsymbol{s}\right) \tag{A.92}$$

$$\int (\boldsymbol{x}_i)_m (\boldsymbol{x}_j)_n (\boldsymbol{x}_k)_l (\boldsymbol{x}_p)_q \exp\left(-\frac{1}{2}\tilde{\boldsymbol{x}} A \boldsymbol{x} + \tilde{\boldsymbol{s}}\boldsymbol{x}\right) d\boldsymbol{x} \tag{A.93}$$

$$= \left\{(A^{-1})_{ik}\delta_{ml}(A^{-1})_{jp}\delta_{nq} + (A^{-1})_{ip}\delta_{mq}(A^{-1})_{jk}\delta_{nl}\right\} \left(\frac{(2\pi)^N}{\det A}\right)^{3/2} \exp\left(\frac{1}{2}\tilde{\boldsymbol{s}} A^{-1} \boldsymbol{s}\right) \tag{A.94}$$

$$+ \left\{(A^{-1})_{ik}\delta_{ml}((A^{-1}\boldsymbol{s})_j)_n + ((A^{-1}\boldsymbol{s})_i)_m (A^{-1})_{jk}\delta_{nl}\right\} ((A^{-1}\boldsymbol{s})_p)_q \left(\frac{(2\pi)^N}{\det A}\right)^{3/2} \exp\left(\frac{1}{2}\tilde{\boldsymbol{s}} A^{-1} \boldsymbol{s}\right) \tag{A.95}$$

$$+ \left\{(A^{-1})_{ip}\delta_{mq}((A^{-1}\boldsymbol{s})_j)_n + ((A^{-1}\boldsymbol{s})_i)_m (A^{-1})_{jp}\delta_{nq}\right\} ((A^{-1}\boldsymbol{s})_k)_l \left(\frac{(2\pi)^N}{\det A}\right)^{3/2} \exp\left(\frac{1}{2}\tilde{\boldsymbol{s}} A^{-1} \boldsymbol{s}\right) \tag{A.96}$$

$$+ \left\{(A^{-1})_{ij}\delta_{mn} + ((A^{-1}\boldsymbol{s})_i)_m ((A^{-1}\boldsymbol{s})_j)_n\right\} (A^{-1})_{kp}\delta_{lq} \left(\frac{(2\pi)^N}{\det A}\right)^{3/2} \exp\left(\frac{1}{2}\tilde{\boldsymbol{s}} A^{-1} \boldsymbol{s}\right) \tag{A.97}$$

$$+ \left\{(A^{-1})_{ij}\delta_{mn} + ((A^{-1}\boldsymbol{s})_i)_m ((A^{-1}\boldsymbol{s})_j)_n\right\} ((A^{-1}\boldsymbol{s})_k)_l ((A^{-1}\boldsymbol{s})_p)_q \left(\frac{(2\pi)^N}{\det A}\right)^{3/2} \exp\left(\frac{1}{2}\tilde{\boldsymbol{s}} A^{-1} \boldsymbol{s}\right) \tag{A.98}$$

Setting $\boldsymbol{s} = \boldsymbol{0}$ and $m = n$, $l = q$.

$$\int (\boldsymbol{x}_i)_m (\boldsymbol{x}_j)_n (\boldsymbol{x}_k)_l (\boldsymbol{x}_p)_q \exp\left(-\frac{1}{2}\tilde{\boldsymbol{x}} A \boldsymbol{x}\right) d\boldsymbol{x} \tag{A.99}$$

$$= \left\{(A^{-1})_{ik}\delta_{ml}(A^{-1})_{jp}\delta_{nq} + (A^{-1})_{ip}\delta_{mq}(A^{-1})_{jk}\delta_{nl}\right\} \left(\frac{(2\pi)^N}{\det A}\right)^{3/2} \tag{A.100}$$

$$+ (A^{-1})_{ij}\delta_{mn}(A^{-1})_{kp}\delta_{lq} \left(\frac{(2\pi)^N}{\det A}\right)^{3/2} \tag{A.101}$$

$$\int (\boldsymbol{x}_i)_m (\boldsymbol{x}_j)_m (\boldsymbol{x}_k)_l (\boldsymbol{x}_p)_l \exp\left(-\frac{1}{2}\tilde{\boldsymbol{x}} A \boldsymbol{x}\right) d\boldsymbol{x} \tag{A.102}$$

$$= \left\{(A^{-1})_{ik}\delta_{ml}(A^{-1})_{jp}\delta_{ml} + (A^{-1})_{ip}\delta_{ml}(A^{-1})_{jk}\delta_{ml}\right\} \left(\frac{(2\pi)^N}{\det A}\right)^{3/2} \tag{A.103}$$

$$+ (A^{-1})_{ij}\delta_{mm}(A^{-1})_{kp}\delta_{ll} \left(\frac{(2\pi)^N}{\det A}\right)^{3/2} \tag{A.104}$$

Finally I obtain

$$\int (\boldsymbol{x}_i \cdot \boldsymbol{x}_j) \cdot (\boldsymbol{x}_k \cdot \boldsymbol{x}_p) \exp\left(-\frac{1}{2}\tilde{\boldsymbol{x}} A \boldsymbol{x}\right) d\boldsymbol{x} \tag{A.105}$$

$$= \sum_{ml} \left\{(A^{-1})_{ik}(A^{-1})_{jp}\delta_{ml} + (A^{-1})_{ip}(A^{-1})_{jk}\delta_{ml} + (A^{-1})_{ij}(A^{-1})_{kp}\right\} \left(\frac{(2\pi)^N}{\det A}\right)^{3/2} \tag{A.106}$$

$$= \left\{3(A^{-1})_{ik}(A^{-1})_{jp} + 3(A^{-1})_{ip}(A^{-1})_{jk} + 9(A^{-1})_{ij}(A^{-1})_{kp}\right\} \left(\frac{(2\pi)^N}{\det A}\right)^{3/2} \tag{A.107}$$

Returning to the matrix element of ℓ^2-dependent potential, we can calculate it with the

above formula,

$$\left\langle \exp\left(-\frac{1}{2}\tilde{\boldsymbol{x}}A'\boldsymbol{x}\right)\mathcal{Y}_0 \middle| \exp\left\{-\frac{1}{2}c'\tilde{\boldsymbol{x}}\boldsymbol{w}\tilde{\boldsymbol{w}}\boldsymbol{x}\right\}\mathcal{L}^2 \middle| \exp\left(-\frac{1}{2}\tilde{\boldsymbol{x}}A\boldsymbol{x}\right)\mathcal{Y}_0 \right\rangle \tag{A.108}$$

$$=\sum_{a=1}^{2}\left\langle \exp\left(-\frac{1}{2}\tilde{\boldsymbol{x}}A'\boldsymbol{x}\right)\mathcal{Y}_0 \middle| \exp\left\{-\frac{1}{2}c'\tilde{\boldsymbol{x}}\boldsymbol{w}\tilde{\boldsymbol{w}}\boldsymbol{x}\right\}\tilde{\boldsymbol{x}}Q_{a,1}\boldsymbol{x}\cdot\tilde{\boldsymbol{x}}Q_{a,2}\boldsymbol{x} \middle| \exp\left(-\frac{1}{2}\tilde{\boldsymbol{x}}A\boldsymbol{x}\right)\mathcal{Y}_0 \right\rangle \tag{A.109}$$

$$=\sum_{a=1}^{2}\sum_{ijkl}^{N-1}Q_{a,1,ij}Q_{a,2,kl}\left\langle \exp\left(-\frac{1}{2}\tilde{\boldsymbol{x}}A'\boldsymbol{x}\right)\mathcal{Y}_0 \middle| \exp\left\{-\frac{1}{2}c'\tilde{\boldsymbol{x}}\boldsymbol{w}\tilde{\boldsymbol{w}}\boldsymbol{x}\right\}(\boldsymbol{x}_i\cdot\boldsymbol{x}_j)\cdot(\boldsymbol{x}_k\cdot\boldsymbol{x}_l) \middle| \exp\left(-\frac{1}{2}\tilde{\boldsymbol{x}}A\boldsymbol{x}\right)\mathcal{Y}_0 \right\rangle \tag{A.110}$$

$$=\sum_{a=1}^{2}\sum_{ijkl}^{N-1}Q_{a,1,ij}Q_{a,2,kl}\frac{1}{4\pi}\int d\boldsymbol{x}(\boldsymbol{x}_i\cdot\boldsymbol{x}_j)\cdot(\boldsymbol{x}_k\cdot\boldsymbol{x}_l)\exp\left(-\frac{1}{2}\tilde{\boldsymbol{x}}(\underbrace{A'+A+c'\boldsymbol{w}\tilde{\boldsymbol{w}}}_{=B})\boldsymbol{x}\right) \tag{A.111}$$

$$=\sum_{a=1}^{2}\sum_{ijkl}^{N-1}Q_{a,1,ij}Q_{a,2,kl}\frac{1}{4\pi}\left\{3(B^{-1})_{ik}(B^{-1})_{jp}+3(B^{-1})_{ip}(B^{-1})_{jk}+9(B^{-1})_{ij}(B^{-1})_{kp}\right\}\left(\frac{(2\pi)^N}{\det B}\right)^{3/2} \tag{A.112}$$

A.3.6 Gaussian over the r^2 potential

This subsection calculates the matrix element of the Gaussian over the r^2,

$$V(r)=\frac{\exp(-\mu r^2)}{r^2}. \tag{A.113}$$

Using the relation that $\dfrac{1}{r^2}=\displaystyle\int_0^\infty dt\exp(-tr^2)$, the desired matrix element become the integration of the matrix element of the Gaussian potential,

$$\left\langle \phi_k \middle| \frac{\exp(-\mu r^2)}{r^2} \middle| \phi_{k'} \right\rangle \tag{A.114}$$

$$=\left\langle \phi_k \middle| \int_0^\infty dt\exp(-(\mu+t)r^2) \middle| \phi_{k'} \right\rangle \tag{A.115}$$

$$=\int_0^\infty dt\,\langle\phi_k|\exp(-\beta(t)r^2)|\phi_{k'}\rangle \tag{A.116}$$

$$=\int_0^\infty dt\frac{(2L+1)!!}{4\pi}\left(\frac{(2\pi)^{N-1}}{\mathrm{detB}}\right)^{\frac{3}{2}}\left(\frac{c}{c+2\beta(t)}\right)^{\frac{3}{2}}\left(\rho-\frac{\gamma\gamma'}{c}\frac{2\beta(t)}{c+2\beta(t)}\right)^L \tag{A.117}$$

$$=\frac{(2L+1)!!}{4\pi}\left(\frac{(2\pi)^{N-1}}{\mathrm{detB}}\right)^{\frac{3}{2}}\int_0^\infty dt\left(\frac{c}{c+2\beta(t)}\right)^{\frac{3}{2}}\sum_{l=0}^{L}{}_LC_l\rho^l\left(-\frac{\gamma\gamma'}{c}\right)^{L-l}\left(\frac{2\beta(t)}{c+2\beta(t)}\right)^{L-l} \tag{A.118}$$

$$=\frac{(2L+1)!!}{4\pi}\left(\frac{(2\pi)^{N-1}}{\mathrm{detB}}\right)^{\frac{3}{2}}\sum_{l=0}^{L}{}_LC_l\rho^l\left(-\frac{\gamma\gamma'}{c}\right)^{L-l}\int_0^\infty dt\left(\frac{c}{c+2\beta(t)}\right)^{\frac{3}{2}}\left(\frac{2\beta(t)}{c+2\beta(t)}\right)^{L-l} \tag{A.119}$$

The integration.

$$\int_0^\infty dt \left(\frac{c}{c+2\beta(t)}\right)^{\frac{3}{2}} \left(\frac{2\beta(t)}{c+2\beta(t)}\right)^{L-l} \tag{A.120}$$

$$= \int_0^\infty dt \left(\frac{c/2}{c/2+\mu+t}\right)^{\frac{3}{2}} \left(\frac{\mu+t}{c/2+\mu+t}\right)^{L-l} \tag{A.121}$$

$$= \int_{\mu+c/2}^\infty dt' \left(\frac{c/2}{t'}\right)^{\frac{3}{2}} \left(\frac{t'-c/2}{t'}\right)^{L-l} \tag{A.122}$$

$$= \int_{\mu+c/2}^\infty dt' \left(\frac{c}{2}\right)^{3/2} t'^{-3/2} \sum_{n=0}^{L-l} {}_{L-l}C_n \left(-\frac{c/2}{t'}\right)^{L-l-n} \tag{A.123}$$

$$= \sum_{n=0}^{L-l} {}_{L-l}C_n \left(\frac{c}{2}\right)^{L-l-n+3/2} (-1)^{L-l-n} \int_{\mu+c/2}^\infty dt' t'^{-L+l+n-3/2} \tag{A.124}$$

$$= \sum_{n=0}^{L-l} {}_{L-l}C_n \left(\frac{c}{2}\right)^{L-l-n+3/2} (-1)^{L-l-n} \frac{\left(\mu+\frac{c}{2}\right)^{-L+l+n-1/2}}{L-l-n+\frac{1}{2}} \tag{A.125}$$

Finally I obtain

$$\left\langle \phi_k \left| \frac{\exp(-\mu r^2)}{r^2} \right| \phi_{k'} \right\rangle \tag{A.126}$$

$$= \frac{(2L+1)!!}{4\pi} \left(\frac{(2\pi)^{N-1}}{\mathrm{detB}}\right)^{\frac{3}{2}} \sum_{l=0}^{L} {}_LC_l \rho^l \left(-\frac{\gamma\gamma'}{c}\right)^{L-l} \sum_{n=0}^{L-l} {}_{L-l}C_n \left(\frac{c}{2}\right)^{L-l-n+3/2} (-1)^{L-l-n} \frac{\left(\mu+\frac{c}{2}\right)^{-L+l+n-1/2}}{L-l-n+\frac{1}{2}} \tag{A.127}$$

$$= \frac{(2L+1)!!}{4\pi} \left(\frac{(2\pi)^{N-1}}{\mathrm{detB}}\right)^{\frac{3}{2}} \sum_{l=0}^{L} \sum_{n=0}^{L-l} {}_LC_l \; {}_{L-l}C_n \rho^l \left(\frac{\gamma\gamma'}{c}\right)^{L-l} (-1)^n \left(\frac{c}{2}\right)^{L-l-n+3/2} \frac{\left(\mu+\frac{c}{2}\right)^{-L+l+n-1/2}}{L-l-n+\frac{1}{2}} \tag{A.128}$$

Acknowledgment

I would like to give thanks to Prof. Horiuchi who provided carefully considered feedback and valuable comments. I would also like to express my gratitude to my family, colleagues, and personal involves for their moral support and warm encouragements.

Bibliography

[1] B. Frois and C. Papanicolas, Ann. Rev. Nucl. Part. Sci. **37**, 133 (1987).

[2] J. H. Kelley, D. R. Tilley, H. R. Weller, and G. M. Hale, Nucl. Phys. A **541**, 1 (1992).

[3] K. Ikeda, N. Takigawa, and H. Horiuchi, Prog. Theor. Phys. Supp. Extra Num. 464 (1968).

[4] S. Typel, Phys. Rev. C **89**, 064321 (2014).

[5] J. Tanaka, Z. H. Yang, S. Typel, S. Adachi, S. Bai, P. van Beek, D. Beaumel, Y. Fujikawa, J. Han, S. Heil *et al.*, Science **371**, 260 (2021).

[6] A. W. Steiner, J. M. Lattimer, and E. F. Brown, Astrophys. J. Lett. **765**, L5 (2013).

[7] F. Hoyle, Astrophys. J. Suppl. Ser. **1**, 12 (1954).

[8] P. Navrátil, J. P. Vary, and B. R. Barrett, Phys. Rev. Lett. **84**, 5728 (2000).

[9] T. Otsuka, T. Abe, T. Yoshida, Y. Tsunoda, N. Shimizu, N. Itagaki, Y. Utsuno, J. Vary, P. Maris, and H. Ueno, Nat. Commun. **13**, 2234 (2022).

[10] B. Baymen ahnd A. Bohr, Nucl. Phys. **9**, 596 (1958).

[11] T. Yamada *et al.*, Prog. Theor. Phys. **120**, 1139 (2008).

[12] H. Morinaga, Phys. Rev. **101**, 254 (1956).

[13] H. Morinaga, Phys. Lett. **21**, 78 (1966).

[14] J. A. Wheeler, Phys. Rev. **52**, 1083 (1937).

[15] H. Margenau, Phys. Rev. **59**, 37 (1941).

[16] S. Saito, Prog. Theor. Phys. **40**, 893 (1968).

[17] S. Saito, Prog. Theor. Phys. **41**, 705 (1969).

[18] S. Saito, Prog. Theor. Phys. **62**, 11 (1977).

[19] E. Uegaki, S. Okabe, Y. Abe, and H. Tanaka, Prog. Theor. Phys. **57**, 1262 (1977).

[20] E. Uegaki, Y. Abe, S. Okabe, and H. Tanaka, *ibid.* **62**, 1621 (1979).

[21] M. Kamimura, Nucl. Phys. A **351**, 456 (1981).

[22] H. Horiuchi, Prog. Theor. Phys. **51**, 1226 (1974).

[23] H. Horiuchi, Prog. Theor. Phys. **53**, 447 (1975).

[24] G. Röpke, A. Schnell, P. Schuck, and P. Nozières, Phys. Rev. Lett. **80**, 3177 (1998).

[25] M. Beyer, S. A. Sofianos, C. Kuhrts, G. Röpke, and P. Schuck, Phys. Lett. B **488**, 247 (2000).

[26] A. Tohsaki, H. Horiuchi, P. Schuck, and G. Röpke, Phys. Rev. Lett. **87**, 192501 (2001).

[27] Y. Funaki, H. Horiuchi, A. Tohsaki, P. Schuck, and G. Röpke, Prog. Theor. Phys. **108**, 297 (2002).

[28] Y. Funaki, H. Horiuchi and A. Tohsaki, Prog. Part. Nucl. Phys. **82**, 78 (2015).

[29] R. Bijker and F. Iachello, Phys. Rev. C **61**, 067305 (2000).

[30] R. Bijker and F. Iachello, Ann. Phys. **298**, 334 (2004).

[31] R. Bijker and F. Iachello, Prog. Part. Nucl. Phys. **110**, 103735 (2020).

[32] L. Fortunato, Phys. Rev. C **99**, 031302(R) (2019).

[33] A. Vitturi, J. Casal, L. Fortunato, and E. G. Lanza, Phys. Rev. C **101**, 014315 (2020).

[34] M. Itoh, H. Akimune, M. Fujiwara, U. Garg, H. Hashimoto, T. Kawabata, K. Kawase, S. Kishi, T. Murakami, K. Nakanishi, Y. Nakatsugawa, B.K. Nayak, S. Okumura, H. Sakaguchi, H. Takeda, S. Terashima, M. Uchida, Y. Yasuda, M. Yosoi, and J. Zenihiro, Nucl. Phys. A **738**, 268 (2004).

[35] M. Freer, H. Fujita, Z. Buthelezi, J. Carter, R. W. Fearick, S. V. Förtsch, R. Neveling, S. M. Perez, P. Papka, F. D. Smit, J. A. Swartz, and I. Usman, Phys. Rev. C **80**, 041303(R) (2009).

[36] M. Itoh, H. Akimune, M. Fujiwara, U. Garg, N. Hashimoto, T. Kawabata, K. Kawase, S. Kishi, T. Murakami, K. Nakanishi, Y. Nakatsugawa, B. K. Nayak, S. Okumura, H. Sakaguchi, H. Takeda, S. Terashima, M. Uchida, Y. Yasuda, M. Yosoi, and J. Zenihiro, Phys. Rev. C **84**, 054308 (2011).

[37] W. R. Zimmerman, M. W. Ahmed, B. Bromberger, S. C. Stave, A. Breskin, V. Dangendorf, Th. Delbar, M. Gai, S. S. Henshaw, J. M. Mueller, C. Sun, K. Tittelmeier, H. R. Weller, and Y. K. Wu, Phys. Rev. Lett. **110**, 152502 (2013).

[38] J. H. Kelley, J. E. Purcell, and C. G. Sheu, Nucl. Phys. A **968**, 71 (2017).

[39] M. Freer *et al.*, Phys. Rev. C **83**, 034314 (2011).

[40] D. J. Marìn-Lámbarri, R. Bijker, M. Freer, M. Gai, Tz. Kokalova, D. J. Parker, and C. Wheldon, Phys. Rev. Lett. **113**, 012502 (2014).

[41] Y. Funaki, Phys. Rev. C **92**, 021302(R) (2015).

[42] C. Angulo et al., Nucl. Phys. A **656**, 3 (1999).

[43] W. H. G. Lewin, J. Van Paradijs, and R. E. Taam, Space Sci. Rev. **62**, 223 (1993).

[44] E. E. Salpeter, Aust. J. Phys. **7**, 373 (1954).

[45] Lai Hnin Phyu, H. Moriya, W. Horiuchi, K. Iida, K. Noda, and M. T. Yamashita, Prog. Theor. Exp. Phys. **2020**, 093D01 (2020).

[46] Lai Hnin Phyu, H. Moriya, W. Horiuchi, K. Iida, K. Noda, and M. T. Yamashita, Few-Body Syst. **62**, 44 (2021).

[47] J. Aguilar and J. M. Combes, Commun. Math. Phys. **22**, 269 (1971).

[48] E. Balslev and J. M. Combes, Commun. Math. Phys. **22**, 280 (1971).

[49] S. Aoyama, T. Myo, K. Kato, and K. Ikeda, Prog. Theor. Phys. **116**, 1 (2006).

[50] V. I. Kukulin and V. M. Krasnopol'sky, J. Phys. A: Math. Gen. **10** L33 (1977).

[51] V. I. Kukulin, V. M. Krasnopol'sky, and M. Miselkhi, Sov. J. Nucl. Phys. **29**, 421 (1979).

[52] S. Aoyama, Phys. Rev. C **68**, 034313 (2003).

[53] H. Matsumura, M. Orabi, Y. Suzuki, and Y. Fujiwara, Nucl. Phys. A **776**, 1 (2006).

[54] V. I. Kukulin, and V. N. Pomenertsev, Ann. Phys. (N. Y.) **111**, 333 (1978).

[55] S. Ohtsubo, Y. Fukushima, M. Kamimura, and E. Hiyama, Prog. Theor. Exp. Phys. **2013**, 073D02 (2013).

[56] H. Moriya, W. Horiuchi, J. Casal, and L. Fortunato, Few-Body Syst. **62**, 46 (2021).

[57] T. Yamada and P. Schuck, Eur. Phys. J. A **26**, 185 (2005).

[58] Y. Funaki, T. Yamada, H. Horiuchi, G. Röpke P. Schuck, and A. Tohsaki, Phys. Rev. Lett. **101**, 082502 (2008).

[59] M. Orabi, Few-Body Syst. **51**, 45 (2011).

[60] S. Ali, A. R. Bodmer, Nucl. Phys. **80**, 99 (1966).

[61] M. Hempel, J. Schaffner-Bielich, S. Typel, and G. Röpke, Phys. Rev. C 84, 055804 (2011).

[62] B. P. Abbott et al. (LIGO Scientific Collaboration and Virgo Collaboration), Phys. Rev. Lett. **119**, 161101 (2017).

[63] M. Oertel, M. Hempel, T. Klähn, and S. Typel, Rev. Mod. Phys. **89**, 015007 (2017).

[64] K. Varga and Y. Suzuki, Phys. Rev. C **52**, 2885 (1995).

[65] Y. Suzuki, W. Horiuchi, M. Orabi, and K. Arai, Few-Body Syst. **42**, 33 (2008).

[66] S. Aoyama *et al.*, Few-Body Syst. **52**, 97 (2012).

[67] Y. Suzuki and K. Varga, *Stochastic Variational Approach to Quantum-Mechanical Few-Body Problems*, Lecture Notes in Physics (Springer, Berlin, 1998), Vol. m54.

[68] S. Ishikawa, Phys. Rev. C **90**, 061604(R) (2014).

[69] M. Chernykh, H. Feldmeier, T. Neff, P. von Neumann-Cosel, and A. Richter, Phys. Rev. Lett. **98**, 032501 (2007).

[70] Y. Kanada-En'yo, Prog. Theor. Phys. **117**, 655 (2007).

[71] R. Smith, M. Gai, M. W. Ahmed, M. Freer, H. O. U. Fynbo, D. Schweitzer, and S. R. Stern, Phys. Rev. C **101**, 021302(R) (2020).

[72] Y. Funaki, A. Tohsaki, H. Horiuchi, P. Schuck, and G. Röpke, Eur. Phys. J. A **24**, 321 (2005).

[73] K. Fukatsu and K. Katō, Prog. Theor. Phys. **87**, 151 (1992).

[74] F. Ajzenberg-Selove, Nucl. Phys. A **506**, 1 (1990).

[75] Y. Funaki, H. Horiuchi, and A. Tohsaki, Prog. Theor. Phys. **115**, 115 (2006).

[76] V. I. Kukulin and V. M. Krasnopol ' sky, J. Phys. A **10**, 33 (1977); V. I. Kukulin and V. M. Krasnopol ' sky, M. Miselkhi, Sov. J. Nucl. Phys. **29**, 421 (1979).

[77] J. Mitory, J. Y. Zhang, and K. Varga, Phys. Rev. Lett. **101**, 123201 (2008).

[78] J. Mitroy, S. Bubin, W. Horiuchi, Y. Suzuki, L. Adamowicz, W. Cencek, K. Szalewicz, J. Komasa, D. Blume, and K. Varga, Rev. Mod. Phys. **85**, 693 (2013).

[79] N. B. Nguyen, F. M. Nunes, and I. J. Thompson, Phys. Rev. C **87**, 054615 (2013).

[80] H. Matsumura and Y. Suzuki, Nucl. Phys. A **739**, 238 (2004).

[81] D. R.Tilley, J. H.Kelley, J. L.Godwin, D. J. Millener, J. E. Purcell, C. G. Sheu, H. R. Weller, Nucl. Phys. **A 745**, 155 (2004).

[82] Y. Suzuki, W. Horiuchi, K. Arai, Nucl. Phys. A **823**, 1 (2009).

[83] E. E. Salpeter, Astrophys. J. **115**, 326 (1952).

[84] E. Nakano, K. Iida, and W. Horiuchi, Phys. Rev. C **102**, 055802 (2020).

[85] G. Röpke, Phys. Rev. C **101**, 064310 (2020).

[86] F. Chevy and C. Mora, Rep. Prog. Phys. **73**, 112401 (2010).

[87] P. Massignan, M. Zaccanti, and G. M. Bruun, Rep. Prog. Phys. **77**, 034401 (2014).

[88] R. Schmidt, M. Knap, D. A. Ivanov, J.-S. You, M. Cetina, and E. Demler, Rep. Prog. Phys. **81**, 024401 (2018).

[89] A. Schirotzek, C.-H. Wu, A. Sommer, and M. W. Zwierlein, Phys. Rev. Lett. **102**, 230402 (2009).

[90] S. Nascimbène, N. Navon, K. J. Jiang, L. Tarruell, M. Teichmann, J. McKeever, F. Chevy, and C. Salomon, Phys. Rev. Lett. **103**, 170402 (2009).

[91] A. Sommer, M. Ku and M. W Zwierlein, New J. Phys. **13**, 055009 (2011).

[92] C. Kohstall, M. Zaccanti, M. Jag, A. Trenkwalder, P. Massignan, G. M. Bruun, F. Schreck, and R. Grimm, Nature **485**, 615 (2012).

[93] M. Cetina, M. Jag, R. S. Lous, I. Fritsche, J. T. M. Walraven, R. Grimm, J. Levinsen, M. M. Parish, R. Schmidt, M. Knap, E. Demler, Science **354**, 96 (2016).

[94] F. Scazza, G. Valtolina, P. Massignan, A. Recati, A. Amico, A. Burchianti, C. Fort, M. Inguscio, M. Zaccanti, and G. Roati, Phys. Rev. Lett. **118**, 083602 (2017).

[95] Z. Yan, P. B. Patel, B. Mukherjee, R. J. Fletcher, J. Struck, and M. W. Zwierlein, Phys. Rev. Lett. **122**, 093401 (2019).

[96] G. Ness, C. Shkedrov, Y. Florshaim, O. K. Diessel, J. von Milczewski, R. Schmidt, and Y. Sagi, Phys. Rev. X **10**, 041019 (2020).

[97] I. Fritsche, C. Baroni, E. Dobler, E. Kirilov, B. Huang, R. Grimm, G. M. Bruun, P. Massignan, Phys. Rev. A **103**, 053314 (2021).

[98] F. Chevy, Phys. Rev. A **74**, 063628 (2006).

[99] R. Combescot, A. Recati, C. Lobo, and F. Chevy, Phys. Rev. Lett. **98**, 180402 (2007).

[100] B. J. DeSalvo, K. Patel, G. Cai, and C. Chin, Nature **568**, 61 (2019).

[101] H. Edri, B. Raz, N. Matzliah, N. Davidson, and R. Ozeri, Phys. Rev. Lett. **124**, 163401 (2020).

[102] K. R. Patton and D. E. Sheehy, Phys. Rev. A **83**, 051607(R) (2011).

[103] A. L. Fetter, and J. D. Walecka, *Quantum Theory of Many-Particle Systems*, (Dover, New York, 2003).

[104] J. H. Van Vleck, Rev. Mod. Phys. **34**, 682 (1962).

[105] Y. Nishida, Phys. Rev. A **79**, 013629 (2009).

[106] S. De and I. B. Spielman, App. Phys. B **114**, 527 (2014).

[107] D. Suchet, Z. Wu, F. Chevy, and G. M. Bruun, Phys. Rev. A **95**, 043643 (2017).

[108] R. Liao, Phys. Rev. Res. **2**, 043218 (2020).

[109] H. Tajima, J. Takahashi, S. I. Mistakidis, E. Nakano, and K. Iida, Atoms **9**, 18 (2021).

[110] H. Moriya, H. Tajima, W. Horiuchi, K. Iida, and E. Nakano, Phys. Rev. C **104**, 065801 (2021).

[111] E. C. Pinilla, D. Baye, P. Descouvemont, W. Horiuchi, and Y. Suzuki, Nucl. Phys. **A 865**, 43 (2011).

[112] T. Arai, W. Horiuchi, and D. Baye, Nucl. Phys. **A 977**, 82 (2018).

[113] D. V. Fedorov and A. S. Jensen, Phys. Lett. **B 389**, 631 (1996).

[114] Y. Suzuki and M. Takahashi, Phys. Rev. C **65**, 064318 (2002).

[115] S. Ishikawa, Phys. Rev. C **87**, 055804 (2013).

[116] K. Ogata, M. Kan, and K. Kamimura, Prog. Theor. Phys. **122**, 1055 (2009).

[117] N. B. Nguyen, F. M. Nunes, I. J. Thompson, and E. F. Brown, Phys. Rev. Lett. **109**, 141101 (2012).

[118] T. Akahori, Y. Funaki, and K. Yabana, Phys. Rev. C **92**, 022801(R) (2015).

[119] H. Suno, Y. Suzuki, and P. Descouvemont, Phys. Rev. C **94**, 054607 (2016).

[120] E .W. Schmid and K. Wildermuth, Nucl. Phys. **26**, 463 (1961).

[121] C. Kurokawa and K. Katō, Phys. Rev. C **71**, 021301(R) (2005).

[122] C. Kurokawa and K. Katō, Nucl. Phys. **A 792**, 82 (2007).

[123] Y. Kanada-En'yo, Phys. Rev. C **91**, 014315 (2015).

[124] H. Tajima, H. Moriya, W. Horiuchi, K. Iida, and E. Nakano, Phys. Rev. C **106**, 045807 (2022).

[125] H. Hu, B. C. Mulkerin, J. Wang, and X.-J. Liu, Phys. Rev. A **98**, 013626 (2018).

[126] H. Tajima and S. Uchino, New J. Phys. **20**, 073048 (2018).

[127] W. E. Liu, J. Levinsen, and M. M. Parish, Phys. Rev. Lett. **122**, 205301 (2019).

[128] T. Wakasa, E. Ihara, K. Fujita, Y. Funaki, K. Hatanaka, H. Horiuchi, M. Itoh, J. Kamiya, G. Röpke, H. Sakaguchi, N. Sakamoto, Y. Sakemi, P. Schuck, Y. Shimizu, M. Takashina, S. Terashima, A. Tohsaki, M. Uchida, H.P. Yoshida, M. Yosoi, Phys. Lett. B **653**, 173 (2007).

[129] S. Adachi, Y. Fujikawa, T. Kawabata, H. Akimune, T. Doi, T. Furuno, T. Harada, K. Inaba, S. Ishida, M. Itoh, C. Iwamoto, N. Kobayashi, Y. Maeda, Y. Matsuda, M. Murata, S. Okamoto, A. Sakaue, R. Sekiya, A. Tamii, M. Tsumura, Phys. Lett. B **819**, 136411 (2021).

[130] Dr. Wataru Horiuchi (2009), PhD Dissertation, Niigata University.